

# Lawrence Berkeley National Laboratory

## Recent Work

**Title**

A Study of Hydrogen Embrittlement in Lath Martensitic Steels

**Permalink**

<https://escholarship.org/uc/item/4sg839xc>

**Author**

Kim, Young-Ho

**Publication Date**

1985-06-01



# Lawrence Berkeley Laboratory

UNIVERSITY OF CALIFORNIA

## Materials & Molecular Research Division

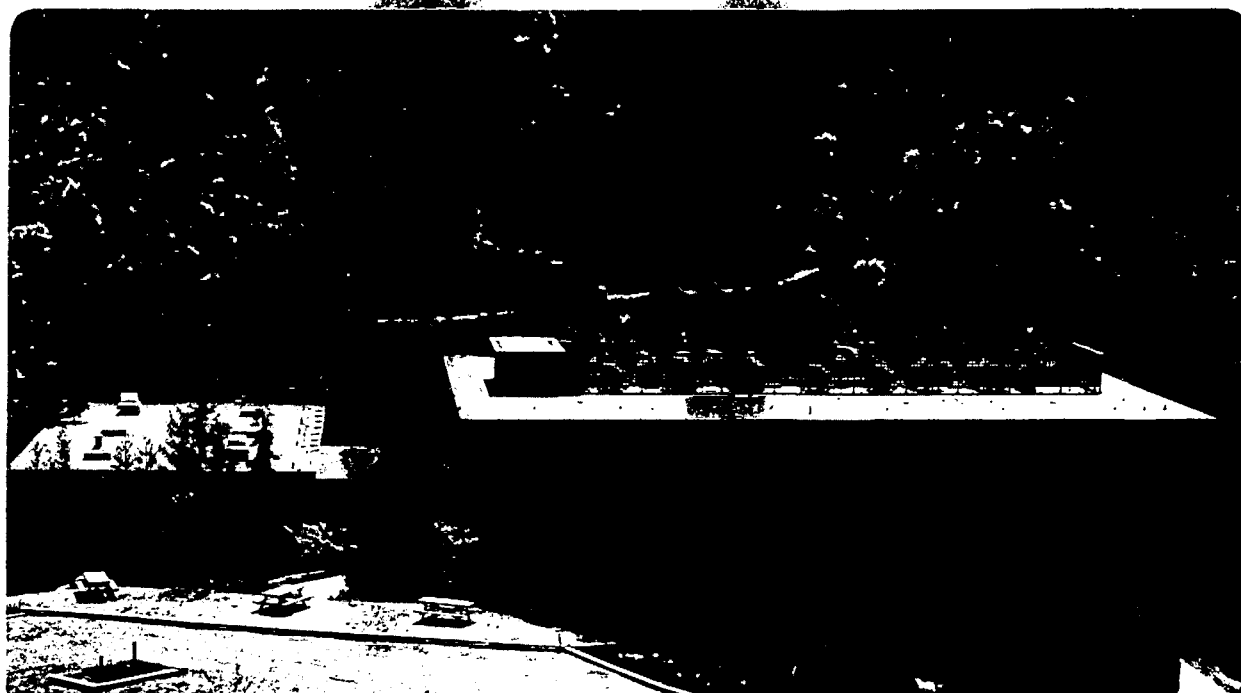
A STUDY OF HYDROGEN EMBRITTLEMENT IN LATH  
MARTENSITIC STEELS

Y.-H. Kim  
(Ph.D. Thesis)

June 1985

**TWO-WEEK LOAN COPY**

*This is a Library Circulating Copy  
which may be borrowed for two weeks.*



LBL-19962

## **DISCLAIMER**

This document was prepared as an account of work sponsored by the United States Government. While this document is believed to contain correct information, neither the United States Government nor any agency thereof, nor the Regents of the University of California, nor any of their employees, makes any warranty, express or implied, or assumes any legal responsibility for the accuracy, completeness, or usefulness of any information, apparatus, product, or process disclosed, or represents that its use would not infringe privately owned rights. Reference herein to any specific commercial product, process, or service by its trade name, trademark, manufacturer, or otherwise, does not necessarily constitute or imply its endorsement, recommendation, or favoring by the United States Government or any agency thereof, or the Regents of the University of California. The views and opinions of authors expressed herein do not necessarily state or reflect those of the United States Government or any agency thereof or the Regents of the University of California.

LBL-19962

**A Study of Hydrogen Embrittlement  
in Lath Martensitic Steels**

**Young-Ho Kim**

**Ph.D. Thesis**

**Lawrence Berkeley Laboratory  
University of California  
Berkeley, California 94720**

**June 1985**

## **ACKNOWLEDGEMENTS**

The author would like to express his deepest gratitude to professor J.W. Morris, Jr. for his guidance, encouragement, and support throughout the course of this research. He is also grateful to professors R.O. Ritchie and I. Finnie for their review of this manuscript. He would like to thank Drs. C.K. Syn, J.I. Kim, H.J. Lee, H.J. Kim, N.J. Kim, and B. Fultz for their advice and guide.

The author is greatly indebted to his family for their patience and encouragement. His wife, Hea Yun, provided me with the energy, enthusiasm, and love needed to complete this work. Special thanks extended to her for typing this manuscript.

The author is grateful to Mr. M. Strum and D. Frear for their help in reviewing this manuscript. The discussion with other colleagues helped me to develop many of the ideas in the present work; his recognition is extended to L. Summers, G. Fior, I.W. Wu, T. Mori, D. Dietderich, G.M. Chang, J. Glazer, S. Shaffer, D. Marinaro, P. Monardo, T. Huh, S.J. Kahng, H. Lee, and K. Lee.

The author appreciates the assistance provided by the support staff of the Materials and Molecular Research Division of Lawrence Berkeley Laboratory and by the Department of Materials Science and Mineral Engineering of U.C. Berkeley. Thanks are owed Mrs. J. Shall for the preparation of this manuscript.

He is also grateful to the Nippon Steel Corporation and D.W.

Taylor Naval Ship Research and Development Center for providing samples of 5.5 Ni steel and HY 130 steel.

This work was supported by the Office of Naval Research under Contract No. N00014-75-C-0154 and by the Director, Office of Energy Research, Office of Basic Energy Sciences, Materials Science Division of the U.S. Department of Energy under Contract No. DE-AC03-76SF00098.

**A STUDY OF HYDROGEN EMBRITTLEMENT  
IN LATH MARTENSITIC STEELS**

Young-Ho Kim

Ph.D.

Department of Materials  
Science and Mineral Engineering

**ABSTRACT**

Hydrogen assisted brittle fracture has been characterized in lath martensitic steels. Fracture modes in hydrogen assisted brittle fracture can be divided into three types: intergranular, brittle transgranular, and dimple rupture. Hydrogen assisted intergranular fracture and transgranular brittle fracture were the main interests of this study since these two brittle fracture modes control susceptibility to hydrogen embrittlement. The sources of metallurgical flaws which result in brittle fracture were identified and modifications to overcome these flaws are suggested.

First, the source of intergranular fracture was identified in 5.5 Ni steel. High resolution scanning Auger spectroscopy analysis showed that impurity segregation on grain boundaries was the main cause of intergranular cracking. Impurity segregation occurred during homogenization at very high temperatures or during aging in the temper embrittlement range. Intergranular cracking can be eliminated by removing the grain boundary impurities. As the concentration of the grain boundary impurities decreased, the fracture mode changed from intergranular to transgranular.

Next, the metallurgical flaw resulting in hydrogen-assisted transgranular brittle fracture was characterized in 5.5 Ni steel and HY 130 steel. The fracture surface generally followed martensite lath boundaries. Interlath microcracks were found frequently in the substructure just beneath the fracture surface. The fracture surface plane was identified as being dominantly the {110} plane which is also the common lath boundary plane. These observations suggested that hydrogen assisted transgranular fracture was governed by lath boundary decohesion.

The 5.5 Ni steel was three-step (QLT) heat treated to introduce precipitated austenite along the lath boundaries. The experimental results, however, showed that the precipitated austenite decreased the toughness and the ductility in the presence of hydrogen. The precipitated austenite transformed to martensite in the strain field ahead of the crack tip. Interlath cracks formed easily at the periphery of the

fresh martensite particles since the volume change that accompanied the martensite transformation imposed a tension across the lath boundary.

The 12 Ni steel was given a repeated rapid thermal cycle that induced a rapid reversion to austenite and retransformation to martensite. The specimen embrittled by hydrogen fractured in a totally ductile manner. This thermal cycling treatment was successful in improving the hydrogen resistance of lath martensitic steel because it refined the martensite lath size and decreased the mean free path of an interlath crack.



## 1. INTRODUCTION

### 1.1. Hydrogen Damage

Hydrogen has long been known to have a deleterious effect on the mechanical properties of many metallic systems. Hydrogen effects were documented first about one hundred years ago [1, 2], although steel makers and industrial workers suspected this long before [3,6]. According to Smialowski [3], Cailletet [1] found out in 1868 that during pickling of steel in dilute sulfuric acid, blisters were formed due to the accumulation of hydrogen in holes below the surface of the sample. In 1875, Johnson [2] reported most of the general phenomena of hydrogen embrittlement in steels in his paper, "On Some Remarkable Changes Produced in Iron and Steel by the Action of Hydrogen and Acids." Steel wires which had been immersed in an acid solution were embrittled and hydrogen bubbles were observed at the wire surface. Therefore hydrogen became recognized to be the cause of embrittlement.

Lath martensitic steels have high strengths and relatively high fracture toughness values. However, they are known to be susceptible to hydrogen embrittlement [4,5]; therefore, steelmaking, fabrication and the practical application of these steels has been somewhat limited by hydrogen embrittlement problems. It is well known that hydrogen promoted catastrophic embrittlement in sour gas wells, pressure vessels, turbines for generation of electrical power, piping and valves for transport of liquids and gases, as well as a wide spectrum of other applications [6]. Consequently, it is important to understand hydrogen embrittlement phenomena in high strength lath martensitic steels. At the same time, the understanding of the nature of hydrogen embrittlement should suggest a way to decrease the hydrogen susceptibility.

### 1.2. The Characteristics of Hydrogen Embrittlement

Hydrogen embrittlement concerns itself with phenomena such as the reduction of load-bearing capability and ductility [7]. There are typical characteristics of hydrogen embrittlement:

(1) A threshold stress (or stress intensity) exists, below which hydrogen assisted failure is not observed [8].

(2) The degree of embrittlement is dependent on temperature and strain rate [6].

(3) Sensitivity to embrittlement increases as the strength of a material is increased [8,9].

(4) Susceptibility to hydrogen embrittlement is sensitive to microstructure and alloy composition [10,11,148].

### 1.3. Theories of Hydrogen Embrittlement

The mechanisms proposed to explain hydrogen embrittlement are numerous and reflect the many ways in which hydrogen has been observed to interact with metals.

### 1.3.1. The Planar Pressure Theory

This mechanism was initially proposed by Zapffe [12] and has been modified by several subsequent investigators [13,14]. Zapffe and Sims [12] formulated the Planar Pressure theory which states that metals have an inherent mosaic substructure with small 'rifts' or regions of misfit between these subgrains. When hydrogen is dissolved in the steel, it enters as nascent hydrogen in interstitial solid solution. Due to the high diffusivity of hydrogen in steel, the hydrogen atoms diffuse to these rifts and recombine to form gaseous hydrogen. With calculations based upon the observed solubilities of hydrogen in steel, Zapffe's theory predicts that the pressure produced by the gaseous hydrogen in the rifts is added to the applied stress and thus lowers the apparent fracture stress.

The formation of scale or pimples on the surface of highly hydrogenated steels gives the best support for the planar pressure theory. Photomicrographs of the areas have been taken by Hobson and Sykes [15] and it can be seen that the metal apparently was blown apart by a high gas pressure, presumably in the rifts.

In spite of the fact that Zapffe's theory was generally accepted for several years after its publication, it has several shortcomings. It is difficult to see how this mechanism can explain the fact that there is a continuous reduction in ductility as the hydrogen concentration is raised. This theory predicts that at low concentrations, lower than critical pressures are generated in the rifts and embrittlement is therefore not present. Also it fails to explain that reinitiation of hydrogen-induced cracking by small changes in pressure unless hydrogen absorption also increases the ease of plastic deformation [16].

### 1.3.2. Surface Adsorption Model

Because of this apparent defect in Zapffe's theory, Petch and Stables [17] proposed a mechanism of hydrogen embrittlement based upon the theory of brittle fracture postulated by Griffith. According to the original theory of Griffith, the virgin material contains numerous small cracks. Fracturing will start for the critical magnitude of external stress at which an incremental enlargement of the crack results in a decrease in the total energy of the sample. This involves the release of elastic strain energy and potential energy of the applied loads in excess of the energy required to create the new crack surface, so that the net energy set free in the process is positive. If the crack continues to spread at a constant external stress with further decrease in the total energy of the sample, sudden fracture will occur with a very high rate of crack propagation.

Arguments against this model are that it underestimates the work of fracture [18]. It is inconsistent with the finding that oxygen, which has a greater heat of adsorption than hydrogen, suppresses cracking in the presence of hydrogen [16].

### 1.3.3. Decohesion Model

The decohesion Model comes from the idea that hydrogen dissolved in steels concentrates in regions of the positive hydrostatic component of elastic stress and that such concentrated hydrogen weakens the lattice by reducing the maximum cohesive force between the atoms so that a crack nucleates under the applied stress [19].

It was assumed that an interconnecting function exists between the interatomic force and hydrogen content and that as the hydrogen concentration is increased, the attractive force between metal atoms is decreased, including the maximum cohesive force. This model was first proposed by Troiano [20] and modified by Oriani [19,21]. Oriani [22] has also argued that Petch and Stables' proposal that hydrogen lowers the surface energy of iron is merely a special aspect of the cohesive strength argument. He has advanced the decohesion model by considering a thermodynamic argument [19]. The decohesion model successfully rationalizes the role of strain rate, temperature, and triaxial stresses on hydrogen embrittlement. But direct evidence to support this model has not been obtained so far and this model does not appear to be in satisfactory form. An exact definition of the hydrogen-lattice bond interaction must await a better understanding of the electronic interaction between hydrogen in solid solution and the bonding forces of the metal lattice.

### 1.3.4. Plasticity-Enhanced Embrittlement

Another proposal suggested by Beachem [23] is that hydrogen can assist deformation and assist fracture. Absorption of hydrogen increases the ease of dislocation motion or generation, or both. This concept is effective in rationalizing certain kinds of embrittlement data, and reduced flow stresses owing to the presence of hydrogen have, in fact, been observed.

This model differs in general from the previous models in that hydrogen is assumed to enhance plasticity locally rather than truly embrittle the lattice. It is, however, difficult to explain either the cleavage-like fracture or the observation of delayed failure by the hydrogen-induced ductility model. Indeed, contrary to this model, there is evidence such as strain aging [24] and internal friction [25] which show that hydrogen impedes dislocation motion.

### 1.3.5. Hydride Formation Theory

Hydrogen in concentrations above the solid-solution solubility limit will interact with many metallic systems to form a hydrogen-rich, and second phase known as a metal hydride. In general these hydrides are less dense than the host metal lattice and are brittle. The embrittlement of structural alloys involving the precipitation of a hydride was first proposed by Westlake [26] and Wood and Daniels [27].

Iron exhibits very high solid-solution solubilities with hydrogen and do not normally form metal hydrides. No iron hydride was found on

exposure to hydrogen pressure of up to 2.5 GPa [18]. So the hydride model has not been widely considered for iron and steel.

None of the widely varying theories described appears successful in explaining the wide variety of published experimental data. Most workers now agree that various theories may be operable as hydrogen affects the properties and behavior of the steels. Nevertheless, some of the theories are contradictory. Thus our overall understanding of the basic mechanism is as yet incomplete.

#### 1.4. Trap Theory of Hydrogen Embrittlement

The concept of trap was introduced to help to analyze hydrogen embrittlement phenomena [28-31]. Traps are defined as heterogeneities in the material with which hydrogen interacts quite strongly. Crack initiation and propagation correlate closely with hydrogen trapping phenomena. Hydrogen-trap interactions play a critical role in hydrogen assisted cracking [30].

A single hydrogen-trap interaction which occurs by a reaction of the type  $\underline{H} + T = HT$  is governed by an equilibrium constant expressed in terms of Fermi-Dirac Statistics [29] as

$$N_{HT}/(\alpha N_T - N_{HT}) = (N_{\underline{H}}/(\beta N_L - N_{\underline{H}})) \exp(E_B/kT)$$

where  $N_{HT}$ ,  $N_{\underline{H}}$ ,  $N_T$ , and  $N_L$  are the number densities of trapped hydrogen, hydrogen in solution, defect traps, and solvent lattice sites, respectively. The degeneracy factors  $\alpha$  and  $\beta$  are the number of trap sites per trap and the number of interstitial sites per solvent atom, respectively.  $E_B$  is the binding energy of the trap for hydrogen. Thus, a hydrogen trap is well characterized if its number density  $N_T$ , its binding energy  $E_B$ , and its saturability through the site degeneracy for hydrogen are known.

Traps characterized by their strength or binding energy can be divided into two types [30,31]. One is a reversible trap which can only weakly bind to hydrogen. The other is an irreversible trap. The strong traps behave irreversibly in the sense that the rate of escape of mobile hydrogen is much smaller than the captured rate.

Traps can play an important role since they can strongly affect the kinetics of hydrogen transport. Their presence can often reduce susceptibility by increasing the time necessary to reach some critical local hydrogen concentration [30]. Sometimes traps act as hydrogen sources or they accelerate the crack nucleation and propagation if the traps are mobile. These mobile traps can transport hydrogen at a much faster rate than by lattice diffusion, and provide an efficient location of rapidly-localizing of hydrogen concentration.

#### 1.5. General Approach

Although investigators cannot agree on the basic theory of hydrogen embrittlement, virtually all the studies support the hypothesis that one

necessary step in embrittlement is the development of a high, local and critical hydrogen concentration [32].

There may be two approaches for preventing or minimizing the hydrogen embrittlement problem in steel. The first is to attempt to prevent the absorption of hydrogen into the steel. This approach is sound and important, but limited in its potential for reliable structures since it will not always be possible to control the introduction of hydrogen. This is particularly true when steels are planned for use in a hydrogen-bearing environment. It is impossible to prevent hydrogen entry in the steel.

A second approach assumes that some amount of hydrogen will inevitably be present in steel and modification of the microstructure decreases the susceptibility to hydrogen embrittlement.

When lath martensitic steels are embrittled by hydrogen, they can fail by intergranular separation along the prior austenite grain boundaries (intergranular mode), by transgranular fracture which traverse the prior austenite grains (transgranular brittle mode), or by void nucleation and growth (dimple rupture mode). An example of the typical fracture modes is shown in Fig.1. All specimens were broken in a totally ductile manner in the absence of hydrogen, but hydrogen changed the fracture morphologies depending on the microstructures and alloy compositions. Brittle fracture modes predominate or contribute to hydrogen embrittlement susceptibility [4]. It appears that the presence of hydrogen encourages brittle modes of failure to operate at lower stress levels.

The metallurgical flaws in the microstructure that permit cracking to happen at relatively low stress must be identified to control brittle fracture. It is then possible to begin to understand how hydrogen interacts with those flaws. In the intergranular mode, it is apparent that the microstructural flaw is the prior austenite grain boundary. Intergranular cracking sometimes occurs depending on the the material's chemical composition and processing [33-35]. In the first part of this study, the intergranular mode was reviewed and characterized. In the transgranular mode, the source of fracture due to hydrogen has not been clearly identified. So the next part is focused on finding the metallurgical origin which results in hydrogen assisted transgranular cracking. A clear understanding of the microstructural sources of hydrogen embrittlement should lead to metallurgical modifications that will decrease embrittlement sensitivity.

## **2. EXPERIMENTAL PROCEDURE**

### **2.1. Materials Preparation and Heat Treatment**

The following steels were used for this study: 5.5 Ni steel, HY 130 steel, and 12 Ni steel. The compositions of these steels are given in Table 1.

### 2.1.1. 5.5 Ni Steel

A commercial 5.5 Ni steel was provided by Nippon Steel Corporation. The alloy was supplied as a 35.6 mm (1.4") thick plate and cut into several the blocks. The alloy was annealed at 1200°C for two hours to remove the effect of prior thermo-mechanical treatment. Specimens were cut from blocks and pre-machined to oversized dimensions. The alloy was austenitized at 800°C for one hour and quenched into ice water. Then specimens were given two tempering treatments. The first was a one-hour temper at 600°C to produce the condition designated QT. The second was the conventional QLT treatment: an intercritical anneal for one hour at 670°C followed by an intercritical temper for one hour at 600°C [36,37].

For the intergranular fracture studies, the specimens were given various heat treatments to produce the various conditions needed to creat different fracture modes (see Sec. 3.4).

### 2.1.2. HY 130 Steel

HY 130 steel was obtained from the David W. Taylor Naval Ship Research and Development Center in the form of a 25.4 mm (1") thick plate. The alloy was annealed at 1200°C for two hours, austenitized at 800°C for one hour, and tempered at 625°C for one hour.

### 2.1.3. 12 Ni Steel

The 12 Ni steel was melted in vacuum from pure starting materials, cast as a 9.5 kg ingot, homogenized at 1200°C for 24 hours under an argon atomsphere and upset cross-forged at 1100°C into a 15 mm (0.6") thick plate.

The plate was then annealed at 1200°C for three hours, furnace-cooled to 900°C and quenched in water. Its condition is designated 'AN'. The AN plate was machined and sliced to slightly over-sized Charpy impact specimens, which were used for the experimental work.

The other treatment is a rapid reversion treatment to the austenite reversion temperature in an induction furnace. The specimen was heated rapidly to 790°C and then immediately dropped into an oil bath. A single such cycle constitutes the 'C' treatment; a double cycle is designated 'CC'. The temperature was monitored during the rapid reversion cycle by spot-welding a thermocouple onto the specimen surface and embedding a second into the specimen center. The two had very similar readings and showed that the surface and bulk reached essentially the same peak temperature [38]. The sample treated in the induction furnace reached peak temperature (790°C) in approximately 15 seconds, while those heated in the air-muffle furnace took more than 15 minutes to reach the same temperature.

## 2.2. Hydrogen Charging Procedure

The cathodic charging technique was used for hydrogen embrittlement testing because of its safety and low cost compared with the high pressure gas exposure technique.

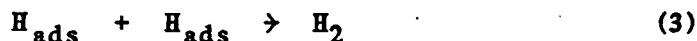
The entry of electrolytic hydrogen from an acid solution into a steel specimen acting as a cathode can be expressed as



which can be followed by either



or



Experimental studies have shown that only a small fraction of the hydrogen generated as shown in Equation (1) is subsequently absorbed as indicated by Equation (2), and that the majority of the hydrogen produced is evolved as hydrogen gas [39]. The reaction indicated by Equation (3) can be inhibited by the addition of recombination poisons such as As, P, and S to the electrolyte [39].

After machining to final dimensions, the specimens were covered with teflon tape except regions that were to be charged. The electrolyte was sulfuric acid solution and 0.5 mg of  $\text{As}_2\text{O}_3$  and 1 ml of  $\text{CS}_2$  was added to 1 liter of this solution as a cathodic recombination poison to promote hydrogen entry into the specimens [40]. The anode was platinum sheet or wire and the power source was an Eco model #550 potentiostat/galvanostat used as galvanostatic mode. External stress was not applied during charging.

The current density and the charging time were left as charging variables. Most specimens were charged for 24 hours to ensure the uniform hydrogen distribution in the specimen. With the exception of the Auger specimen, the specimens were not cadmium plated after hydrogen charging.

Hydrogen was expected to diffuse out from the Auger specimens on the high vacuum chamber before fracturing; therefore, it was necessary to prevent hydrogen effusion from specimen. Specimens were electroplated with cadmium because cadmium is considered an effective barrier to hydrogen permeation [41].

For the outgassing experiment, the specimen was put in the high vacuum chamber at room temperature for 20 days.

## 2.3. Mechanical Testing

### 2.3.1. Tensile Test

Uniaxial tensile tests were performed at room temperature and at 77 K using an 5 kN (1.1kips) capacity Instron Tensile testing machine (model TT-C) and a 220 kN (50kips) capacity Instron 1332 universal testing machine.

The tested specimens were round tensile specimens with 25.4mm (1 in) gage length and a 6.4mm (0.25 in) gage diameter, as shown in Fig. 2. Constant cross-head speed was  $6.35 \times 10^{-3}$  mm/sec for Instron 1332 machine and  $1.67 \times 10^{-3}$  mm/sec for Instron model TT-C. The tensile test were started within 5 minutes after the completion of hydrogen charging.

The yield strength was calculated by the 0.2% offset method and the total elongation was determined by measuring the difference in distance between gage length marking both before and after testing. The elongation and reduction in the area were measured by a travelling microscope with an accuracy of  $\pm 0.01$ mm.

### 2.3.2. Three Point Bending Test

Standard size Charpy specimens were modified to use in the three point bending test (Fig.3). Specimens were machined after heat treatment, fatigue precracked, and subjected to hydrogen charging. The notches were made perpendicular to the rolling direction of the plate. The crack tip area was protected with teflon tape, while the back side of the crack tip was exposed to the electrolyte for hydrogen absorption. The 1334 kN (300kips) MTS universal testing machine was used for this test.

### 2.4. X-ray Diffraction Analysis

X-ray diffraction analysis was performed to measure the volume fraction of austenite phase in the experimental alloys. Specimens were cut from bulk samples, ground on a set of SiC paper to create a clean smooth surface, and chemically polished in a solution of 3 ml HF(48%) + 100 ml H<sub>2</sub>O<sub>2</sub> (30%) for 10 minutes to remove any deformed surface where mechanically-induced transformation of the austenite phase may have existed. After this preparation, the specimens were scanned with either a Picker X-ray diffractometer (model 3488K) or a Siemens Kristalloflex X-ray diffractometer (model 500D) using Cu K<sub>α</sub> radiation. The volume fraction of austenite was calculated using Miller's method [42] in which the average integrated intensities of the (220) and the (311) austenite peaks are compared with that of the (211) martensite peak.

The formula used was:

$$\text{Vol. \% } \gamma = 1.4I_{\gamma} / (I_{\alpha} + 1.4 I_{\gamma})$$

where  $I_{\gamma}$  is the average integrated intensity of the (220) and the (311) austenite and  $I_{\alpha}$  is integrated intensity of the (211) martensite peak.

### 2.5. Microscopy

#### 2.5.1. Optical Microscopy

Specimens for optical microscopy were mounted in Koldmount or bakelite. The surfaces were ground by a step-by-step hand grinding using up to 600 grade SiC papers under flood cooling. Polishing was done on 1 μm diamond paste wheel and finally with 0.3 μm alumina on a



felt cloth. The specimens were etched with a 2% nital solution to reveal lath structure. The microstructures were examined with a Carl Zeiss metallograph.

### 2.5.2. Scanning Electron Microscopy

The fracture surfaces were examined in the scanning electron microscope (SEM) to characterize the fracture mode, crack propagation process and local deformation. The microscopes used in this study were an AMR 1000 SEM and ISI DS 130 SEM.

Chemical analysis was performed with a Kevex X-ray detector and analyzer attached to the microscope.

### 2.5.3. Stereo Scanning Electron Microscopy

Stereo fractographs were taken using the specimen tilting method to get the three dimensional image. The specimen was tilted symmetrically across the flat surface to minimize the distortion of the images. The optimum tilting angle was determined to be 10 degrees. Stereo pairs of SEM fractographs were observed under a WILD ST4 mirror stereoscope.

### 2.5.4. Transmission Electron Microscopy

Specimens for the study by Transmission Electron Microscope (TEM) were first cut into wafers of about 400  $\mu\text{m}$  thickness by an abrasive wheel saw with flood cooling. These wafers were chemically thinned to about 100  $\mu\text{m}$  in a solution of 3 ml HF (48%) + 100 ml  $\text{H}_2\text{O}_2$  (30%). The chemically thinned wafers were spark-cut into disks of 3 mm diameter, which were ground on a set of SiC papers to a thickness of 50  $\mu\text{m}$ . These disks were thinned to perforation in a twin-jet electropolishing apparatus using a cooled solution of 400 ml  $\text{CH}_3\text{COOH}$  + 75 gr  $\text{CrO}_3$  + 30 ml  $\text{H}_2\text{O}$ . Operation voltage was about 35 mV - 40 mV.

The foils were examined with Phillips 301 and 400 electron microscopes operated at 100 kV. High voltage microscope (Hitachi 650) was often used to observe the foils at 650 kV.

### 2.5.5. Profile Fractographic Technique

For the investigation of crack propagation, fracture surfaces were plated with nickel or pure iron. After the specimens were mounted with bakelite and they were cut perpendicular to the fracture surface and along the direction of crack propagation. The cross sections were polished, etched, and observed along the edge of the fracture surface in optical microscope or SEM. These cross sectional areas for SEM observations were coated with evaporated gold for electrical conduction.

The cross section of the fracture surface was also examined in the TEM. The plating layer for profile TEM was 0.8-1.5 mm. The specimens were sliced and mechanically polished to reduce thickness. Then thin foil specimens were prepared by a combination of electropolishing and ion beam milling [43,44]. A number of foils were obtained, which contained the profile of the fracture surface within the region that was

transparent to 100 kV electrons. The foils were then examined in a transmission electron microscope at an operating voltage of 100 kV and of 650 kV.

## 2.6. Auger Electron Spectroscopy (AES)

Specimens for Auger electron spectroscopic studies were cut from the heat treated plates and machined to the shapes and dimensions illustrated in Fig. 4. Specimens were cathodically charged at the current density of  $100 \text{ A/m}^2$  for 24 hours and then cadmium plated, according to the method described in section 2.7.

Auger electron spectroscopic studies were carried out with a PHI model 590 Scanning Auger Microscope (SAM) combined with a scanning electron microscope and an  $\text{Ar}^+$  ion sputtering gun.

Each specimen was put into the reaction chamber equipped with an in-situ fracturing stage. The specimens were slowly loaded at room temperature instead of impact-fracturing by hammer at liquid nitrogen temperature to reveal hydrogen induced fracture. After fracture, the specimen was positioned in front of the SAM cylindrical mirror analyzer and was then analyzed.

Following the AES analysis on the fresh fracture surface, the surface was sputtered by an  $\text{Ar}^+$  ion gun. The sputtered regions were re-analyzed to compare the difference between the surfaces before and after sputtering.

## 2.7. Etch Pit Technique

The orientation of fracture surface planes were examined by the etch pit technique in addition to profile transmission electron microscopy. Etching was done using the three-step procedure and the reagents suggested by several investigators [45,46]. The etchant and etching time are summarized in Table 2. Between each step, the specimen was flushed with running water. The specimen was observed in the SEM after it was rinsed in ethyl alcohol.

## 2.8. Electroplating

### 2.8.1. Cadmium Plating

The cadmium plating bath consisted of 22 gr/l of  $\text{CdO}$ , 144 gr/l of  $\text{NaCN}$ , 20 gr/l  $\text{NaOH}$ , and 4.5 gr/l of brightening agent dissolved in water and the anode was a cadmium block. Plating started within 10 minutes after completion of hydrogen charging and about  $25 \mu\text{m}$  thickness of cadmium layer was plated through all the specimen surface.

### 2.8.2. Nickel Plating

A commercial electrolyte was used for a bright nickel deposit. It consisted of 88 gr/l nickel chloride ( $\text{NiCl}_2 \cdot 6\text{H}_2\text{O}$ ), 315 gr/l of nickel sulfate ( $\text{NiSO}_4 \cdot 6\text{H}_2\text{O}$ ), and 45 gr/l of boric acid ( $\text{H}_3\text{BO}_3$ ). In order to avoid the formation of pores in the specimen-coating interface, the

current density must be kept low, about  $50 \text{ A/m}^2$ , at the beginning [44]. After a few hours, the current density could be successively increased to a maximum of  $200 \text{ A/m}^2$ .

### 2.8.3. Iron Plating

The bath used for iron plating was a solution of iron (II) and calcium chlorides, which has been referred to as the Fischer-Langbein solution [47]. The composition of the plating bath consisted of 300 gr/l of ferrous chloride ( $\text{FeCl}_2 \cdot 4\text{H}_2\text{O}$ ) and 335 gr/l of calcium chloride ( $\text{CaCl}_2$ ). This bath was operated at about  $90^\circ\text{C}$  using a high purity iron electrode and a current density of  $650 \text{ A/m}^2$ .

## PART I. INTERGRANULAR CRACKING

### 3. THE STUDY OF HYDROGEN ASSISTED INTERGRANULAR CRACKING

#### 3.1. Observation of Intergranular Cracking in 5.5 Ni Steel

The 5.5 Ni steel that had been homogenized at 1250°C fractured in an intergranular mode when broken after hydrogen charging (Fig. 5A). The same alloy fractured in a ductile mode when broken at room temperature before hydrogen charging. Intergranular cracking was not observed when the specimens were broken at liquid nitrogen temperature (Fig. 5B). As homogenizing temperature decreased, the portion of intergranular fracture decreased. The specimens homogenized below 1200°C and quenched to room temperature fractured in a mixed transgranular and dimple rupture mode even though hydrogen was charged.

#### 3.2. The Review of Intergranular Fracture

##### 3.2.1. Grain Boundary Chemistry

Impurity segregation on the grain boundary is regarded as the cause of intergranular fracture in iron and steel and has been studied extensively [33,48,49]. The most common elements which segregate to the grain boundaries and cause embrittlement are phosphorus [50-53], sulfur [54-57], tin [48,58], and antimony [48,59]. In addition to them, Te, Se, and Si can be grain boundary embrittling elements [49].

The effects of alloying elements on intergranular embrittlement are also recognized [35,49,50,60,61]. It is believed that impurity segregation to the grain boundary is influenced by the presence of common alloying elements [49,60]. It was found that Mo additions reduced phosphorus induced embrittlement, whereas Mn additions slightly enhanced it [53]. Ni is considered to promote the segregation of embrittling elements such as Sn, Sb and P to the grain boundaries [61]. Cr and Mn enhanced impurity induced grain boundary embrittlement in an Fe-impurity alloy system [60].

These segregation of embrittling elements may occur during austenitization [33] or aging in the temper embrittlement temperature range [48].

One important feature is that the extent of intergranular fracture is directly proportional to the degree of embrittlement and increases with increasing amounts of segregation to the grain boundaries.

It is believed that grain boundary embrittlement that causes intergranular fracture is associated with decrease of grain boundary strength due to segregation of impurities [49]. If impurity elements lower the cohesive strength of the grain boundaries, they cause the boundary to be the lowest energy path for crack propagation.

### 3.2.2. Combined Effects of Impurities and Hydrogen

A substantial amount of research in lath martensitic steels has shown that intergranular cracking can be accelerated in the presence of both segregated metalloid impurities and hydrogen on the grain boundaries. These embrittling impurities were found to be sulfur [54,62,63], phosphorus [51,58,61,64-66], nitrogen [51,58,61], silicon [58,61,65], tin [58,61,66], manganese [65]. Nickel also can be embrittled by hydrogen along the grain boundaries when Sb and Sn are segregated [67,68].

From the studies of temper and hydrogen embrittlement, the mechanisms of hydrogen-induced intergranular fracture assisted by impurities have been proposed [63,65,67,68]. Yoshino and McMahon [65] suggested the cooperative effect of segregated impurities and hydrogen on the loss of the cohesive strength of grain boundaries. Their interpretation of their results showed an interaction between hydrogen induced cracking and weakening of grain boundaries by impurities. Impurity elements like S, P, Mn, and Si are presumably responsible for the reduction of grain boundary cohesion. It was assumed that the presence of collected hydrogen can lower this cohesive strength still more, so that crack growth can occur along these grain boundaries at very low values of stress intensity. These observations are consistent with Oriani's analysis, which puts the main emphasis on the lowering of the maximum cohesive force by collected hydrogen [22]. Shin and Meshii's results suggest that the grain boundary weakening effects of metalloid impurities and hydrogen are independent and the combined effect is additive [69].

It has also been suggested that hydrogen and impurities have a synergistic effect on hydrogen-induced intergranular fracture [67,68]. Research on the intergranular embrittlement of nickel suggests that the entry of hydrogen into nickel occurs preferentially in the proximity of grain boundary intersections with the free surface, due to the presence of impurities that act as hydrogen recombination poisons [39] and stimulate the supply of atomic hydrogen to the crack tip.

It has been found that the amount of intergranular cracking increased and/or the mechanical properties decreased with the concentration of the grain boundary impurities. Bruemmer, et al. [62] correlated the percentage of intergranular fracture due to hydrogen to the sulfur concentration at the intergranular surface in pure irons which were deformed at room temperature with dynamic hydrogen charging. They found that a critical concentration of 13% monolayer coverage of sulfur determined the transition of the fracture mode from transgranular to intergranular fracture. The critical concentration is expected to be sensitive to the grain boundary segregation of other elements such as carbon [40,56]. Shin and Meshii [63,69] showed that the fracture stress of a hydrogen-free specimen linearly decreased with increasing sulfur concentration and that the fracture stress of hydrogen-charged specimens severely decreases with increasing sulfur concentration.

The above results suggest that a relationship exists between the role of the impurities and hydrogen in the reduction of grain boundary strength; however, the exact mechanism of this relationship is not yet known.

### 3.3. The Source of Intergranular Fracture in 5.5 Ni Steel

The surface-sensitive AES technique was applied to detect any segregation within a monolayer of the surface on the prior austenite grain boundaries in the homogenized specimens. An attempt to use a charpy size specimen to analyze the grain boundary surface after the specimen was broken in air was made, but it was not successful due to heavy oxidation. Therefore, an in-situ fracture stage was used to break hydrogen-charged specimens in the high vacuum Auger chamber. Since about 20 minutes is needed to pre-pump and transfer the specimen to the in-situ fracture stage, hydrogen may diffuse out, so the specimen was protected by a cadmium layer. Then a hydrogen-assisted intergranular fracture surface was revealed in the Auger chamber and typical Auger electron spectrum was obtained from the in-situ fracture surface.

As shown in Fig. 6, a sulfur peak was observed in the grain boundary. Carbon and oxygen were also detected on the whole fracture surface; however, their presence was attributed to adsorption from the environment. In order to reduce hydrogen outgassing from the Auger samples, the sample was loaded and fractured at the vacuum of about  $10^{-6}$  torr; therefore oxygen and carbon adsorption rates were sufficiently high to account for the observed coverages. It was also noticed that the vacuum suddenly dropped when specimen was loaded, which indicated that hydrogen diffused out easily from the stressed specimen.

Phosphorus and other impurities were not observed. After  $\text{Ar}^+$  ion sputtering on the prior austenite grain boundary, the sulfur peak disappeared from Auger spectrum (Fig. 6A and D).

### 3.4. Heat Treatment Effect

Some specimens of 5.5 Ni steel were heat treated for further study of intergranular cracking. After each heat treatment, the specimens were quenched into water. Standard charpy size saw-cut specimens were broken at liquid nitrogen temperature without hydrogen charging or at room temperature using a three point bending fixture (Fig. 7) after hydrogen charging at a current density of  $100 \text{ A/m}^2$  for 24 hours. The fracture surfaces were examined to measure the portion of intergranular fracture.

#### Case 1. Homogenized at $1250^\circ\text{C}$ for 2 Hours.

Uncharged specimens were broken in a totally ductile manner at room temperature and in a quasicleavage mode at liquid nitrogen temperature (Fig. 5B). The charged specimen fractured at room temperature showed a mixture of intergranular and transgranular mode (Fig. 5A). The intergranular portion was about 70%.

Case 2. Homogenized at  $1250^\circ\text{C}$  for 2 Hours and Temper Embrittled at  $450^\circ\text{C}$  for 200 hours.

Charged specimens fractured in a intergranular mode (Fig. 5C). The fracture surface was very smooth and there was no indication that some particles precipitated on the grain boundaries.

Case 3. Homogenized at 1250°C for 2 Hours and Austenitized at 800°C for 1 Hour.

The specimens broken after hydrogen charging showed intergranular cracking (Fig. 5D). The intergranular facet size of this specimen was same as that found in Case 1 or 2. A careful examination of the fracture surfaces showed small microvoids on the grain boundaries.

Case 4. Homogenized at 1250°C for 2 Hours Followed by Austenitized at 1000°C for 1 Hour.

Intergranular cracking was found in the charged specimen (Fig. 5E). Grain boundaries revealed by hydrogen were same size as those formed at 1250°C, but the intergranular facets were very small compared with Case 2. It is believed that these grain boundaries were formed during a heat treatment at 1000°C.

Case 5. Homogenized at 1100°C for 2 Hours.

Charged specimen fractured in a mixture of transgranular and dimple rupture mode (Fig. 5F). No intergranular cracking was observed.

Case 6. Homogenized at 1250°C for 2 Hours and Tempered at 590°C.

The specimens were tempered at 590°C for one hour, three hours, ten hours, and one hundred hours. The specimens showed primarily intergranular cracking after hydrogen charging (Fig. 8). Austenite precipitated along the prior austenite grain boundaries and lath boundaries since the tempering temperature (590°C) was within the two phase region of  $\alpha + \gamma$ . As tempering time increased, the austenite would grow and the austenite precipitates on the grain boundaries revealed by the hydrogen assisted fracture would become larger.

Case 7. Homogenized at 1250°C for 2 hours and Tempering at 670°C for 1 Hour and Tempering at 600°C for 1 Hour (designated ALT Treatment).

The ALT specimen was hydrogen charged and fractured using a three point bending fixture at room temperature. The fractography of this specimen is shown in Fig. 9. The specimen showed intergranular cracking (Fig. 9A), but the fracture surfaces of this specimen were not so smooth as those in the homogenized specimen (Fig. 9B).

### 3.5. Discussion

#### 3.5.1. Homogenization

Normally sulfur is precipitated as a sulfide in steels and not free to segregate to the grain boundaries. Sulfides like MnS, CrS, and FeS become thermodynamically less stable with increasing temperature [70]. If sulfur is free in a solution or dissolved from sulfide compound, it will segregate to the grain boundary.

Several investigators noticed that intergranular embrittlement was observed when the austenitizing temperature was high [71,72]. Briant

and Beneriji [71] found that no embrittlement was observed when the austenitizing temperature was at or below 1000°C; however, above that temperature, the sulfides dissolved and embrittlement was observed. If the sulfur was precipitated as MnS, a much higher austenitizing temperature was required to dissolve the sulfide [72]. Some of the sulfides dissolved during homogenization at high temperature would segregate along the austenite grain boundaries.

Similar problems occurred in the 5.5 Ni steel when it was homogenized at 1250°C. Detection of sulfur from the grain boundaries showed that a considerable amount of sulfides were dissolved. High resolution scanning electron microscopy did not reveal the frequent precipitate on the grain boundaries, and sputtering of the surface of the Auger specimens showed that the sulfur was located very near the surface within a monolayer. Therefore, sulfur did not exist in a precipitated form but in a metalloid form. The specimens homogenized at 1200°C or 1100°C showed less intergranular embrittlement since the dissolved sulfur was not much. Uncharged specimens did not reveal intergranular cracking even though they homogenized at the high temperature. The amount of segregated impurities would not be enough to induce intergranular cracking without the assistance of hydrogen; however, hydrogen presumably reduces the strength of boundaries more, so cracking followed the grain boundaries.

Once the sulfides were dissolved, it was very difficult to avoid intergranular cracking in the presence of hydrogen. All specimens homogenized at 1250°C showed some intergranular cracking on the fracture surfaces.

This sulfur-induced cracking phenomena resembles the rather old metallurgical problem of "overheating" or "burning" of alloy steels [72-74]. "Overheating" is caused by the solution of sulfide in austenite at high temperatures and its subsequent re-precipitate during cooling to form fine particles of sulfide on austenite grain boundaries, whereas "burning" is due to the formation of a film of sulfur-rich liquid at austenite grain boundaries [73]. Both phenomena require sulfur dissolution and segregation on the grain boundaries.

### 3.5.2. Temper Embrittlement

Aging in the temper embrittlement temperature range would build up the impurities on the grain boundary. The specimens show complete intergranular cracking when they were homogenized above 1200°C followed by aging at 450°C for 200 hours and broken after hydrogen charging. All the specimens temper embrittled at 450°C for 200 hours revealed at least a portion of grain boundaries, when broken at liquid nitrogen temperature. In these cases the amount of impurities that segregate along the grain boundaries during aging would be enough to decrease the grain boundary strength without hydrogen. In the present experiment, Auger analysis on the temper embrittled specimen was not attempted; however, the other work on the same steel demonstrated phosphorus segregation [75].



It was found that avoiding tempering in the temper embrittlement range reduced hydrogen induced intergranular cracking and increased the fracture toughness value [58].

### 3.6. The Elimination of Hydrogen Assisted Intergranular Cracking

The present and previous research on the hydrogen-assisted intergranular cracking has showed that impurity segregation is necessary for intergranular cracking. A possible way to eliminate intergranular cracking problem is to prevent impurities from segregating to the grain boundaries.

It has been found that titanium additions to low carbon steels [76], rare earth additions [77], and possibly aluminum additions [35] help to eliminate impurity induced embrittlement.

The present problem is sulfur-induced grain boundary cracking. High temperature homogenization causes the dissolution of sulfide so that free sulfur can segregate on the grain boundary. So sulfur should be removed from grain boundary.

A low temperature homogenizing treatment would be helpful since sulfide can not dissolve easily at low temperature. Unfortunately, a high temperature soaking is necessary to obtain a uniform microstructure.

If the impurities had already segregated on the grain boundaries, tempering was not effective in reducing the susceptibility to intergranular cracking. Austenite precipitated along the grain boundaries was revealed in Fig. 8. On the grain surface (grain boundary), both holes and austenite precipitates are observed. The holes on the grain boundary would be the location of the austenite precipitates on the other conjugate surface. Smith [78] suggested that proeutectoid ferrites formed on grain boundary would have a definite orientation relative to one of the austenite grains and a random relationship with the other. Even though the coherency and the orientation relationship of the interfaces were not obtained in the present experiment, austenite presumably precipitated as Smith suggested. Incoherent interfaces can absorb impurities but not coherent ones [52]; therefore, fracture would follow the incoherent interface.

The effect of austenite precipitates introduced by LT treatment after homogenization was also studied. It is well known that austenite can getter elements that promote intergranular cracking [79]. It may decrease susceptibility to hydrogen when the impurity concentrations at the grain boundary are reduced. As is shown in Fig. 9, the charged specimen also fractured in a intergranular mode; however, the fracture surfaces were very rough and portions of the grain boundaries were stuck together, which indicates that there was a resistance to separation and it would have higher fracture toughness. However, this heat treatment was not enough to eliminate hydrogen assisted grain boundary cracking.

One way to avoid hydrogen-assisted intergranular cracking is by the removal of deleterious species in the steel and making pure material.

HY 130 steel was purified by limiting the Mn and Si contents of the steel, by avoiding contamination of Sn [35]. This material eliminated the hydrogen-assisted intergranular cracking even though it aged 3000 hours in temper embrittlement temperature range. But as the impurity concentration in the grain boundary was increased, the hydrogen-assisted fracture path became more intergranular and the fracture toughness value decreased [35,58]. When the grain boundary impurity concentration was low, hydrogen-induced cracking occurred by transgranular.

### 3.7. Conclusion

The study has been conducted to characterize the hydrogen-assisted intergranular cracking by using 5.5 Ni steels. The following conclusions were obtained:

(1). The main source of hydrogen-assisted intergranular cracking is impurity segregation along the grain boundaries.

(2). Either high temperature homogenization or tempering at 450°C for a long time induced the grain boundary embrittlement. Low temperature homogenization and avoiding tempering in the temper embrittlement temperature range could reduce hydrogen-assisted intergranular cracking.

(3). Tempering at 590°C to introduce the austenite precipitates was not effective in reducing the susceptibility to hydrogen-assisted intergranular cracking.

(4). ALT treatment had some beneficial effect on hydrogen-assisted intergranular cracking, but it could not eliminate intergranular cracking.

(5). Making clean steel by avoiding contamination of impurities and controlling the alloying elements can eliminate hydrogen-assisted intergranular cracking as found in the HY 130 steel [35].

## PART II. TRANSGRANULAR CRACKING

### 4. THE SOURCE OF HYDROGEN-ASSISTED TRANSGRANULAR CRACKING

As discussed in the Part I, the fracture mode shifts from intergranular to transgranular mode when the concentration of grain boundary impurities decreases. The second part of the thesis is to study the hydrogen-assisted transgranular brittle fracture; the cracks propagate through the grains in a brittle manner. Materials used in this study were 5.5 Ni steel and HY 130 steel.

#### 4.1. Observation of Transgranular Cracking and Degradation of Mechanical Properties

Figure 10 shows typical load-deflection curves for three-point bending specimens of QT-treated 5.5 Ni steel fractured at room temperature with and without hydrogen charging. The hydrogen-free specimen had a high fracture toughness of approximately  $330 \text{ MPa}\cdot\text{m}^{1/2}$  ( $300 \text{ ksi}\cdot\text{in}^{1/2}$ ) and fractured in a totally ductile manner as illustrated by the scanning electron fractographs presented in Fig. 11. Hydrogen charging the specimen caused a drop in the load-deflection curve and a substantial decrease in the fracture toughness to approximately  $180 \text{ MPa}\cdot\text{m}^{1/2}$  ( $160 \text{ ksi}\cdot\text{in}^{1/2}$ ). The primary fracture mode was hydrogen assisted transgranular fracture (Fig. 12), with an occasional admixture of ductile rupture. Secondary cracks were infrequently observed branching away from the fracture surface. In the uniaxial tensile test, the effect of hydrogen manifests itself as a decrease of ductility. The uncharged 5.5Ni QT specimen has great ductility and was broken in a totally ductile mode (Fig. 13). The reduction of area was 79.2% and the total elongation was 29.8%. Hydrogen charging increased the strength slightly but caused large losses in ductility. The reduction of area of the charged specimen was 17.8% and the total tensile elongation was 5.6%. The fracture mode was a mixture of transgranular brittle fracture and ductile rupture (Fig. 14).

The brittle fracture mode characterizes the hydrogen susceptibility. Figure 15 shows the conjugated surfaces of hydrogen-assisted fracture. Both sides of the fracture surface match together with a one to one correspondence even though they look complicated. The projected region of one fracture surface matches the hollowed region in the other picture taken from the opposite fracture surface. These transgranular fracture surfaces suffered little deformation and separated easily during fracturing. The material showing transgranular brittle mode has low fracture toughness value and reduced ductility.

Accordingly, the next topic of this study was to characterize this fracture mode as well as to identify the source of transgranular fracture. The application of high resolution SEM and profile techniques of hydrogen-assisted transgranular fracture surfaces has led to a significant advance in their characterization. The use of SEM stereo pairs, in particular, yields a three-dimensional picture of the often complex surfaces. Furthermore, the SEM allows the matching of opposite fracture

surfaces. Profile techniques of the fracture surfaces allow an analysis of fracture path.

#### 4.2. Quasicleavage and Hydrogen Assisted Transgranular Fracture

The hydrogen-assisted transgranular fracture mode was first interpreted as cleavage [80] or quasicleavage (QC) [23]. Many investigators used QC to describe hydrogen-assisted transgranular cracking, because the transgranular mode in hydrogen embrittlement superficially resembles QC in low temperature thermal embrittlement [5,54].

The morphological difference between hydrogen-assisted transgranular brittle fracture and low-temperature cleavage was reported by several authors [81,82,83]. Kikuta [83] and others proposed that hydrogen assisted fracture be called 'quasicleavage fracture of hydrogen embrittlement (QCHE)' from the study of fracture facet size, fracture path, the orientation of the fracture surface. Hinotami [81] et al. also reported a morphological difference between low temperature embrittlement and hydrogen embrittlement. The fracture surface in hydrogen embrittlement consisted of small facets and showed rugged appearance, while low-temperature cleavage was smooth and flat. Nakasato and Bernstein [82] observed that hydrogen-assisted cracks were characterized by the planar segments and the markings perpendicular to the advancing crack front.

The most important feature of this difference comes from the orientation of fracture surfaces.

#### 4.3. Crystallographic Orientation of Transgranular Cracking

Early studies of hydrogen-assisted transgranular cracking found that the cracks were produced on {100} planes in Fe-3% Si single crystals [84-86]. These results were attained by observing the relative position of etch pit arrays of dislocations and crack traces on one specific surface of the specimen. The {100} planes are well known to be the usual cleavage planes of body center cubic iron [87,88] and the first concept of hydrogen-assisted cracking in BCC metals was cleavage fracture.

On the other hand, it was recently reported that hydrogen-induced transgranular cracks occurred along the potential slip planes. These fracture surface planes were {110} or {112} in a purified polycrystalline iron [40] and in iron single crystal [82], {110} in iron single crystal and several commercial alloy steels [81], and {112} subboundaries in a pure iron polycrystal [89]. Another report claimed that the hydrogen-induced fracture surface was changed from slip plane to cleavage plane by silicon addition [82].

Crystallographic studies of hydrogen-assisted transgranular cracking was also conducted on the lath martensitic steels. Hydrogen-assisted transgranular cracks occurred on {110} planes [83,90] which were identified by etch pit technique.

Gradually the fracture process of hydrogen-assisted transgranular cracking has been recognized to be different from that of low-temperature cleavage since the crystallographic orientations of the fracture surfaces are different. Therefore, it is not sufficient to interpret hydrogen embrittlement as a mere extension of quasicleavage fracture.

#### 4.4. Slip Plane Decohesion

Several authors have noted that the crystallographic orientation of the fracture surface is identical to the dominant slip plane in BCC metals. This coincidence between fracture plane and slip plane led them to suggest that embrittlement occurs through a glide/slip plane decohesion [91,92].

McMahon [92] proposed the mechanism of glide plane decohesion, which is analogous to the behavior of Zn at low temperatures [93]. The schematic diagram of this model is illustrated in Fig. 16. This model is based on two concepts: Moving dislocations carry hydrogen and hydrogen alters the binding energy of the crystal lattice in such a way that the cohesive energy is reduced. The carbides formed in the lath boundaries could provide effective dislocation barriers. The presence of hydrogen in the edge dislocation cores reduced surface energy and produces Zn-like glide plane decohesion.

The mechanism can be summarized as follows [34,92]:

(1) Plane strain plastic yielding occurs and hydrogen is carried along the slip lines in the cores of dislocations.

(2) The hydrogen is not only trapped and carried along by the dislocation cores, but also it enhances screw dislocation mobility and slip planarity [94].

(3) The accumulation of hydrogen in the slip lines becomes sufficient to allow glide plane decohesion when edge dislocations are blocked at the barriers such as interlath carbides.

But the evidence supporting this hypothesis in lath martensite steels is indirect since the crystallographic studies in hydrogen assisted cracking were done by etch pit technique [83,90] and optical fracture profile studies did not clearly reveal the crack path [34].

There is an alternative explanation for the observed crystallography of hydrogen-assisted transgranular fracture which is based on the orientation of lath boundary plane in high strength martensitic steels [152]. The hypothesis is presented in the following sections.

#### 4.5. The Structure of Martensitic Steels

Some steels (for example, iron-carbon) quenched from a high temperature have a very fine and sharp microstructure. The structure of quenched steel is called martensite in honour of A. Martens [95]. There are two major types of martensite in steels: plate martensite and lath martensite [96].

#### 4.5.1. Plate Martensite

Plate martensite is usually found in high carbon, high nickel and high nitrogen iron alloys. Plate martensite is composed of lenticular plates. The plates form individually and are heavily twinned. Extensive studies have been carried out elsewhere [95-99].

#### 4.5.2. Lath Martensite

A typical lath martensite structure is shown in Fig. 17. The structure is divided into grains of the prior austenite phase. A prior austenite grain is subdivided into several groups, each of which is named a 'packet' [96,98]. This optical microscopy shows that the basic units are generally aligned parallel to one another in a packet. The morphology of the individual unit has been characterized as needles [99,100], cells [100], laths [99] or fine platelets [101]. This unit is generally called a 'lath'. An individual lath resolved by etching is not well defined in the optical microscope.

Figures 18, 19, and 20 show transmission electron micrographs of the interior of a packet within this structure. The martensite is heavily dislocated. The laths within a packet are usually separated by highly dislocated low angle boundaries, sometimes by high angle boundaries. Twin boundaries are also occasionally found (Fig. 21). Lath boundaries lie nearly parallel to one another, but they are wavy and dovetail shapes are also observed.

#### 4.5.3. Lath Boundary Plane

The crystallography of lath martensite and the orientation of the lath boundary (or the habit plane) has been identified phenomenologically by several authors. In early studies on lath martensite, the habit plane was found to be  $\{111\}_\gamma$  [102-104]. Subsequent investigations using electron microscopy have shown that the habit plane is near to  $\{111\}_\gamma$  (equivalently  $\{110\}_\alpha$ ) in lath martensite structures. It was observed in low carbon Fe-C alloys [105,106], low nickel Fe-Ni alloys [98,100,107,108], low nitrogen Fe-N alloys [109], a pure iron martensite [110], low carbon Fe-Mn alloys [111], Fe-Cr alloys [112], and an Fe-Ni-Mn alloy [113]. Some deviations from the  $\{111\}_\gamma$  habit plane were reported, which were approximately  $\{557\}_\gamma$  (an 8 degrees deviation from  $\{111\}_\gamma$ ) in low carbon Fe-C alloys [114],  $\{213\}_\gamma$  (10-20 degrees away from  $\{111\}_\gamma$ ) in low carbon Fe-C alloys [115], and  $\{575\}_\gamma$  (equivalently  $\{154\}_\alpha$ ) in an Fe-Ni-Mn alloy [116]. The adjacent laths occasionally have a twin relation and the twin boundary was reported to be  $\{211\}_\alpha$  [117].

Most of the available evidence shows that the habit plane of lath martensite is in the vicinity of  $\{111\}_\gamma$  or  $\{110\}_\alpha$  even though uncertainty still exists as to the exact crystallography of the habit plane.

The prevalence of the  $\{110\}$  planes in the boundaries of martensite lath or subgrain suggests an alternative hypothesis for the observed crystallography of hydrogen-assisted fracture. This hypothesis is that transgranular fracture in hydrogen-embrittled lath martensitic steels

follows lath or subgrain boundaries, and hence resembles intergranular cracking more than the transgranular cleavage or glide plane decohesion. To clarify this issue, high resolution studies were performed to correlate the microstructure in lath martensitic steels to the hydrogen assisted fracture path.

#### **4.6. Fractographic Studies on the Fracture Surface**

##### **4.6.1. Scanning Electron Microscopy**

A close examination of the fracture surfaces revealed they were decorated by fine, wrinkle-like features (Fig. 22C). This wrinkle-like feature is much finer than the step or the ridge of the low temperature cleavage (Fig. 23) and is comparable in dimension to the martensite laths shown in TEM pictures (Fig. 18-21). Measurements of the fine unit showed that its size was on the order of a martensite lath in width [81,83].

Stereo observations of a tensile fracture surface reveal a feathery, needle-like structure (Fig. 24). It was also observed that some relatively flat areas are composed of several needle-like structures.

Another example of a stereo-fractograph of a three-point bending specimen shows similar morphology (Fig. 25). The direction of crack propagation is from the bottom to the top of the picture. Again, a needle-like structure and a relatively flat structure, which consisted of needle-like structure, were observed. Secondary cracks between relatively flat regions (one crack facet) were also observed. The structural units in a crack facet were stretched in a row, to the same direction. The crack facets changed their directions at some boundaries exhibited as shallow secondary crackings.

It was observed that dimple rupture fracture connected two adjacent transgranular brittle fractures (Fig. 26,27). This resembles the shear rupture which has the characteristic of small and shallow voids.

The above observations suggest that transgranular cracking occurs at least in part along with certain special planes and that it is likely hydrogen charging can reveal the substructure of martensite by causing interfacial separation.

##### **4.6.2. Profile Fractographic Studies**

The cross sections of the fracture surface of three point bending specimens were observed to characterize the fracture path. Typical examples of untempered 5.5Ni steel are shown in Figs. 28 and 29. The main fracture surface was protected by iron plating. In Fig. 28 the main crack is along the lath boundaries and short steps, indicated by arrow heads, which connect the crack (Fig. 28B) were observed. Secondary cracks (Center of Fig. 28A or the right side of Fig. 28B) parallel the lath boundaries and steps connecting secondary cracks were also observed.

The other fracture profile optical microscopy of 5.5Ni steel shows a main crack and a secondary crack along the lath boundaries (Fig. 29). This secondary crack was deflected at the packet boundary and both ends of the secondary cracks were curved at the packet boundaries.

A new approach was tried to observe the hydrogen-assisted cracks. First, specimens were loaded in a three-point bending fixture after hydrogen charging to initiate fracture, then unloaded before the crack had propagated through the whole section. A section of the crack-arrested region was observed (Fig. 30). Discrete cracks were found ahead of the arrested macrocrack. Figure 30A was taken before chemical etching to show the pattern of the discrete cracks. The crack propagation direction was from left to right. Most of the cracks were disconnected from each other. Figure 30B was taken after etching with a 2% nital solution to reveal the martensite substructure. This figure shows cracks along the lath boundaries, most of which terminate at packet boundaries. The only translath cracks observed were short crack segments connecting cracks along adjacent lath boundaries.

Figure 31 shows a second example of a discrete crack in this sample and illustrates the continuation of interlath cracks across packet boundaries. A crack would propagate into another packet if neighboring martensite laths were similarly oriented. This crack seems to be connected through the whole section but careful examination of it shows some discontinuity of cracks, and a high magnification picture confirmed this (upper region of a crack). Cracks were not straight and followed the etched boundaries.

Cracking along the lath boundaries was also observed in HY 130 steel (Fig. 32). Here the crack propagated parallel to the lath boundary except upper center region where the crack followed the phase boundary. This phase boundary may be either a packet or a prior austenite grain boundary, but it is not clear from this picture.

These observations suggest that the crack propagates preferentially along the martensite laths and lies either in or parallel to the lath boundaries. Optical and scanning electron micrographs of etched fracture profile specimens confirm this conclusion, but higher resolution techniques are required to determine where the crack lies either in or along the lath boundaries.

Transmission electron micrographs of the profile fractographic specimens of three-point bend tests afford a more detailed view of the fracture surface and the immediate subsurface region. Several examples are presented in Figs. 33-40. There is some uncertainty in the precise location of the fracture surface since the matching surface is unavailable and since it is possible that the specimen surface was slightly altered by the plating process. It is clear, however, that the fracture surface tends to parallel the long axis of the martensite laths. It also appears that the fracture surface lies in the lath boundaries over almost its whole length.

The fracture surfaces in profile transmission electron micrographs were not strictly straight because the lath boundaries were not



straight, and dovetailing within the packet was frequent. A zig-zag fracture surface indicates that the fracture process occurs along the dovetailed boundary. A few trans-lath steps that deviated from the lath boundary were observed (for example, the segment marked with an asterisk at the lower right in Fig. 34) and they seem to represent short steps connecting two main lath boundary crackings. High voltage transmission electron microscopy allowed a larger portion of fracture surface to be seen in Fig. 40, the fracture surface extended more than 10  $\mu\text{m}$  along the lath boundary.

Some regions beneath the fracture surface were a little deformed so the fracture surfaces were found close to the (110) plane by the trace analyses of diffraction patterns (Figs. 33, 34, and 39).

Cracking along the {211} plane is possible since the {211} plane is the boundary plane when adjacent laths are twin related [117] (see Fig. 21). The possibility of finding this plane is very small in a limited transmission electron microscopy study of a fracture surface.

Some subsurface regions yield diffraction patterns in which the spots are spread into arcs along the diffraction circle, as in Fig. 35 which is evidence of plastic deformation.

The high resolution transmission electron fractographs also revealed a dense population of fine secondary cracks immediately beneath the fracture surface. These secondary microcracks were observed in most of micrographs; they are located by solid arrows in Figs. 33-38 and by arrow heads in Fig. 39. The secondary microcracks almost invariably lay in and along lath boundaries. They usually initiated at irregularities in the lath boundary such as boundary intersections, steps, foreign particles, and at the tip of fresh martensite which was transformed from the austenite precipitate. They continued as sharp flaws in the boundary plane. In one isolated instance, shown in Fig. 36, a microcrack was located in the interior of a lath. This microcrack emanated from an impurity particle which is probably a carbide.

The microcracks were commonly found in the first few micrometers of material beneath the fracture surface but were not found in specimens taken from deeper within the fractured sample.

#### 4.7. Etch Pit Studies

Complementary work has been done to identify the orientation of fracture surface by the etch pit technique. Some chemicals can attack the surface very locally and the etch pits formed on the surface have a characteristic appearance which depends on the crystallographic orientation of the surface.

Figure 41 shows elongated hexagonal etch pits on the hydrogen-assisted transgranular fracture surface, which indicates the {110} plane. Etch pits were also obtained from the low temperature quasi-cleavage plane of the same specimen to compare with the hydrogen assisted transgranular fracture plane. Etch pits are square shapes since the

cleavage plane is {100} (Fig. 42). This observation is consistent with previous results [83,90].

#### 4.8. Outgassing Experiment

The outgassing experiment was done to determine whether the effect of hydrogen is reversible or irreversible. Specimens used in this experiment were the as received 5.5-Ni steel. Tensile tests were performed with three kinds of specimens; the uncharged specimen, the hydrogen-charged specimen, and the hydrogen-charged then outgassed specimen. The results are shown in Table 3. The outgassed specimen had almost the same tensile properties as uncharged specimen. Hydrogen-assisted transgranular fracture mode was not observed in the outgassed specimen. This result strongly suggests that the effect of hydrogen is reversible in this steel.

#### 4.9. Conclusion

The results presented above suggest that the hydrogen-assisted transgranular brittle fracture in lath martensitic steels is governed by interlath fracture. This conclusion is based on the following observations:

(1) The superficial transgranular fracture plane is predominantly the {110} plane which is the common lath boundary plane.

(2) All optical, scanning electron, and transmission electron micrographic views of the fracture surface reveal an apparent interlath fracture.

(3) Microcracks are common in the lath boundaries and certainly associated with the fracture process.

(4) Trans-lath fracture segments are only occasionally found and seem to be internal microcracks due to irregularities of lath structure, impurity particles, or short steps connecting interlath fractures.

Hence, hydrogen-induced transgranular fracture appears to be an interlath phenomenon which phenomenologically resembles intergranular fracture.

### 5. MICROMECHANISM OF HYDROGEN-ASSISTED TRANSGRANULAR CRACKING

The process of hydrogen assisted brittle fracture can be considered to be made up of two major steps. They are crack initiation and crack propagation.

#### 5.1. Crack Initiation

A microcrack will nucleate when hydrogen accumulates in vicinity of crack notch tip and a critical concentration is attained. It is generally agreed that the probable site for hydrogen accumulation is the location of the maximum triaxial stress state near the crack tip region

[22,118]. Hydrogen diffuses to this region under the driving force of a stress gradient.

An analysis of Rice [118,119] shows the location of maximum tri-axial stress ahead of a sharp crack

$$x = 2\delta = K_I^2 / (E\sigma)$$

where  $x$  = distance from the crack tip  
 $\delta$  = crack tip opening displacement  
 $K_I$  = stress intensity factor  
 $E$  = Young's modulus  
 $\sigma$  = the tensile yield strength

However, the crack initiation site is not restricted to the above location calculated by macroscopic data. Microscopic variation of the stress state and local hydrogen concentrations are also important. The heterogeneity near the location of the maximum triaxial stress state will be the most probable location for crack nucleation because the incompatibility of stress and hydrogen concentration exists across the heterogeneity.

These facts suggest that the internal interfaces serve as the preferred sites of hydrogen-assisted microcrack initiation. The transmission electron fractographic studies revealed that the crack initiated preferentially at the irregularities in the lath boundaries, inclusions (or particles), and interlath austenite precipitates.

The interlath microcracks near the fracture surface almost certainly formed ahead of the propagating crack tip, since the stress required to nucleate them would be relieved once the crack tip had passed. Costa and Thompson's experiment [54] in a QT-treated medium carbon steel also implies that the crack initiated below the Charpy-type notch root.

This microcrack initiation is almost certainly associated with the fracture process, which was proved by the outgassing experiment results (Sec. 4.8.). Microcracks would affect the tensile properties if they had already formed during hydrogen charging. Furthermore, microcracks were not found far away from the fracture surface of the three point bending specimen but were commonly found near the fracture surface of the specimens. Previous work showed that the substructure of the surfaces of dimple rupture fracture and low temperature quasicleavage did not reveal the lath boundary cracks [43,120]. Therefore, the possibility that the specimen would be damaged and microcracks would be induced during specimen preparation can be ruled out.

## 5.2. Crack Propagation

A careful examination of the fracture surface suggests that cracking occurs by the formation of small, lath boundary microcracks in advance of the main crack and their joining. The main crack continues to grow by repeated link-up of subsurface interlath cracks. This is in contrast to the incremental stable crack advancement. Profile studies of the fracture surface contain clear evidence for crack propagation along

lath boundaries. The continuity of the lath boundary network permits the growing microcracks to link together. It was suggested that subsurface cracks may present excellent sites for hydrogen recombination and pressurization [121]. The localized internal stress due to pressure of hydrogen developed in the microcrack may add the stress. Therefore this additional stress can lower the critical stress for crack propagation.

Another feature of crack growth is that it is discontinuous in nature. Acoustic emission studies show that a mechanical stop or jump can occur during crack propagation [122,123]. In fact, "clicks" were heard with the naked ear in the present experiment. A running crack will leave the excess hydrogen concentration behind so reaccumulation is necessary for another crack nucleation.

Sometimes, cracks grow across the laths. When the interlath microcracks lie parallel to each other in a packet structure, they may link by shearing the intervening bulk material. When the lath boundary planes are poorly oriented for easy crack propagation with respect to macroscopic stress state, cracking along the lath boundary is not energetically favorable. It may be possible that cracks transverse the lath boundary leaving lath boundary cracks by a terracing process. Therefore steps will be produced when the main and new lath boundary cracks join together. This could also occur by shear rupture of material between the cracks when the distance between the cracks is large enough for voids to nucleate.

### **5.3. The Characteristic of Lath Boundary Cracking**

#### **5.3.1. The Possibility of Impurity Segregation**

The scanning Auger microscope was used to identify any possible impurity segregation to the lath boundary. The Auger spectrum from the fracture surface did not show any possible impurity peaks. Since the specimen was fractured at a relatively low vacuum condition (see Sec. 3.3), contamination would disturb the detection of an impurity peak. But it is certain that the amount of segregated impurities on the lath boundary is much smaller than that on the grain boundary where a definite sulfur peak was observed in the annealed specimen at high temperature. It is unclear as to how the considerable amount of impurities can segregate on the lath boundary.

#### **5.3.2. The Structure of Lath Boundary**

There have been few reports on the structure or characteristic of lath boundaries. An analysis by Wakasa and Wayman [113] revealed that the lath substructure consisted of three sets of  $\langle 111 \rangle$  screw dislocation in a cross-grid arrangement and dislocations at lath-lath impingement boundaries are of the same nature as those found within laths. Recently Olson and Cohen developed a discrete-dislocation description of interphase-boundary structure [124,125] and applied these concepts to martensitic interfaces in order to calculate the stress fields, energy, and stability of martensitic interfaces [126]. But there is still a long way to an extensive understanding of the exact structure and characteristic of lath boundary.

However, it is well known that the lath boundaries are highly dislocated. This dislocation structure certainly affects hydrogen-assisted cracking.

#### **5.4. Interfacial Phenomena**

There is some evidence that hydrogen affects interfacial cohesion. The various kinds of interfaces could be the hydrogen assisted fracture path. Preferred crack paths were found to be grain boundaries [40], packet boundaries [54], twin boundaries [127], austenite/a' martensite and austenite/e martensite phase boundaries [128,129,130], subgrain boundaries [64], and particle-matrix interfaces [131].

This observation of interfacial decohesion is consistent with present work on interlath cracking. Since the lath boundaries are highly dislocated, hydrogen atmospheres will develop around lath boundaries. Autoradiographic studies [129,132] showing tritium trapping on lath boundaries (cell walls) supports this observation. Hydrogen atmospheres will certainly affect their interfacial cohesion.

It is also possible that dislocation glide influences the interlath fracture; the embrittled specimens undergo substantial plastic deformation during fracture and, in some cases, the material immediately adjacent to the transgranular fracture surface has been significantly deformed. The results, however, seem to establish that classic "glide plane decohesion" is a minor factor in the transgranular brittle mode if it is relevant at all. Moreover, since the transgranular brittle cracking is predominantly interfacial, it is not necessary to assume that hydrogen has any relevant effect on the bonding characteristics of the bulk alloy.

A similar process seems to operate in Fe-based alloys which contain no martensite phase. For example, Nagumo and coworkers [89] studied the hydrogen embrittlement of pure iron and found that embrittlement occurred only after the iron had been strained sufficiently to form well-defined subgrains. Fracture then proceeded through the nucleation and linkage of microfractures in the subgrain boundaries. Also, in this case the dominant mechanism of "transgranular" hydrogen embrittlement is apparently interfacial decohesion along internal boundaries.

## **6. EFFECT OF AUSTENITE PRECIPITATION**

### **6.1. Introduction**

A commercial 5.5 Ni steel was developed for structural use at cryogenic temperature, and it is toughened for cryogenic service by a three-step heat treatment (called the QLT treatment) [36,37] that causes the precipitation of a significant amount of a thermally stable austenite along martensite lath boundaries. The morphology, composition and mechanical behavior of this precipitated austenite have been studied in detail [36,37,88,120,133], and the precipitation of austenite has been verified to be beneficial in improving the low temperature mechanical properties [120,133].

Meanwhile, several investigators [9,134,136] have suggested that retained austenite is beneficial to the hydrogen resistance of lath martensitic steels. The mechanism of the improvement is, however, unclear and there are indications from other work that the austenite may be harmful [137].

To help to clarify this issue, it was decided to investigate the role of austenite in lath martensitic steels.

The plan was to use a heat treatment to introduce a controlled distribution of precipitated austenite along the martensite lath boundaries and to determine the influence of this austenite on the degree and mechanism of hydrogen embrittlement. Since the intercritical tempering treatments that introduce austenite in this steel also temper the dislocated lath martensite matrix, two heat treatments were used. The first, designated QT, provides a tempered martensite with very little precipitated austenite. The second, the QLT treatment, provides a tempered martensite matrix that is densely decorated with fine interlath islands of austenite.

## 6.2. Microstructure

When the alloy is tempered at a temperature just within the two-phase  $\alpha+\gamma$  field, as it is in the QT heat treatment, the dislocation network within the martensite is partly recovered and austenite is precipitated along the martensite lath boundaries [88,120,138]. The microstructure of the QT alloy is shown in Fig. 43. The volume fraction of precipitated austenite is only 1.8%, reflecting the relatively low tempering temperature and short tempering time. It was difficult to observe austenite in the lath boundary since the amount is very small. Sometimes the austenite precipitates were observed at the packet boundaries (Fig. 44).

The three-step QLT treatment produces a highly tempered martensite structure with a dense distribution of precipitated austenite [88,120,138]. The microstructure is shown in Fig. 45. The tempered martensite laths are outlined by well-defined boundaries even though the alloy has been tempered twice. The precipitated austenite content is about 8.5 volume percent. The dark-field micrograph in Fig. 45B brings out the elongated austenite particles along the martensite lath boundaries. The austenite precipitate can be distinguished from the so-called retained austenite by its shape. Retained austenite has a thin film shape (Fig. 46) which formed along the lath boundaries during the rapid quenching from the austenitizing temperature. Since the lath boundaries are very low-angle boundaries, it is possible for the interlath austenite to be simultaneously in almost exact crystallographic registry with both of the neighboring martensite laths. The Kurdjumov-Sachs (KS) relation [139] is usual (Fig. 45), although the Nishiyama-Wasserman (NW) relation [140,141] is also occasionally observed (Fig. 47).

## 6.3. Mechanical Tests

The results of the uniaxial tensile tests are presented in Table 4. In the uncharged condition the QLT specimen has a lower yield and ulti-

mate tensile strength than the QT specimen, but has greater ductility. Both alloys are significantly embrittled by hydrogen charging. The strength increases slightly while the ductility decreases substantially. The QLT specimen is the more severely embrittled of the two. After charging, the QLT specimen has a much lower tensile elongation than the QT specimen (2.2% vs. 5.6%) and an even more obviously depressed reduction in area (2.9% vs. 17.8%). This result is significant since the QLT specimen has a lower yield strength, and lower strength alloys usually show less sensitivity to hydrogen [8,9].

The results of the three-point bend tests were, qualitatively, the same. Before hydrogen charging both the QT and QLT alloys had high fracture toughness ( $330 \text{ MPa}\cdot\text{m}^{1/2}$  and  $360 \text{ MPa}\cdot\text{m}^{1/2}$ , respectively.) Both specimens were embrittled by hydrogen charging (Fig. 46). Again, the QLT specimen was the more severely affected of the two, based on its load-bearing capacity and crack-opening displacement. Its estimated fracture toughness ( $K_{\text{max}}$ ) was  $100 \text{ MPa}\cdot\text{m}^{1/2}$ , versus  $180 \text{ MPa}\cdot\text{m}^{1/2}$  for the QT specimen.

#### 6.4. Fractographic Analysis

Without hydrogen charging both specimens fractured in a fully ductile mode. After charging both fractured in a mixed mode that included transgranular brittle fracture and dimple rupture (Fig. 49). These observations confirm and complement the profile fractographic data on the QT alloy presented in Sec. 4.6.

Figure 50 is a profile transmission electron fractograph of a QLT specimen that was broken after hydrogen charging. The principal fracture follows lath boundaries. Secondary microcracks appear along the lath boundaries beneath the fracture surface. Some examples are marked by the arrows in the Fig. 50. The microcracks vary in length, with the smallest being about  $0.01 \mu\text{m}$ .

Previous work [43,142] on tempered Fe-Ni steels showed that precipitated austenite undergoes an essentially complete transformation to martensite in the deformed region near the crack tip. The hydrogen-charged QLT specimens behaved in the same way. While hydrogen charging did not induce transformation by itself, the precipitated austenite in the charged alloys transformed fully to martensite in the highly strained region near the crack. As shown in Fig. 50, the regions of the QLT specimens immediately below the fracture surface contain a number of dark interlath islands that are morphologically identical to the precipitated austenite islands shown in Figs. 45-47. Examples are at the ends of the arrows in Fig. 50A, and just to the left of the lowest arrow in Fig. 50B. However, high resolution diffraction studies show that these are dislocated martensite particles. There is an essentially complete transformation of the precipitated austenite near the fracture surface. Interlath microcracks emanate from fresh martensite particles. Typical examples are marked by the arrows in Fig. 51, 52, and 53.

### 6.5. The Influence of Precipitated Austenite

The results strongly suggest that the presence of precipitated austenite increases the severity of hydrogen embrittlement. The QLT-treated alloys which has a substantially greater austenite fraction (8.5%) than the QT-treated alloy (1.8%), is much less tough and ductile after hydrogen charging, even though its yield strength is significantly lower and its toughness and ductility in the uncharged condition are higher. Since both alloys have a well-tempered martensite matrix the principal difference between them is the austenite content.

The conclusion that precipitated austenite is the microstructural flaw in the QLT alloy is reinforced by the fractographic studies. These show that the precipitated austenite near the fracture surface invariably transforms to fresh martensite, and that the interlath cracks that form near the fracture surface almost always appear at the periphery of islands of fresh martensite. The strain-induced martensitic transformation provides preferential sites for interlath fracture. It has long been known that the presence of fresh martensite increases susceptibility to hydrogen embrittlement [143,148]. Snape [155] also showed that the presence of fresh martensite drastically reduced sulfide cracking resistance.

### 6.6. The Mechanism of Embrittlement by Interlath Austenite

It is intuitively plausible that the transformation of the precipitated austenite islands along the lath boundaries should promote interlath fracture [153]. A possible mechanism is diagrammed in Fig. 54. The martensite transformation of the precipitated austenite involves a volume increase of 2-3%. When the transforming particle is an elongated inclusion that lies in the lath boundary, as it is in the present case, the volume increase must impose a tensile stress perpendicular to the boundary that promotes fracture in the lath boundary plane by the wedge opening effect.

But the volume change on transformation does not cause interlath cracking by itself. The interlath austenite also transforms during the fracture of ferritic steels that are not hydrogen-charged, but does not cause any noticeable fracture on the lath boundaries [43]. In fact, the precipitated austenite is intentionally introduced into these steels to improve their resistance to brittle fracture [36,37,120]. However, hydrogen weakens the lath boundaries, as evidenced by the fact that the hydrogen-induced fracture is interlath whether or not austenite is present, to the point where they apparently cannot resist the combination of the applied stress and the stress imposed by the martensite transformation.

The transformation of the interlath austenite may actually contribute to the weakness of the lath boundary. Hydrogen is more soluble in the face-centered cubic austenite than in the body-centered cubic ferrite, and has been shown to accumulate in the austenitic constituent of a two-phase alloy [137]. If a saturated interlath austenite transforms it produces a supersaturated martensite. The most likely hydrogen diffusion path to relieve the supersaturation is along the lath



boundary, which should yield a transient increase in the local boundary concentration of hydrogen.

### **6.7. Comparison with Prior Work**

As described in the Sec. 5.1., previous work on the influence of retained austenite on hydrogen embrittlement produced mixed results. Some authors [8,134-136] report an improvement in hydrogen resistance when retained austenite is present while others report a deterioration [137]. Since the fractographic details of the embrittlement are not identified in the papers, it is not possible to make a specific comparison between that work and this. It does seem likely that the embrittlement phenomena reported by Toy and Phillips [137] are similar to those documented here.

It is, moreover, possible to suggest at least two circumstances in which retained austenite might enhance hydrogen resistance. The first was proposed by Ritchie et al. [134] and by Gooch [135] to explain an increased resistance to hydrogen under dynamic conditions. They noted the higher solubility and lower diffusivity of hydrogen in the austenite phase, and suggested that the austenite might act as a sink for hydrogen to retard its migration to the crack front. This model presumes, of course, that the alloy is unsaturated and the austenite is mechanically stable.

The second case in which one would expect the austenite to improve hydrogen resistance is when the alloy is brittle in an intergranular mode. As it was discussed in Sec. 3.6., it may reduce susceptibility to hydrogen relative to that the alloy would have if its boundaries remained contaminated. The fractographic evidence for this mechanism would be relative improvement in the toughness in the hydrogen-charged condition accompanied by a change in the fracture mode from intergranular to transgranular or by a change from the smooth intergranular surface to rough one. The toughness in the presence of hydrogen would, however, remain less than it would be if both the austenite and the grain boundary contaminant were absent.

### **6.8. The Contrasting Influence of Precipitated Austenite on the Ductile-Brittle Transition**

The QLT treatment was developed for 5.5Ni steel to decrease its ductile-brittle transition temperature for low-temperature service [36,37]. Roughly similar heat treatments are used to control the ductile-brittle transition in other ferritic steels [43,144,145]. The mechanism of brittle fracture in these alloys is transgranular cleavage. The addition of precipitated austenite has the paradoxical effect that it suppresses transgranular thermal embrittlement while it promotes transgranular hydrogen embrittlement.

The source of the paradox lies in the different fractographic mechanisms of transgranular thermal and hydrogen embrittlement. The dominant low-temperature cleavage plane is the {100} cleavage plane [87,88,146]. This plane crosses the low-angle martensite lath boundaries with the consequence that martensite packets cleave as a unit.

Interlath austenite cuts through the cleavage planes. The precipitation of austenite along the martensite lath boundaries serves to interrupt the cleavage planes, as illustrated in Fig. 55 and hence refines the effective grain size of the alloy. This grain refinement is indirect. In virtually all cases studied to date the precipitated austenite is mechanically unstable and is transformed to martensite by the plastic deformation associated with the advancing crack. The crystallographic variant of the martensite product is influenced by the mechanical state at the time of transformation [120,144], as illustrated in Fig. 56 which was taken from substructure near the dimple fracture surface. The martensite variant adopted by the mechanically retransformed austenite is usually different from the dominant variant of the surrounding packet. The crystallographic alignment of the martensite packet is hence broken up, and the possibility of clean trans-packet cleavage along the crystallographic planes is removed. Since the ductile-brittle transition is associated with the replacement of ductile rupture by the cleavage fracture mode, microstructural changes which increase the difficulty of cleavage fracture are effective in lowering the ductile-brittle transition temperature. However, hydrogen embrittlement shifts the dominant fracture plane to the lath boundary, which tends to lie near {110}. The interlath austenite lies in these planes. Its transformation promotes interlath fracture by the mechanism outlined above.

## 7. MODIFICATION OF MICROSTRUCTURE

### 7.1. Approach

Since the mechanism of transgranular hydrogen embrittlement is interlath separation, there are several ways in which it might be suppressed:

- (1) By preventing the accumulation of hydrogen in the lath boundaries to the critical concentration.
- (2) By improving the inherent resistance of the lath boundary to hydrogen embrittlement.
- (3) By decreasing the mean free path of a lath boundary crack.

It is not clear how the internal structure of the boundary could be changed to prevent the segregation of hydrogen or to improve its inherent resistance. It is not always successful and sometimes dangerous to add traps in the steel to prevent the accumulation of hydrogen in the lath boundary since they could be potential crack nuclei [11,30]. An example of this is the introduction of austenite precipitates.

The microstructural feature that can be controlled is the dimension of the lath that determines the mean free crack length or the potential crack length during crack propagation. Reducing the facet size can increase the amount of plastic deformation during crack propagation. For example, in the coarse microstructure (Fig. 31), the cracks run along the lath boundaries easily for several hundred micrometers and, in the finer microstructure (Fig. 30), the cracks were short and

disconnected and will not propagate easily. So refining the lath structure and making it more complicated will improve the resistance of hydrogen-assisted cracking. Since several results imply the beneficial effect of grain refinement [147,148], this approach looks like a good solution to hydrogen problem in steels.

Previous work [38] has shown that the lath size is dramatically reduced and the alignment of laths are very complicated if the alloy is given a repeated rapid thermal cycle. This method was applied to attack hydrogen embrittlement problem and the hydrogen sensitivity was tested with rapid thermal cycled specimens.

## 7.2. Microstructure

Annealing at 1200° followed by water quenching produced a coarse microstructure. The microstructure of the 12Ni steel alloy in the annealed-and-quenched (AN) state is illustrated by the optical micrograph in Fig. 57A. The alloy is divided into prior austenite grains, each of which is subdivided into packets of lath martensite. The boundaries of the packets are irregular, as evidenced by their jagged appearance in the plane of the micrograph and by the appearance of islands of one packet in the interior of its neighbor.

The substructure of the alloy is illustrated by the transmission electron micrograph in Fig. 58, which is typical of those taken to characterize the substructure of the steel. This micrograph contains over 70 parallel laths that are long and nearly straight in the plane of the figure. Selected area diffraction patterns were taken over the whole area shown. An example is included in the inset to the figure. The diffraction patterns show that all laths have the same crystallographic orientation, demonstrating that only a single martensite variant is present. It follows that the laths are separated by low-angle boundaries.

The microstructures of the alloy in single and double rapidly thermal cycled ('C' and 'CC' respectively) are shown in Fig. 57B and C. It is clear that the microstructural change induced by the rapid thermal cycle is quite different from that associated with conventional austenitization. There is no evidence of recrystallization in the 'C' and 'CC' microstructures, but the packet substructure has been disturbed, particularly after the second rapid cycle. In the 'C' condition the prior austenite grain boundaries are roughened and partly obscured by the martensite transformation product. In the 'CC' condition the prior austenite grain boundaries can hardly be found. The substructure of the alloy in the 'CC' condition is illustrated by the transmission electron micrograph shown in Fig. 59. In contrast to the 'AN' (Fig. 58) condition, the lath morphology within the 'CC' alloy is irregular and the lath boundaries are difficult to trace. The crystallographic alignment between adjacent laths has been largely destroyed. The distinct variants can be separated with dark field techniques, as shown in Fig. 59. The region shown in Fig. 59 contains at least three martensite variants, which yield three distinct diffraction patterns that are indexed as [113], [001], and [115]. The dark field micrographs were taken from the diffraction spots that are marked with arrows in these three

diffraction patterns. The results show that different martensite variants are intermixed on a very fine scale.

The results of the transmission electron microscopy suggest that the 'CC' alloy has an extremely fine effective grain size, on the order of 1  $\mu\text{m}$ .

### 7.3. Fractography

The specimens were broken by bolt-loading immediately after hydrogen charging. Figure 60 shows the scanning electron microscopy of the fracture surfaces. The 'AN' alloy shows a mixture of transgranular cracking and dimple rupture and the 'C' alloy shows the dimple rupture mode with small regions of transgranular cracking, while 'CC' alloy shows totally ductile mode.

The 'AN' and 'CC' specimens were temper embrittled at 450° for 300 hours and broken after hydrogen charging. The 'AN' specimen fractured in an intergranular mode (Fig. 58A) but 'CC' alloy fractured in a totally dimple rupture mode (Fig. 58D). It has been reported that there is a tendency to change the fracture mode from brittle transgranular cracking to dimple rupture as the stress intensity increased in hydrogen environments [122,135,149]. This correlation between fracture mode and stress intensity suggests that thermal cycling yields a substantial resistance temper or hydrogen embrittlement.

### 7.4. Grain Refinement by Rapid Thermal Cycling

The rapid reversion treatment that is used in the 'C' and 'CC' treatments creates an extremely fine effective grain size by destroying the alignment of adjacent martensite laths. Hence the term 'packet refinement' is used to distinguish this mechanism from the 'grain refinement' associated with the recrystallization of the austenite. Packet refinement is clearly the most efficient means for decreasing the effective grain size. This fine grain size governs both cleavage and hydrogen embrittlement. The resulting alloy has a ductile-brittle transition temperature well below 77 K [38] and fractures in a ductile mode after tempering and hydrogen charging.

While the mechanism of packet refinement in a rapid austenitization cycle needs further investigation, the results are plausible in the light of current understanding of austenite reversion. Rapid reversion prevents recrystallization due to the absence of holding time, so that the austenite that retransforms into martensite on quenching has a high density. The martensite is crystallographically related to its parent by the Kurdjumov-Sachs relations:  $(111)_{\gamma} // (011)_{\alpha}$ ,  $[110]_{\gamma} // [111]_{\alpha}$ . These relations permit 24 variants of martensite to appear in a single prior austenite grain, but for reasons that are not well understood, the martensite forms cooperatively in packets of a single variant. Given the high defect density in reverted austenite, and the propensity for the heterogeneous nucleation of martensite, it is certainly possible that the cooperative growth of adjacent laths is suppressed so that martensite laths appear in small elements whose

variants are more randomly chosen from among those permitted by the K-S relations.

### 7.5. Concluding Remarks

This rapid thermal treatment reduced the facet size so made crack path more tortuous and increased the amount of plastic deformation. Rapidly thermal treated specimen fractured totally dimple rupture mode, even though it was embrittled by hydrogen.

The possibility of achieving ultrafine grain size through a rapid austenitization treatment has been used, empirically, in the development of the multipass welding techniques that permit the welding of ferritic cryogenic structural steels with ferritic filler metals [150,151], and hence has commercial significance. In addition to it, this kind of thermal cycle may help to explain the improved hydrogen resistance of HY 130 welds that are made with a multipass gas-tungsten-arc (GTA) welding process [154].

## 8. CONCLUSION

### Part I. Intergranular cracking

Hydrogen-assisted intergranular cracking is observed in 5.5Ni steel when the specimens are homogenized at very high temperatures. Auger electron spectroscopy analysis of these specimens shows that sulfur segregates along the grain boundaries in the form of a metalloid. The segregated impurity alone is not sufficient to cause grain boundary fracture since intergranular cracking is only observed in the hydrogen-charged specimens. One-step tempering at 590°C is not effective in reducing the susceptibility to hydrogen-assisted intergranular cracking when the grain boundaries are contaminated by impurities. Two-step tempering treatments which introduce a dense distribution of precipitated austenite are beneficial but do not eliminate intergranular cracking. The elimination of intergranular cracking in hydrogen charged specimens requires the removal of the impurities segregated along grain boundaries.

### Part II. Transgranular Cracking

The hydrogen assisted transgranular cracking in 5.5Ni steel and HY 130 steel was characterized. All optical, scanning electron, and transmission electron microscopy reveal the presence of lath-like structures on the fracture surfaces. Profile fractographic studies show that the fracture surface generally follows martensite lath boundaries. In addition, interlath microcracks are frequently found in the substructure just beneath the fracture surface. These observations suggest that hydrogen-assisted transgranular cracking is primarily an interlath cracking phenomenon. Since the lath boundary planes tend to lie in {110}, the results explain the prevalence of {110} fracture surface planes.

The results also suggest a micromechanism for hydrogen-assisted transgranular cracking in lath martensitic steels. Hydrogen diffuses to the lath boundaries near the location of the maximum triaxial stress state ahead of crack tip and weakens the lath boundaries. Fine cracks form on the lath boundaries when the concentration of hydrogen reaches a critical value. The main crack continues to propagate along the lath boundaries by repeated joining of interlath microcracks until it produces the macroscopic failure.

The effect of precipitated austenite on hydrogen embrittlement in 5.5Ni steel was also investigated. The hydrogen resistance decreases when it is heat treated to introduce a dense distribution of precipitated austenite along the lath boundaries in the dislocated lath martensitic substructure. The hydrogen-induced fracture is transgranular and follows the lath boundaries as it did in the QT specimens. The precipitated austenite undergoes a strain-induced transformation to martensite ahead of the crack tip. The strain associated with the transformation, particularly the volume increase, apparently imposes a tensile stress across the lath boundary that promotes fracture. Small microcracks are often found that emanate from the periphery of the transformed austenite particles along the lath boundaries. The transformed austenite may also act as a source of hydrogen that contributes to the embrittlement of the lath boundaries. It follows that austenite precipitation is not useful for improving resistance to transgranular hydrogen embrittlement.

Rapid thermal cycling treatments were applied to 12Ni steel in an effort to attack the hydrogen embrittlement problem. Repeated rapid thermal cycling treatments refine the lath size and decrease the mean free path of an interlath crack. The specimens given the rapid thermal cycling treatments and embrittled by hydrogen failed in a totally ductile manner. Since this ductile dimple rupture mode yields a high fracture toughness, the resistance to hydrogen embrittlement is raised by thermal cycling treatments.

## REFERENCES

1. L. Cailletet: Compt. Rend., 1868, vol.66, p. 847.
2. W.H. Johnson: Proc. Roy. Soc., London, 1875, vol. 23, p. 168.
3. M. Smialowski: Hydrogen in Steel, Addison Wesley, Reading, MA and Pergamon Press, NY, 1962.
4. C.A. Zanis: SAMPE Quarterly, 1978, p. 8.
5. H.G. Nelson: Treatise on Materials Science and Technology, 1983, vol. 25, p. 275.
6. A.W. Thompson and I.M. Bernstein: Metallurgical treatises, J.K. Tien and J.Elliott, eds., TMS-AIME, Warrendale, PA, 1981, pp. 589-601.
7. R.A. Oriani: Ann. Rev. Mater. Sci., 1978, vol. 8, p. 327.
8. W.W. Gerberich and Y.T. Chen: Metall. Trans. A, 1975, vol. 6A, p.271.
9. J.F. Lesser and W.W. Gerberich: Metall. Trans. A, 1976, vol. 7A, p. 953
10. I.M. Bernstein and A.W. Thompson: Hydrogen Embrittlement and Stress Corrosion Cracking, R. Gibala and R.F. Hehemann, eds., ASM, Metals Park, Ohio, pp. 135-152.
11. G.M. Pressouyre: Current Solutions to Hydrogen Problems in Steels, C.G. Interrante and G.M. Pressouyre, eds., ASM, Metals Park, Ohio, 1982, pp.18-34.
12. C.A. Zapffe and C.E. Sims: Trnas. TMS-AIME, 1941, vol. 145, p. 225.
13. F. de Kazinczy: JISI, 1954, vol. 177, p. 85.
14. A.S. Tetelman: Fracture of Solids, D.C. Drucker and J.J. Gilman eds., Wiley (Interscience), NY, 1963, pp. 671-708.
15. J.D. Hobson and C. Sykes: JISI, 1951, vol. 169, p. 209.
16. M.R. Louthan, Jr. and R.P. McNitt: Effect of Hydrogen on Behavior of Materials, A.W. Thompson and I.M. Bernstein, eds., AIME, New York, NY, 1976, p.p. 496-506
17. Petch and Stables: Nature, 1952, vol. 169, p. 842.
18. J.P. Hirth: Hydrogen Embrittlement and Stress Corrosion Cracking, R. Gibala and R.F. Hehemann, eds., ASM, Metals Park, Ohio, 1984, pp. 29-41.
19. R.A. Oriani: ivid., pp. 43-59.

20. A.R. Troiano: *Trans. ASM*, 1960, vol. 52, p. 54.
21. R.A. Oriani: *Ber. Bunsen-Ges. Phys. Chem.*, 1972, vol.76, p. 848.
22. R.A. Oriani: *Stress Corrosion Cracking and Hydrogen Embrittlement of Iron Base Alloys*, NACE, Houston, TX, 1977, pp. 351-358.
23. C.D. Beachem: *Metall. Trans.*, 1972, vol. 3, p. 437.
24. A.M. Adair and R.F. Hook: *Acta Metall.*, 1962, vol. 10, p. 741.
25. R. Gibala: *Trans. TMS-AIME*, 1967, vol. 239, p. 1574.
26. D.G. Westlake: *Trans. ASM*, 1969, vol. 62, p. 1000.
27. T.W. Wood and R.D. Daniels: *Trans. TMS-AIME*, 1965, vol. 233, p. 898.
28. G.M. Pressouyre: *Metall. Trans. A*, 1979, vol. 10A, p. 1571.
29. R. Gibala and A.J. Kumnick: *Hydrogen Embrittlement and Stress Corrosion Cracking*, R. Gibala and R.F. Hehemann eds., ASM, Metals Park, Ohio, 1984, pp. 61-77.
30. G.M. Pressouyre and I.M. Bernstein: *Metall. Trans. A*, 1981, vol. 12A, p. 835.
31. A.J. Kumnick and H.H. Johnson: *Acta Metall.*, 1980, vol. 28, p. 33.
32. M.R. Louthan, Jr.: *Current Solutions to Hydrogen Problems in Steels*, C.G. Interrante and G.M. Pressouyre, eds., ASM, Metals Park, Ohio, 1982, pp. 454-461.
33. C.L. Briant and S.K. Banerji: *Int. Met. Rev.*, 1978, vol. 23, p. 164.
34. Y. Takeda and C.J. McMahon, Jr.: *Metall. Trans. A*, 1981, vol. 12A, p. 1251.
35. Y. Takeda and C.J. McMahon, Jr.: *Metall. Trans. A*, 1982, vol. 13A, p. 111.
36. S. Nagashima, T. Ooka, S. Sekino, H. Mimura, T. Fujishima, S. Yano, and H. Sakurai: *Trans. Iron Steel Inst. Japan*, 1971, vol. 58, p. 402.
37. S. Nagashima, T. Ooka, S. Sekino, H. Mimura, T. Fujishima, S. Yano, and H. sakurai: *Tetsu-to-Hagane*, 1972, vol. 58, p. 128.
38. H.J. Kim, Y.H. Kim, and J.W. Morris, JR.: *Metall. Trans. A*, ( in press).
39. R.D. McCright: *Stress Corrosion Cracking and Hydrogen Embrittlement of Iron Base Alloys*: NACE, Houston, TX, 1977, pp. 306-324.
40. I.M. Bernstein: *Metall. Trans.*, 1970, vol.1, p. 3143.



41. R. Heidersbach and B. Allen: Current Solutions to Hydrogen Problems in Steels, C.G. Interrante and G.M. Pressouyre, eds., ASM, Metals Park, Ohio, 1982, pp. 104-105.
42. R.L. Miller: Trans. ASM, 1964, vol. 57, p. 892
43. C.K. Syn, B. Fultz, and J.W. Morris, Jr.: Metall. Trans. A, 1978, vol. 9A, p. 1635.
44. S. Hogmark, H. Swahn, and O. Vingsbo: Ultramicroscopy, 1975, vol. 1, p. 113.
45. S. Matsuda, T. Inoue, H. Mimura, and Y. Okamura: Toward Improved Ductility and Toughness, Climax Molybdenum Development Co. Japan Ltd., Kyoto, 1972, pp. 45-66.
46. H. Hayakawa and A. Imamura: Bull. of JIM, 1979, vol. 18, p. 282.
47. O.J. Klingensmaier: Modern Electroplating, F.A. Lowenheim, ed., John Wiley & Sons, New York, NY, 1974, pp. 250-265.
48. I. Olefjord: Int. Met. Rev., 1978, vol. 23, p. 149.
49. C.L. Briant and S.K. Banerji: Treatise on Materials Science and Technology, vol. 25, C.L. Briant and S.K. Banerji, eds., 1983, Academic Press, New York, NY, pp. 21-58.
50. R.O. Ritchie: Metall. Trans. A, 1977, vol. 8A, p. 1131.
51. S.K. Banerji, C.J. McMahon, Jr., and H.C. Feng: Metall. Trans. A, vol. 9A, p. 237.
52. T. Ogura, C.J. McMahon, Jr., H.C. Feng, and V. Vitek: Acta Metall., 1978, vol. 26, p. 1317.
53. C.J. Briant and S.K. Banerji: Metall. Trans. A, 1982, vol. 13A, p. 827.
54. J.E. Casta and A.W. Thompson: Metall. Trans. A, 1981, vol. 12A, p. 761-55. P.V. Ramasubramanian and D.F. Stein: Metall. Trans., 1973, vol. 4, p. 1735.
56. C. Pichard, J. Rieu, and C. Goux: Metall. Trans. A, 1976, vol. 7A, p. 1181.
57. G.J. Spaeder, R.M. Brown, and W.J. Murphy: Trans. ASM, 1967, vol. 60, p. 418.
58. C.L. Briant, H.C. Feng, and C.J. McMahon, Jr.: Metall. Trans. A, 1978, vol. 9A, p. 625.
59. A.H. Ucisik, C.J. McMahon, Jr. and H.C. Feng: Metall. Trans. A, 1978, vol. 9A, p. 604.

60. D.Y. Lee, E.V. Barrera, J.P. Stark, and H.L. Marcus: *Metall. Trans. A*, 1984, vol. 15A, p. 1415.
61. S.K. Banerji, C.L. Briant, and C.J. McMahon, Jr.: *Mechanisms of Environment Sensitive Cracking of Materials*, P.R. Swan, F.P. Ford, and A.R.C. Westwood, eds., 1977, The Metal Society, Multiplex Techniques Ltd., Orpington, Kent; pp. 437-445.
62. S.M. Bruemmer, R.H. Jones, M.T. Thomas, and D.R. Baer: *Scripta Metallurgica*, 1980, vol. 14, No. 1, p. 137.
63. K.S. Shin and M. Meshii: *Acta Metall.*, 1983, vol. 31, No. 10, p. 1559.
64. B.P. Craig and G. Krauss: *Metall. Trans. A*, 1980, vol. 11A, p. 1799.
65. K. Yoshino and C.J. McMahon, Jr.: *Metall. Trans.*, 1974, vol. 5, p. 363.
66. R. Viswanathan and S.J. Hudak: *Effect of Hydrogen on Behavior of Materials*, A.W. Thompson and I.M. Bernstein, eds., 1976, AIME, New York, NY, pp. 262-272.
67. R.M. Latanision and H. Opperhauser, Jr.: *Metall. Trans.*, 1974, vol. 5, p. 483.
68. R.M. Latanision and H. Opperhauser, Jr.: *Metall. Trans. A*, 1975, vol. 6A, p. 233.
69. K.S. Shin and M. Meshii: *Scripta Metallurgia*, 1983, vol. 17, p. 1121.
70. R. Kiessling and N. Lange: *Non-Metallic Inclusions in Steel*, 2nd ed., The Metals Society, London, 1978, pp. 97-145.
71. C.L. Briant and S.K. Banerji: *Metall. Trans. A*, 1981, vol. 12A, p. 309.
72. B.J. Schulz and C.J. McMahon, Jr.: *Metall. Trans.*, 1973, vol. 4, p. 2485.
73. W.C. Leslie: *The Physical Metallurgy of Steels*, McGraw-Hill Book Co., New York, NY, 1981, p. 181.
74. D.J. Widgery and T. Boniszewski: *JISI*, 1966, vol. 204, p. 53.
75. M. Murakami, K. Shibata, K. Nagai, and T. Fujita: *Trans. ISI Japan*, 1983, vol. 23, No. 10, p. 808.
76. H. Ohtani, H.C. Feng, and C.J. McMahon: *Metall. Trans.*, vol. 5, p. 516.
77. M.P. Seah, P.J. Spencer and E.P. Hondros: *Proc. R. Soc. London Ser.*, 1973, vol. A 335, p. 191.

78. C.S. Smith: Trans. ASM, 1953, vol. 45, p. 533.
79. C.W. Marshall, R.H. Heheman and A.R. Troiano: Trans. ASM, 1972, vol. 55, p. 135.
80. W.W. Gerberich and C.E. Hartbower: Fundamental Aspects of Stress Corrosion Cracking, NACE, Houston, TX, 1969, pp. 420-438.
81. S. Hinotani, F. Terasaki and F. Nakasato: Proc. JIMIS-2, Hydrogen in Metals, suppl. to Trans. Japan Inst. Metals, 1980, vol. 21, p. 421.
82. F. Nakasato and I.M. Bernstein: Metall. Trans. A, 1978, vol. 9A, p. 1317.
83. Y. Kikuta, T. Araki and T. Kuroda: Fractography in Failure Analysis, ASTM STP 645, B.M. Strauss and W.H. Cullen eds., American Society for Testing and Materials, 1978, pp. 107-127.
84. A.S. Tetelman and W.D. Robertson: Trans. TMS-AIME, 1962, vol. 224, p. 775.
85. A.S. Tetelman and W.D. Robertson: Acta Metall., 1963, vol. 11, p. 415.
86. M. Gell and W.D. Robertson: Acta Metall., 1966, vol. 14, p. 481.
87. A.S. Tetelman and A.J. McEvily, Jr.: Fracture of Structural Materials, John Wiley & Sons, Inc., New York, NY, 1967, pp. 40-45.
88. J.I. Kim: Ph.D. Thesis, Department of Materials Science and Mineral Engineering, University of California, Berkeley, CA, 1979.
89. M. Nagumo, H. Morikawa, and K. Miyamoto: Proc. JIMIS-2 Hydrogen in Metals, suppl. to Trans. Japan Inst. Metals, 1980, vol. 21, pp. 405-408.
90. Y. Kikuta, T. Araki, and S. Ochiai: 2nd International Congress on Hydrogen in Metals, Pergamon Press, 1977, 3A3.
91. Y. Kikuta and T. Araki: Hydrogen Effects in Metals, I.M. Bernstein and A.W. Thompson, eds., TMS-AIME, Warrendale, Pa, 1981, pp. 309-318.
92. C.J. McMahon, *ibid.*, pp. 219-234.
93. J.I. Gilman: Trans. TMS-AIME, 1958, vol. 212, p. 783.
94. H. Kimura, H. Matsui and S. Takaki: Mechanical Properties of BCC Metals, M. Meshii, ed., TMS-AIME, Warrendale, PA, 1982, pp. 125-133.
95. Z. Nishiyama: Martensitic Transformation, Academic Press, New York, NY, 1978, pp. 1-13.
96. G. Krauss and A.R. Marder: Metall. Trans., 1971, vol. 2, p. 2343.

97. G. Thomas: Metall. Trans., 1971, vol. 2, p. 2373.
98. W.S. Owen, E.A. Wilson, and T. Bell: High Strength Materials, V.F. Zackay, ed., John Wiley & Sons Inc., New York, NY, 1965; pp. 167-212.
99. P.M. Kelley and J. Nutting: Proc. Roy. Soc., 1960, (A), vol. 259, p. 45.
100. G.R. Speich and P.R. Swann: JISI, 1965, vol. 203, p. 480.
101. A.R. Marder and G. Krauss: Trans. ASM, 1967, vol. 60, p. 651.
102. A. Sauveur and C.H. Chou: Trans. TMS-AIME, 1929, vol. 84, p. 350.
103. R.F. Mehl, C.S. Barret, and D.W. Smith: Trans. TMS-AIME, 1933, vol. 105, p. 307.
104. A.B. Grenninger and A.R. Troiano: Trans. TMS-AIME, 1940, vol. 140, p. 307.
105. G.R. Speich and H. Warlimont: JISI, 1968, vol. 206, p. 385.
106. C.A. Apple, R.N. Caron, and G. Krauss: Metall. Trans., 1974, vol. 5, p. 593.
107. F.J. Schoen, J.L. Nilles, and W.S. Owen: Metall. Trans., 1971, vol. 2, p. 2489.
108. R.G. Bryans, T. Bell and V.M. Thomas: The Mechanism of Phase Transformations in Crystalline Solids, Inst. of Metals, Monograph No.33, 1969, p.p. 131-188.
109. T. Bell and W.S. Owen: JISI, 1967, vol. 205, p. 428.
110. C.M. Wayman and C.J. Altstetter: Acta Metall., 1962, vol. 10, p. 992.
111. J.D. Bolton and E.R. Petty: Met. Sci. J., 1971, vol. 5, p. 166.
112. A. Gilbert and W.S. Owen: Acta Metall., 1962, vol. 10, p. 45.
113. K. Wakasa and C.M. Wayman: Acta Metall., 1981, vol. 29, p. 991.
114. A.R. Marder and G. Krauss: Trans. ASM, 1969, vol. 62, p. 957.
115. J.M. Chilton, C.J. Barton and G.R. Speich: JISI, 1970, vol. 208, p. 184.
116. B.P.J. Sandvik and C.M. Wayman: Metall. Trans. A, 1983, vol. 14A, p. 809.
117. M.G.A. Biswas and I. Codd: JISI, 1968, vol. 206, p. 494.

118. J.R. Rice: Stress Corrosion Cracking and Hydrogen Embrittlement of Iron Base Alloys, NACE, Houston, TX, 1977, pp. 11-15.
119. J.R. Rice and M.A. Johnson: Inelastic Behavior of Solids, M.F. Kanninen, W.F. Adler, A.R. Rosenfield, and R.I. Jaffee, eds., McGraw-Hill Book Company, New York, NY, 1970, pp. 641-670.
120. J.I. Kim, C.K. Syn, and J.W. Morris, Jr.: Metall. Trans. A, 1983, vol. 14A, p. 93.
121. M.F. Stevens: Ph.D. Thesis, Department of Metallurgical Engineering  $\beta$  Materials Science, Carnegie-Mellon University, 1984.
122. W.W. Gerberich, Y.T. Chen and C.S.T. John: Metall. Trans. A, 1975, vol. 6A, p. 1485.
123. C.A. Tatro, R.G. Liptai, and D.W. Moon: Stress Corrosion Cracking and Hydrogen Embrittlement of Iron Base Alloys, NACE, Houston, TX, 1977, pp. 509-518.
124. G.B. Olson and M. Cohen: Acta Metall., 1979, vol. 27, p. 1907.
125. G.B. Olson: Acta Metall., 1981, vol. 29, p. 1475.
126. G.B. Olson and M. Cohen: Solid-Solid Phase Transformations, H.I. Aaronson, D.E. Laughlin, R.F. Sekerka, and C.M. Wayman, eds., TMS-AIME, Warrendale, PA, 1982, pp. 1209-1213.
127. M.R. Louthan, Jr., R.P. McNitt and R.D. Sisson: Advanced Techniques for Characterizing Hydrogen in Metals, N.F. Fiore and B.J. Berkowitz, eds., TMS-AIME, Folrham Park, NJ, 1982, pp. 25-41.
128. J. Chene: Current Solutions to Hydrogen Problems in Steels, C.G. Interrante and G.M. Pressouyre, eds., ASM, Metals Park, Ohio, 1982, pp. 263-271.
129. M. Anouturier, *ibid*, pp. 407-412.
130. H. Hanninen and T. Hakkarainen: Metall. Trans. A, 1979, vol. 10A, p. 1196.
131. B.D. Craig and N.G. Krauss: Hydrogen Effects in Metals, I.M. Bernstein and A.W. Thompson, eds., TMS-AIME, Warrendale, PA, 1981, p. 795.
132. C. Paes de Oliveira, M. Anouturier and P. Lacombe: Corrosion, NACE, 1980, vol. 36, p. 53.
133. J.I. Kim, H.J. Kim, and J.W. Morris, Jr.: Metall. Trans. A, 1984, vol. 15A, p. 2113.
134. R.O. Ritchie, M. Castro-Cedeno, V.F. Zackay, and E.R. Parker: Metall. Trans. A, 1978, vol. 9A, p. 35.

135. T.G. Gooch: *Weld. J.*, 1974, vol. 53(7), p. 287s.
136. C. Chen, A.W. Thompson, and I.M. Bernstein: *Weldments-Physical Metallurgy and Failure Phenomena, Proceedings, 5th Bolt on Landing Conference*, R.J. Christoffel, E.F. Nippes, and H.D. Solomon, eds., General Electric Company, Schenectady, NY, 1979, pp. 219-230.
137. S.M. Toy and A. Phillips: *Weld. J.*, 1970, vol. 49(11), p. 497s.
138. J.I. Kim and J.W. Morris, Jr.: *Metall. Trans. A*, 1981, vol. 12A, p. 1957.
139. G. Kurdjumov and G. Sachs: *Z. Physik*, 1930. vol. 64, p. 325.
140. Z. Nishiyama: *Sci. Rep. Tohoku University*, 1934, vol. 23, p. 637.
141. G. Wassermann: *Mitt. K-W-I Einsenforsch*, 1935, vol. 17, p. 149.
142. C.N. Sastry, K.H. Kahn, and W.E. Wood: *Metall. Trans. A*, 1982, vol. 13A, p. 676.
143. I.M. Bernstein, A.W. Thompson, F. Gutierrez-Solana and L. Christodoulou: *Current Solutions to Hydrogen Problems in Steels*, C.G. Interrante and G.M. Pressouyre, ASM, Metals Park, Ohio, 1982, pp. 259-262.
144. J.W. Morris, Jr., C.K. Syn, J.I. Kim, and B. Fultz: *Proceedings, International Conference on Martensitic Transformations*, W. Owen, ed., M.I.T. Press, Cambridge, MA, 1979, pp. 572-577.
145. M. Murakami, K. Shibata, and T. Fujita: *Proceedings International Cryogenic Materials Conference*, Kobe, Japan, K. Tachikawa and A. Clark, eds., Butterworths, London, 1982, pp. 356-359.
146. H. Haga and H. Mimura: *Trans. JIM*, 1972, vol. 13, p. 155.
147. R. Garber, P.J. Grobner, and D.L. Sponseller: *Hydrogen Effects in Metals*, I.M. Bernstein and A.W. Thompson, eds., TMS-AIME, Warrendale, Pa, 1981, pp. 361-368.
148. I.M. Bernstein and A.W. Thompson: *Int. Met. Rev.*, 1976, vol. 21, p. 269.
149. R. Viswanathan and S.J. Hudak, Jr.: *Metall. Trans. A*, 1977, vol. 8A, p. 1633.
150. H.J. Kim and J.W. Morris, Jr.: *Weld. J.*, 1983, vol. 62(8), p. 210s.
151. H.J. Kim: *Ph.D. Thesis, Dept. of Materials Science and Mineral Engineering, University of California, Berkeley, CA, 1982.*
152. Y.H. Kim and J.W. Morris, Jr.: *Metall. Trans. A*, 1983, vol. 14A, p. 1883.

153. Y.H. Kim, H.J. Kim and J.W. Morris, Jr.: Metall. Trans. A, (in Press).
154. C.A. Zannis, P.W. Holsberg, and E.C. Dunn, Jr.: Weld. J., 1980, vol. 59(2), p. 355s.

### FIGURE CAPTIONS

- Fig. 1. Fracture modes in hydrogen assisted fracture. (5.5 Ni steel)  
 (A) dimple rupture mode (B) transgranular brittle mode  
 (C) intergranular mode
- Fig. 2. Round tensile specimen geometry.
- Fig. 3. Charpy size three point bend specimen geometry.
- Fig. 4. AES specimen geometry in-situ fracture.
- Fig. 5. Scanning electron fractographs of the 5.5 Ni steel specimens  
 (A) homogenized at 1250 C (B) homogenized at 1250 C  
 (C) homogenized at 1250 C and tempered at 450 C  
 (D) homogenized at 1250 C and austenitized at 800 C  
 (E) homogenized at 1250 C and austenitized at 1000 C  
 (F) homogenized at 1100 C
- All specimens except (B) were broken at room temperature after hydrogen charging and specimen (B) was broken at 77 K without hydrogen charging.
- Fig. 6. Scanning electron fractograph and AES spectrum obtained from an intergranular fracture surface before and after sputtering (A and D) and from a dimple rupture surface (untempered 5.5Ni steel).
- Fig. 7. Schematic diagram of a three point bending fixture and a charpy size specimen.
- Fig. 8. Scanning electron fractographs showing precipitated austenite on the grain boundaries. The numbers in upper right region of the figures represent the tempering time at 590 C (5.5Ni steel).
- Fig. 9. Scanning electron fractographs showing the grain boundaries of the ALT specimen (5.5Ni steel). (A) shows three grain boundaries and (B) shows detailed view of a grain boundary showed in Fig. (A).
- Fig. 10. The load displacement curves of three point bend specimens of 5.5Ni steel tested before and after hydrogen charging.
- Fig. 11. Scanning electron fractographs of a three point bend specimen broken in the uncharged condition. (QT treated 5.5 Ni steel)  
 (A) Low magnification fractograph showing the ductile rupture fracture mode. (B) Higher magnification view of region outlined in (A).



- Fig. 12. Scanning electron fractographs of a three point bend specimen broken after hydrogen charging. (QT treated 5.5 Ni steel) (A) Low magnification fractograph showing the presence of transgranular brittle fracture. (B) High magnification view of transgranular brittle fracture. (C) High magnification view of a region of ductile fracture.
- Fig. 13. Scanning electron fractographs of a tensile specimen broken at room temperature before hydrogen charging.
- Fig. 14. Scanning electron fractographs of a tensile specimen broken after hydrogen charging (QT treated 5.5Ni steel). (A) Low magnification fractograph. (B) High magnification view showing transgranular brittle fracture. (C) High magnification view showing ductile fracture.
- Fig. 15. Conjugated fracture surfaces of 5.5Ni steel. The three-point bend specimen was broken at room temperature after hydrogen charging. Arrows represent the crack propagation direction.
- Fig. 16. Schematic representation of a model for slip plane decohesion proposed by McMahon.
- Fig. 17. Optical micrograph and schematic diagram showing grain, packet and lath. (untempered 5.5Ni steel)
- Fig. 18. Transmission electron micrograph of tempered HY 130 steel.
- Fig. 19. Another example of transmission electron micrograph of tempered HY 130 steel.
- Fig. 20. Transmission electron micrograph showing low angle lath boundaries in QT treated 5.5Ni steel
- Fig. 21. Transmission electron micrograph showing twin-related laths in QT treated 5.5Ni steel. (A) shows a bright field image. Fig.(B) and (C) are dark field images taken from spots indicated by arrows in selected area diffraction patterns.
- Fig. 22. Scanning electron micrographs of tempered 5.5Ni steel broken after hydrogen charging. (A) macroscopic view showing transgranular brittle fracture. (B) macroscopic view showing shear-like fracture. (C) high magnification view outlined in (A). (D) high magnification view outlined in (B).
- Fig. 23. Scanning electron micrographs showing quasicleavage fracture (untempered 5.5Ni steel). The specimen was broken at 77 K in an uncharged condition.
- Fig. 24. Scanning electron micrographs showing needle-like features. The specimen was broken in tension at room temperature after hydrogen charging. (QLT treated 5.5Ni steel).

- Fig. 25. Scanning electron micrographs of a three point bend specimen. The specimen was broken at room temperature after hydrogen charging (as received 5.5Ni steel).
- Fig. 26. Scanning electron micrograph of the 5.5Ni steel specimen embrittled by hydrogen. Shear rupture fracture connected two adjacent hydrogen assisted transgranular cracks.
- Fig. 27. Scanning electron micrographs showing hydrogen-assisted transgranular fracture and shear-like dimple rupture between transgranular fracture regions (untempered 5.5Ni steel).
- Fig. 28. Optical micrograph of the cross section of the fracture surface in the untempered 5.5Ni steel specimen embrittled by hydrogen. The fracture surface was protected by iron plating. (A) Low magnification picture showing profile surface. (B) High magnification view of the fracture surface showing in (A).
- Fig. 29. Optical micrograph of a profile specimen (untempered 5.5Ni steel).
- Fig. 30. Optical micrographs of a plane perpendicular to the fracture surface in a hydrogen-charged specimen, showing secondary cracks ahead of the tip of an arrested crack. Photograph (B) was taken after etching with nital to reveal the sample microstructure (untempered 5.5 Ni steel).
- Fig. 31. Optical micrograph of an etched cross section through the specimen showing crack propagation along lath boundaries and crack deflection at packet boundaries (untempered 5.5Ni steel).
- Fig. 32. Scanning electron micrograph showing hydrogen assisted cracks. The specimen was etched with 2% nital solution (tempered HY 130 steel).
- Fig. 33. Transmission electron fractograph showing the fracture surface (open arrows) and 3 subsurface interlath cracks (QT treated 5.5Ni steel).
- Fig. 34. Transmission electron fractograph showing the fracture surface (open arrows), apparent translath steps in the fracture surface (\*), and subsurface interlath microcracks (small arrows) (QT-treated 5.5Ni steel).
- Fig. 35. Transmission electron fractograph showing the fracture surface (open arrows), a subsurface interlath crack (small arrow), and a subsurface diffraction pattern (QT treated 5.5 Ni steel).
- Fig. 36. Transmission electron fractograph showing the fracture surface (large arrows), an interlath microcrack (a), and a microcrack within a lath (b) (QT treated 5.5Ni steel).

- Fig. 37. Transmission electron fractograph showing the fracture surface (arrow heads) and interlath microcracks (small arrows), (QT-treated 5.5 Ni steel).
- Fig. 38. Transmission electron fractographs showing the fracture surfaces (arrow heads) and interlath microcracks (arrows). Both are taken from the same area but with different tilting conditions.
- Fig. 39. Transmission electron fractographs showing the fracture surface (open arrows), interlath microcracks (arrow heads), and diffraction patterns taken from a Ni plated layer (A) and a subsurface region (B).
- Fig. 40. High voltage transmission electron fractograph showing the fracture surface (open arrows) (QT-treated 5.5 Ni steel).
- Fig. 41. Scanning electron micrograph of the hydrogen assisted transgranular brittle fracture surface showing distorted hexagonal etch pits (QT-treated 5.5 Ni steel).
- Fig. 42. Scanning electron micrograph of the quasicleavage fracture surface showing square etch pits. (untempered 5.5 Ni steel)
- Fig. 43. Transmission electron micrograph showing the microstructure of 5.5 Ni steel in the QT condition.
- Fig. 44. Transmission electron micrograph showing precipitated austenite at the packet boundaries (QT treated 5.5 Ni steel).
- Fig. 45. Transmission electron micrographs showing the microstructure of 5.5 Ni steel in the QLT condition. Figure (B) is a dark field micrograph taken from a diffraction spot, showing precipitated austenite along the martensite lath boundaries. Diffraction pattern shows the K-S relationship between austenite and martensite.
- Fig. 46. Transmission electron micrograph of an untempered 5.5 Ni steel specimen. (A) Bright field image (B) Dark field image showing retained austenite.
- Fig. 47. Transmission electron micrographs showing precipitated austenite in QLT treated 5.5 Ni steel. Diffraction pattern shows the N-W relationship between austenite and martensite.
- Fig. 48. The load displacement curves of three point bend specimen of 5.5 Ni steel in the QT and QLT condition before and after hydrogen charging.
- Fig. 49. Scanning electron fractographs showing the fracture surfaces of the QT and QLT specimens after hydrogen charging and fracture in three-point bending (5.5 Ni steel).

- Fig. 50. Transmission electron fractographs of a hydrogen-charged 5.5 Ni QLT specimen. The fracture surface is marked by the open triangles in micrograph (A). The solid arrows point to interlath microcracks just beneath the fracture surface. Micrograph (B) is a high magnification of the region designated (B) in micrograph (A). The arrows point to interlath microcracks, which tend to lie at the periphery of fresh martensite islands, as evidenced by the cracks at the upper and lower arrows.
- Fig. 51. Transmission electron micrograph showing the substructure just below the fracture surface in a hydrogen-charged 5.5Ni steel QLT specimen. The arrows point to interlath microcracks which lie at the edges of fresh martensite particles.
- Fig. 52. Another example of transmission electron micrograph showing the substructure just below the fracture surface.
- Fig. 53. Another example of transmission electron micrograph showing the substructure just below the fracture surface.
- Fig. 54. Schematic drawing illustrating the probable mechanism of hydrogen embrittlement in the presence of interlath austenite. (1) The initial structure of dislocated martensite with interlath austenite. (2) The interlath martensite transforms to martensite in the stressed region ahead of the crack tip. (3) The transformation volume change imposes a tensile stress across the boundary, which has been weakened by hydrogen, and nucleates microcracks. (4) The microcracks grow and coalesce into macrocracks.
- Fig. 55. Optical micrographs of a plane perpendicular to the quasicleavage fracture surface in an untempered 5.5Ni steel broken at 77 K.
- Fig. 56. Transmission electron micrograph showing the substructure below the ductile fracture surface in an as-received 5.5 Ni steel specimen. (A) bright field image (B) dark field image of the precipitated austenite which still remained (C) dark field image of mechanically transformed martensite.
- Fig. 57. Optical micrographs of 12 Ni steel. (A) annealed and quenched

Table 1. Alloy Compositions

---

Chemical Composition (wt. %)

---

	C	Si	Mn	P	S	Ni	Cr	Mo	V	Ti
5.5 Ni	0.06	0.20	1.21	0.008	0.01	5.86	0.69	0.20	-	-
HY 130	0.08	0.03	0.84	0.01	0.005	5.11	0.59	0.59	0.08	-
12 Ni	0.006	-	-	0.001	0.002	12.07	-	-	-	0.20

---

Table 2. Etchant and Etching Time

## (1) Etchant A

Reagent:	HCl	1 cc
	H <sub>2</sub> O <sub>2</sub>	20 cc
	H <sub>2</sub> O	25cc
Time:	4 sec.	

## (2) Etchant B

Reagent:	FeCl <sub>3</sub> -6H <sub>2</sub> O	20 cc
	HCl	10 cc
	H <sub>2</sub> O	100 cc
Time:	40 sec.	

## (3) Etchant C

Reagent:	HCOOH	25 cc
	H <sub>2</sub> O <sub>2</sub>	25 cc
	C <sub>2</sub> H <sub>5</sub> OH	25 cc
	H <sub>2</sub> O	25 cc

Table 3. Outgassing Experiment Data

		(No H)	(H)	(baked)
Y.S.	(MPa)	600	619	604
U.T.S.	(MPa)	751	752	749
R.A.	( % )	79.5	61.2	78.7
Tot. Elong.*	( % )	29.9	19.3	29.1

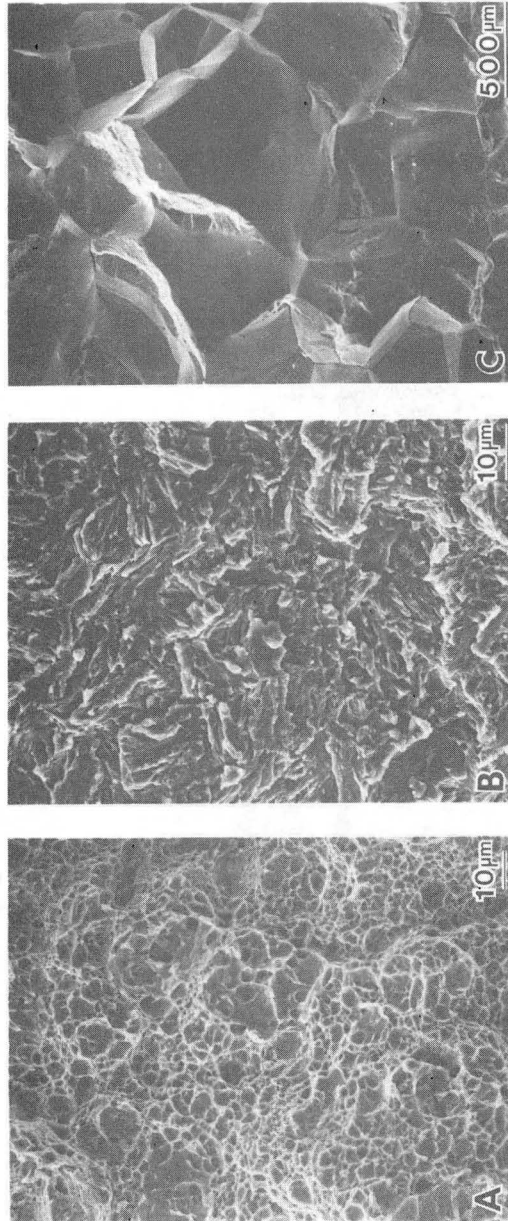
\* 25.4 mm (1 in) gauge length

Table 4. Tensile Test Data of 5.5 Ni Steel

		QT		QLT	
		(No H)	(H)	(No H)	(H)
Y.S.	(MPa)	737	757	590	616
	(ksi)	107	110	86	89
U.T.S.	(MPa)	779	758	735	616
	(ksi)	113	110	107	97
R.A.	(%)	79.2	17.8	79.7	2.9
Tot. Elong.*	(%)	29.8	5.6	34.6	2.2

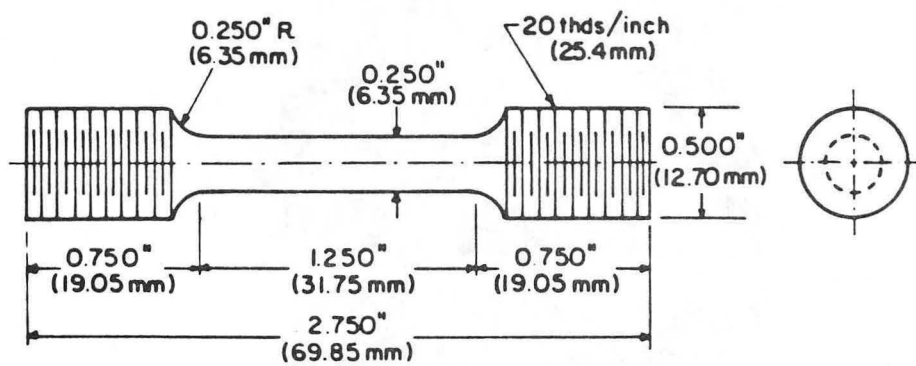
\* 25.4 mm (1 in) gauge length





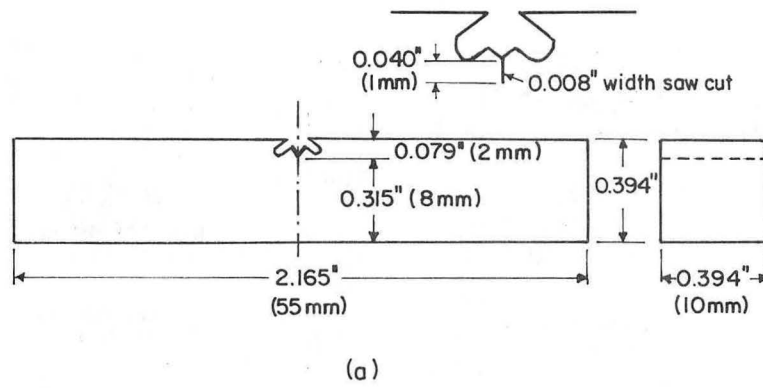
XBB 830-8234

Fig. 1



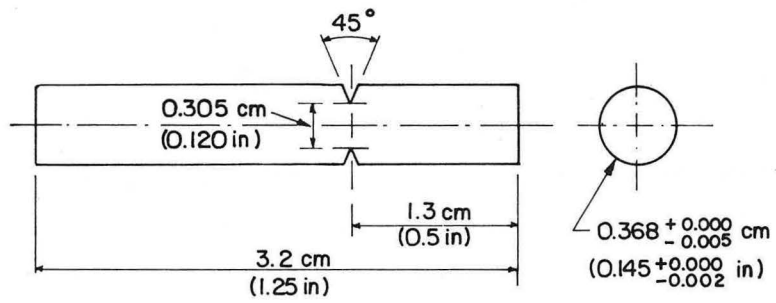
XBL 856-2711

Fig. 2



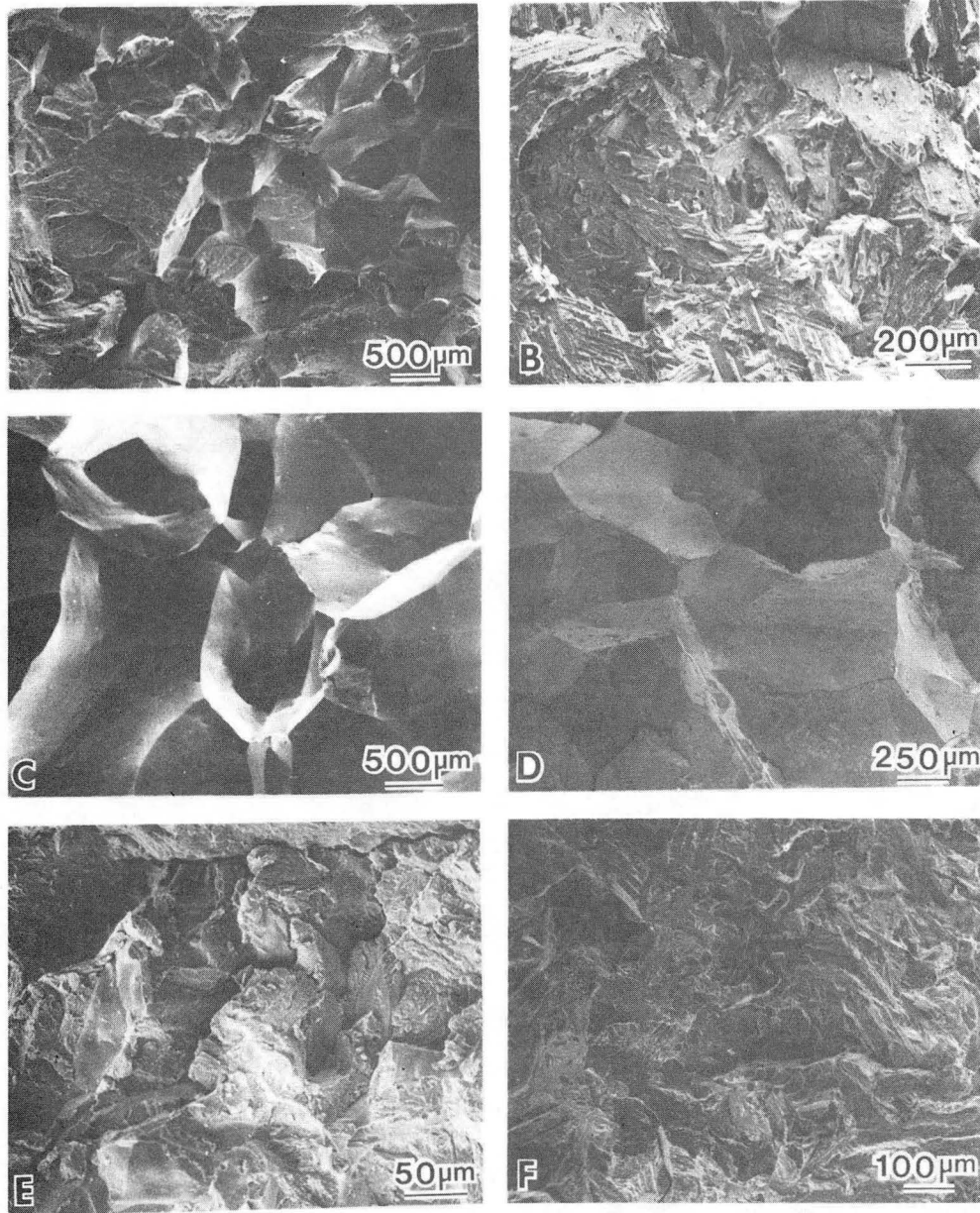
XBL 827-6028

Fig. 3



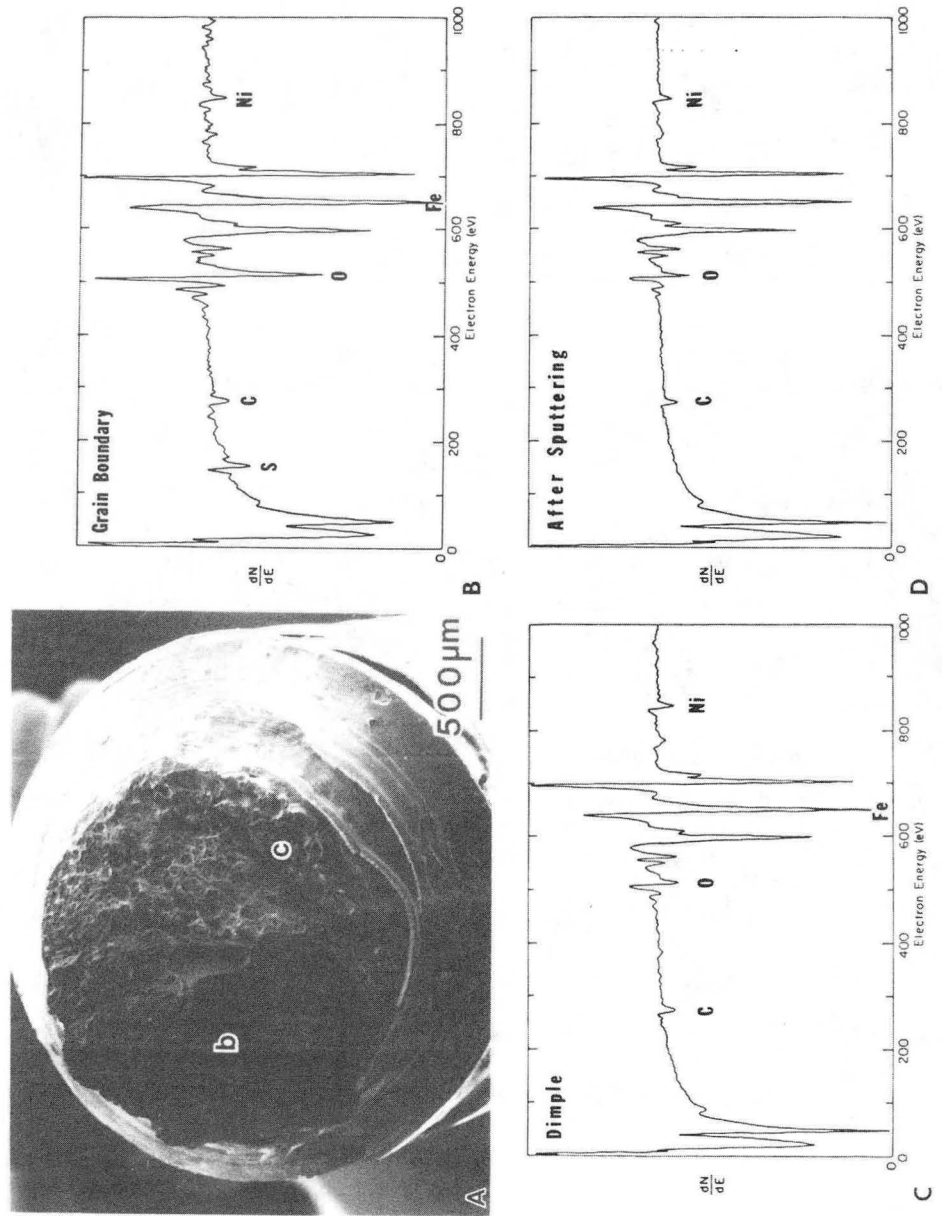
XBL 812-5242

Fig. 4



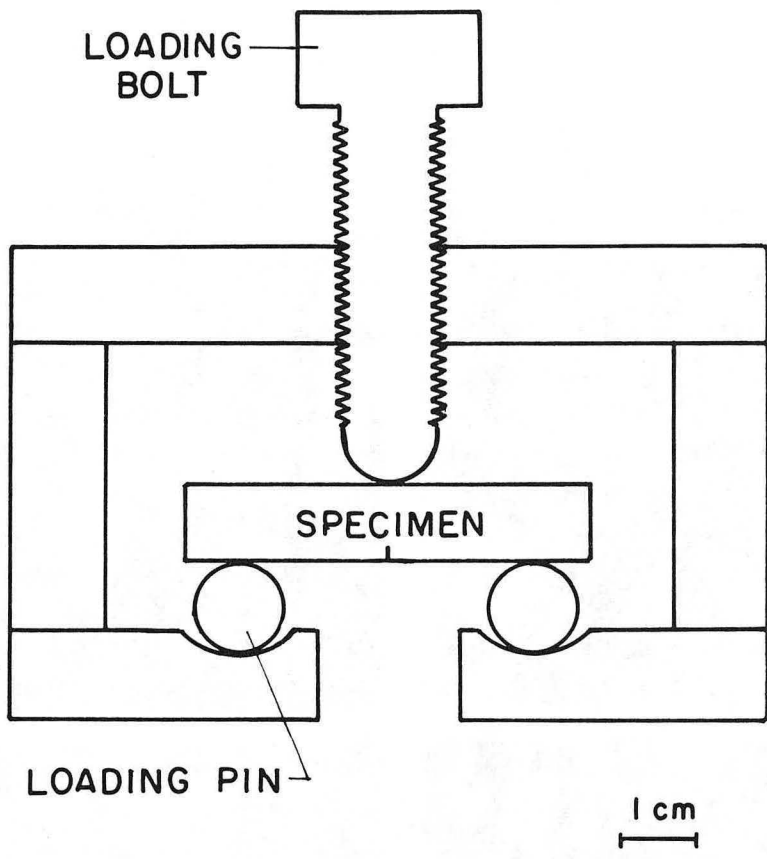
XBB 854-3225

Fig. 5



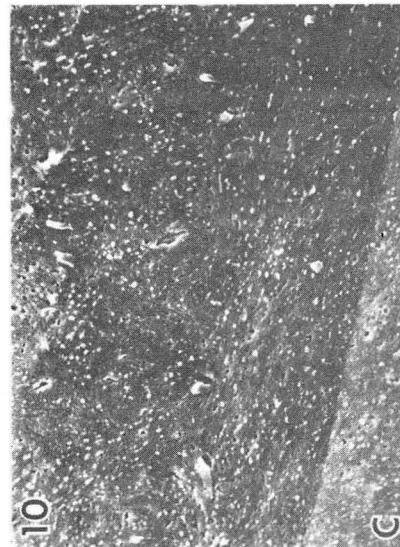
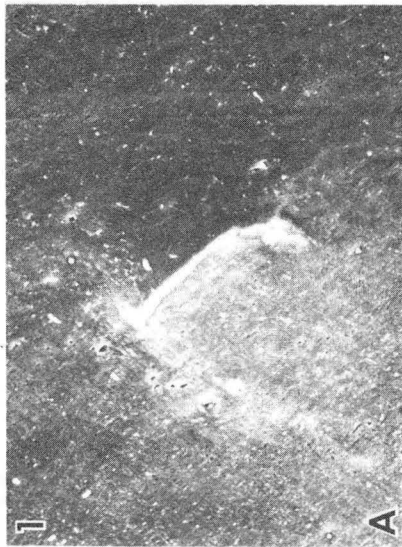
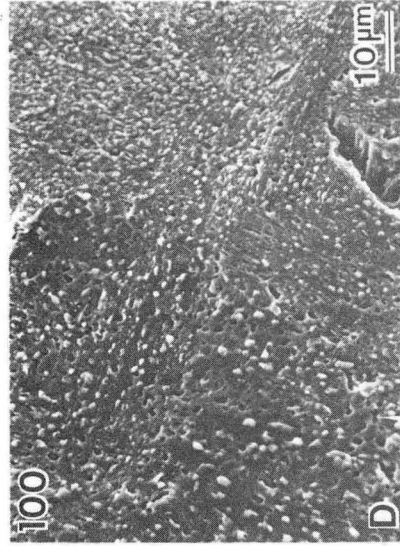
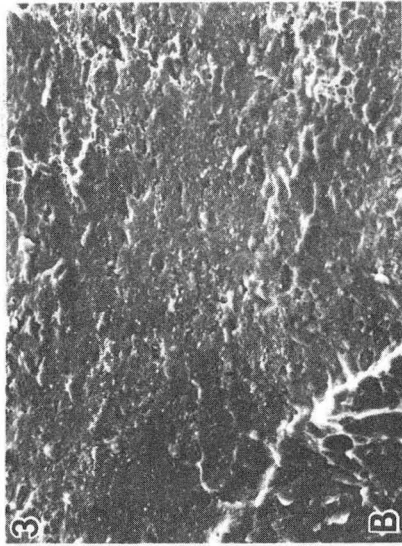
XBB 830-9591A

Fig. 6



XBL 855-2410

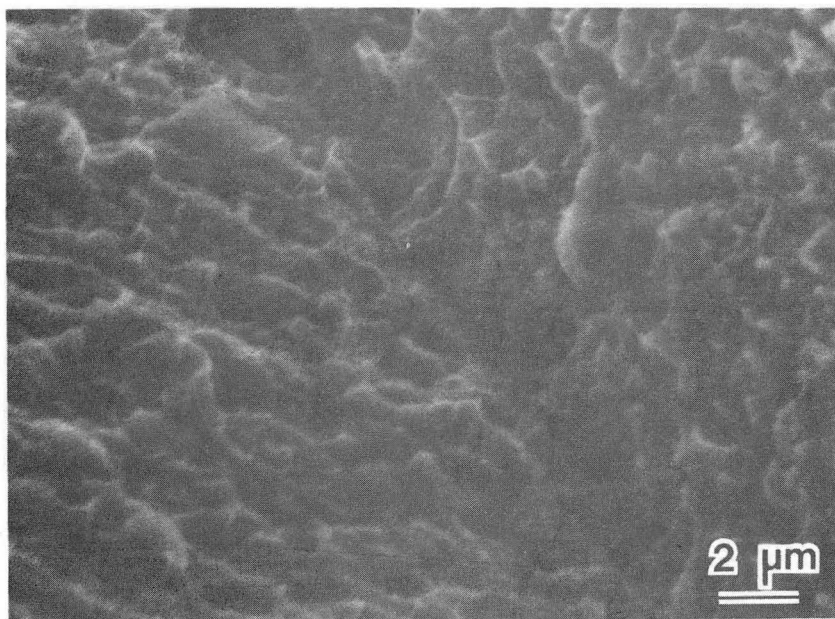
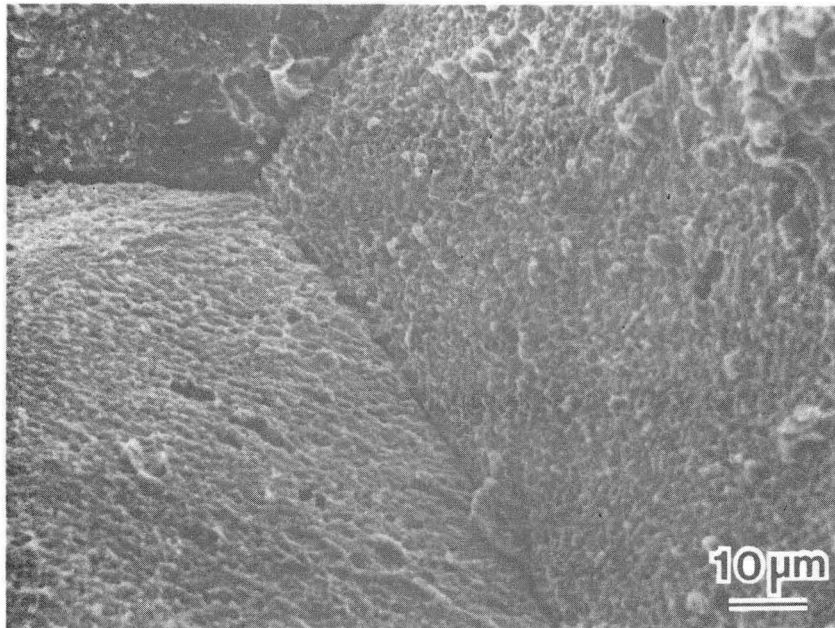
Fig. 7



XBB 851-34

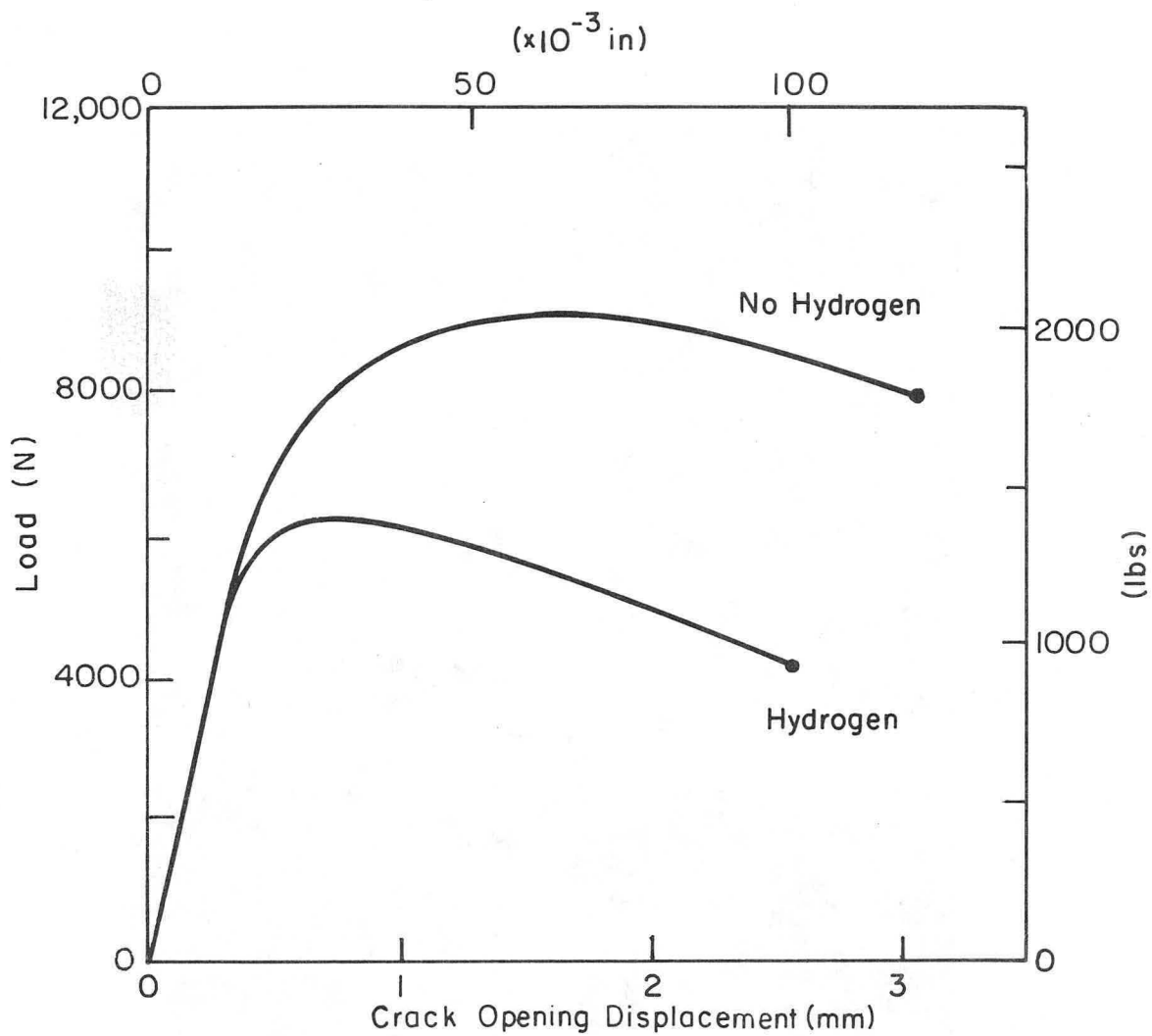
Fig. 8





XBB 851-33

Fig. 9



XBL 833 - 536 7A

Fig. 10

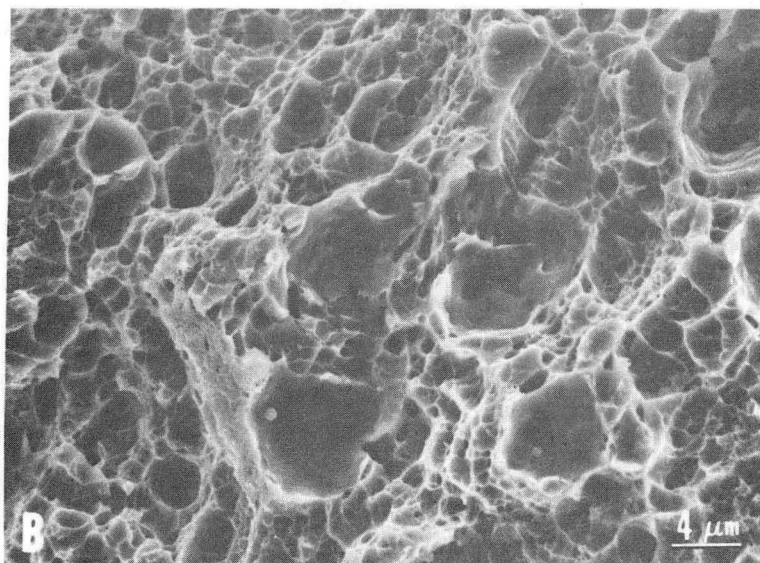
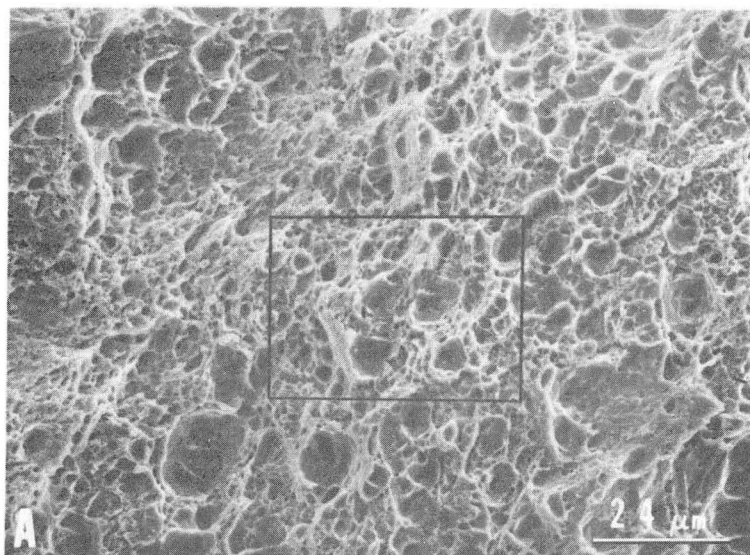


Fig. 11

XBB 829-8369

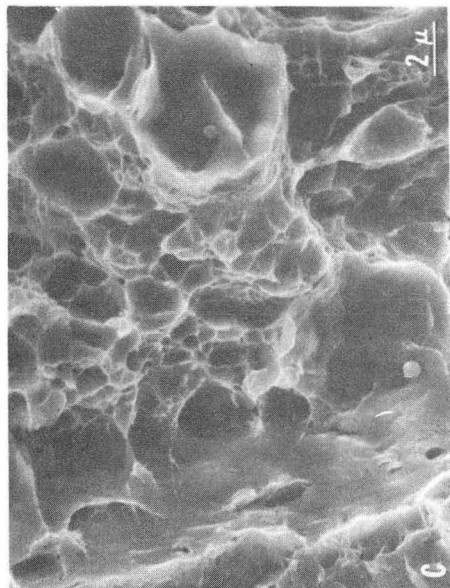
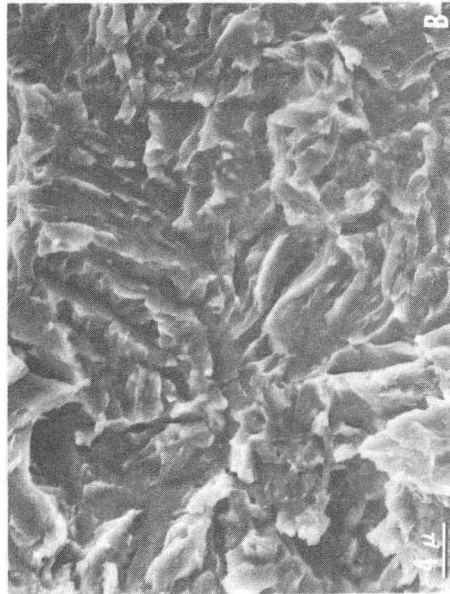
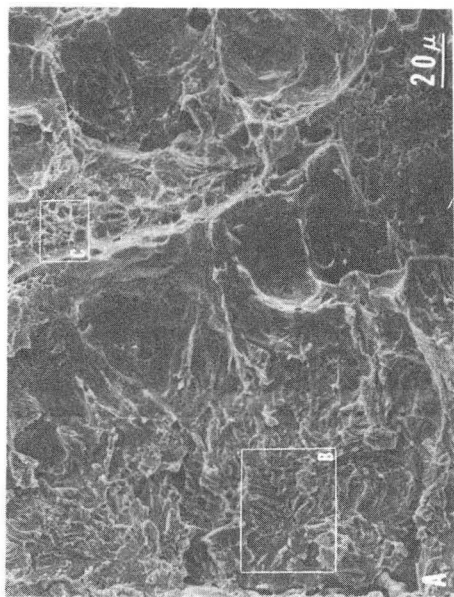


Fig. 12

XBB 820-9437

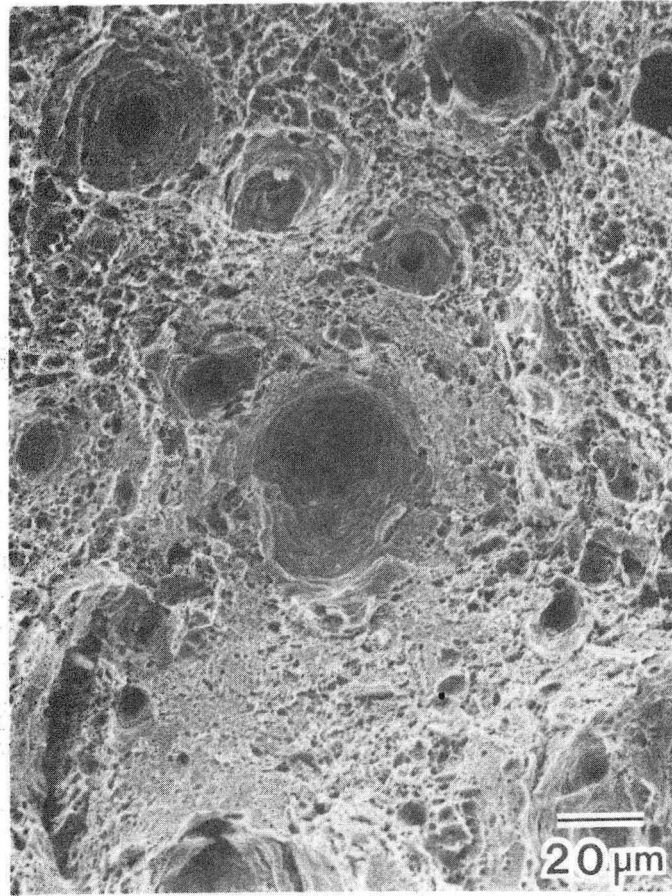


Fig. 13

XBB 840-9426

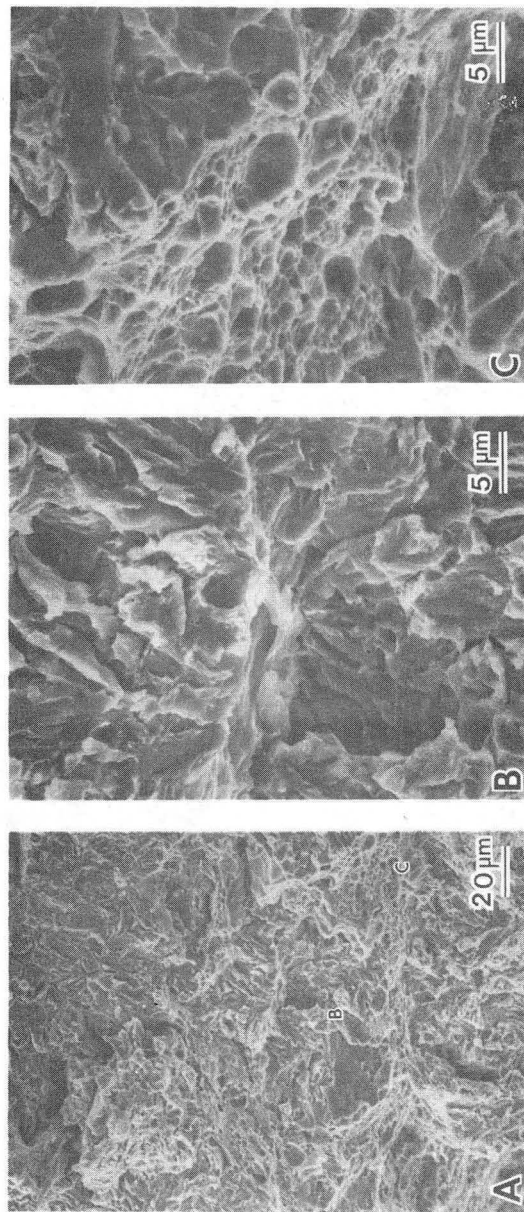
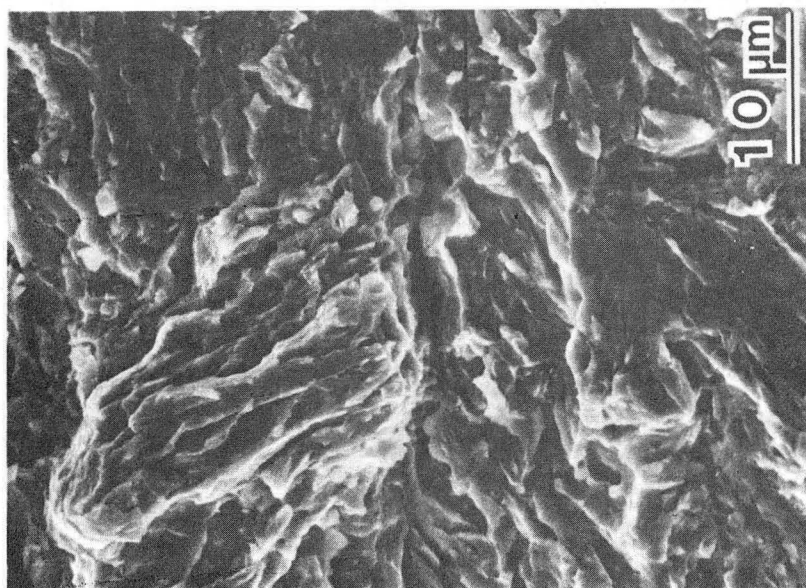
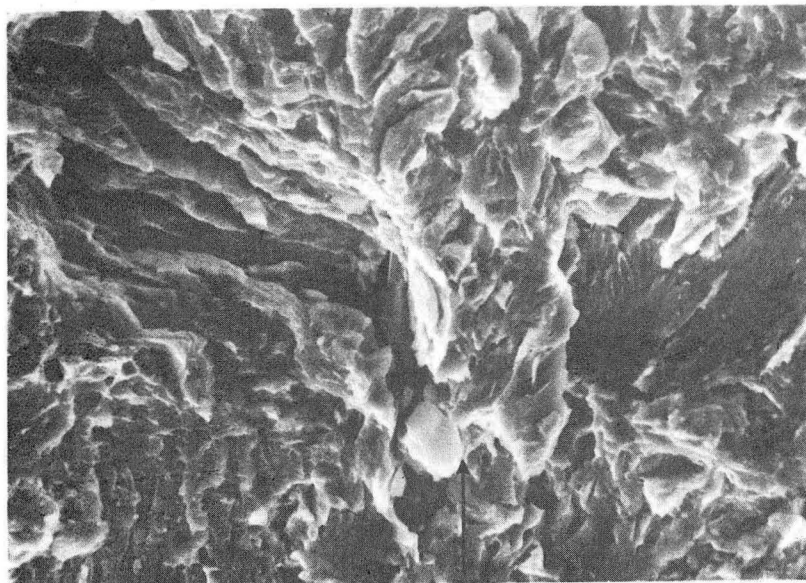


Fig. 14

XBB 841-488



XBB 840-9424

Fig. 15

Slip Plane Decohesion Model (after McMahon)

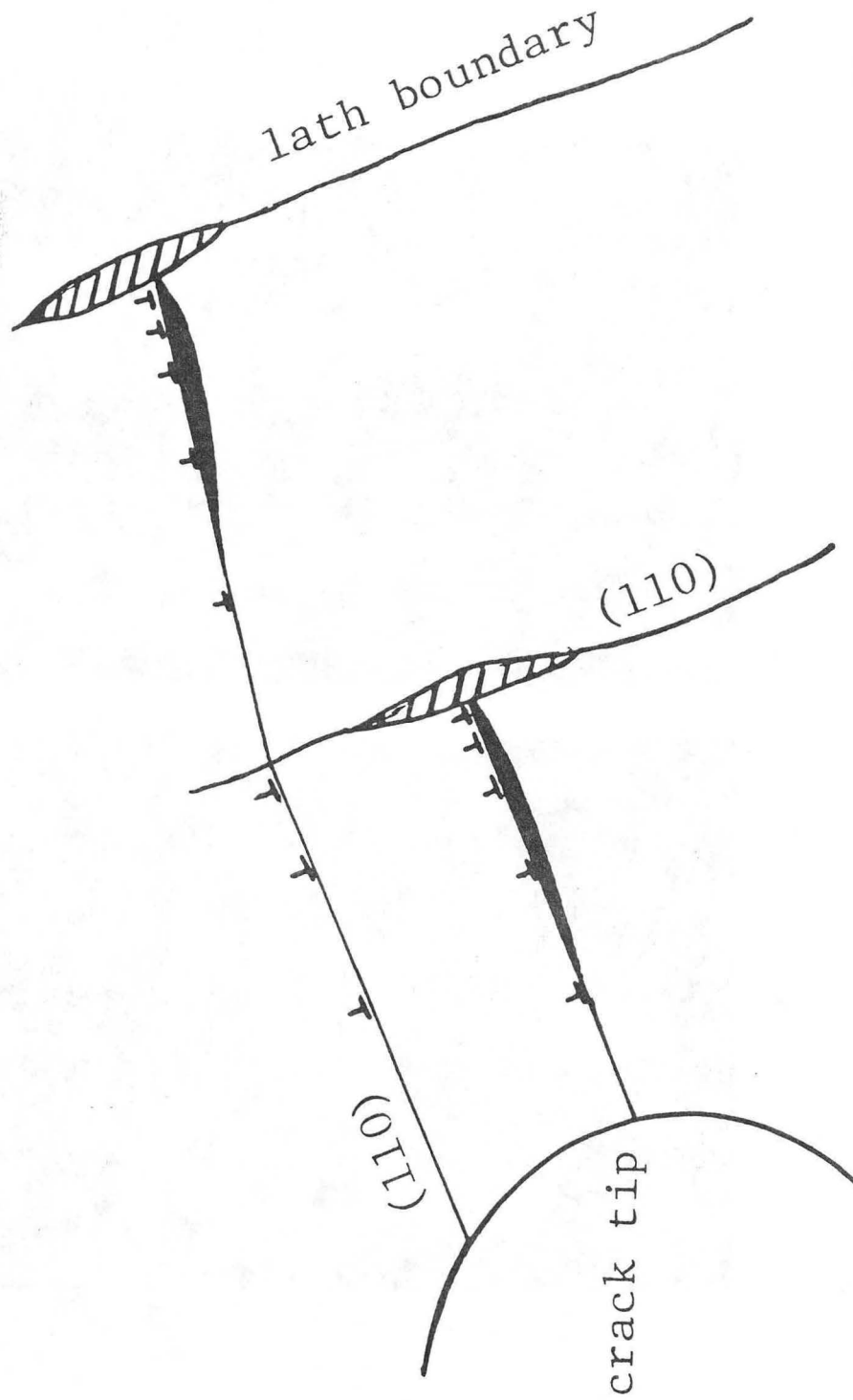


Fig. 16

XBL 8412-5337



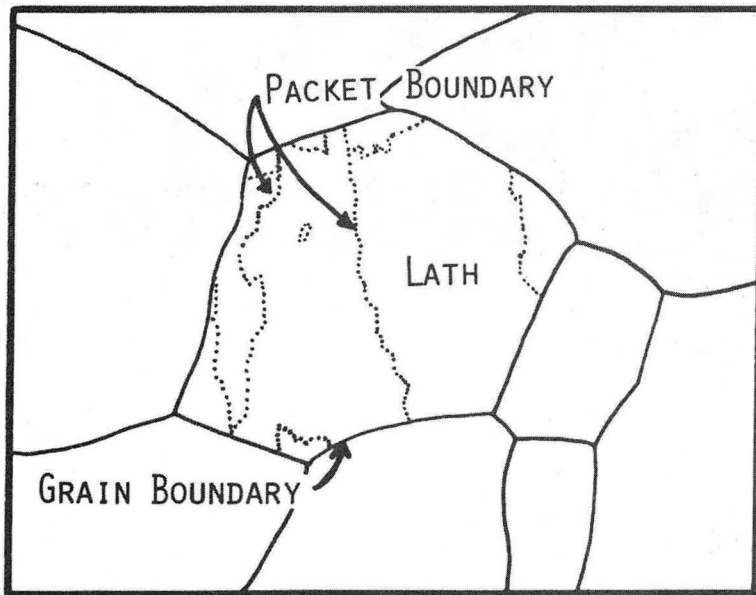
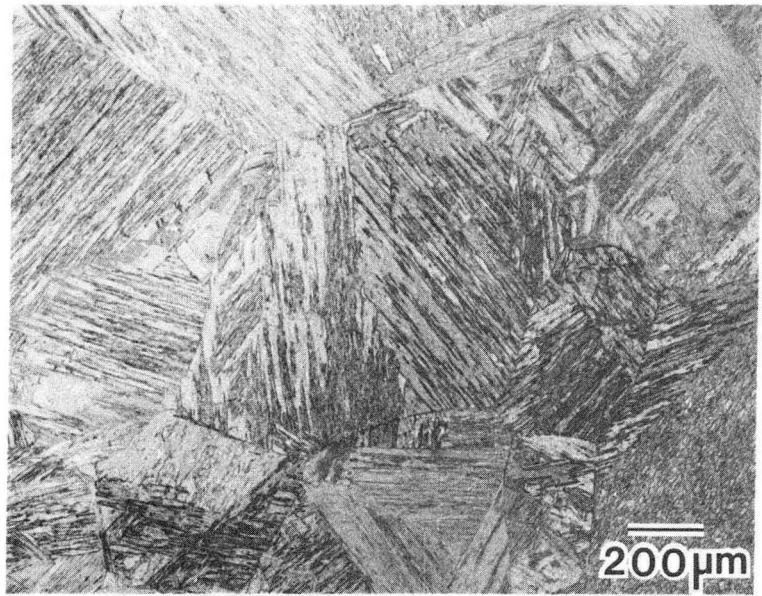


Fig. 17

XBB 851-479



Fig. 18

XBB 822-1312

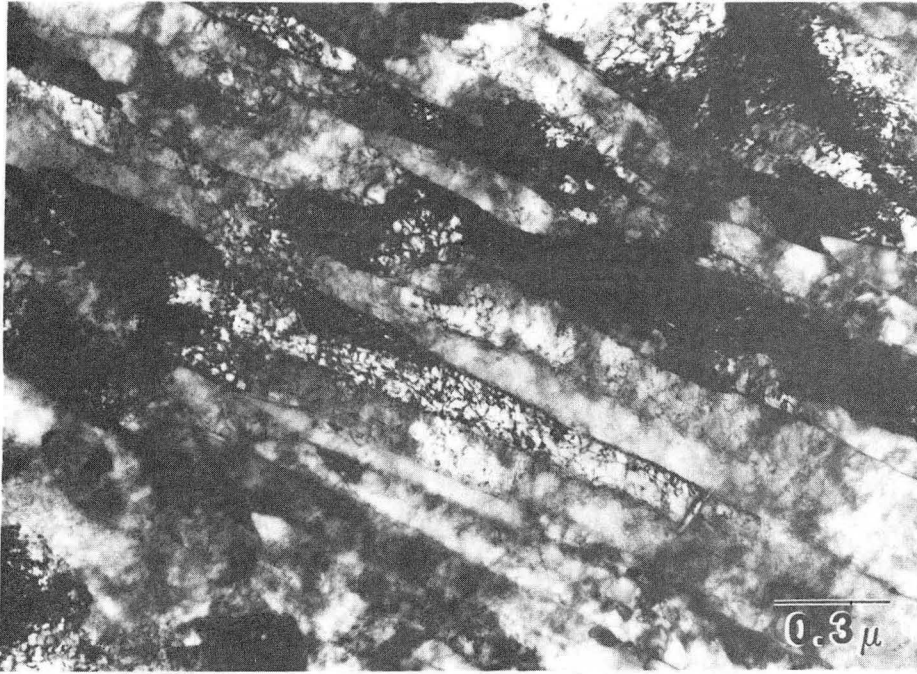


Fig. 19

XBB 822-1313

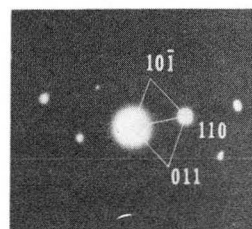
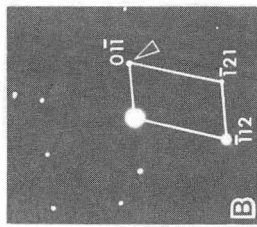
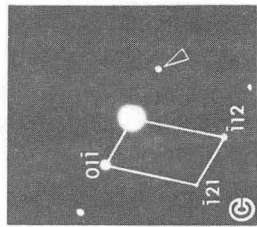
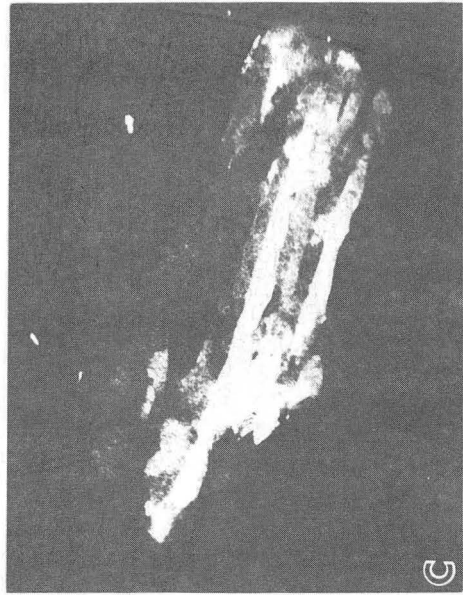
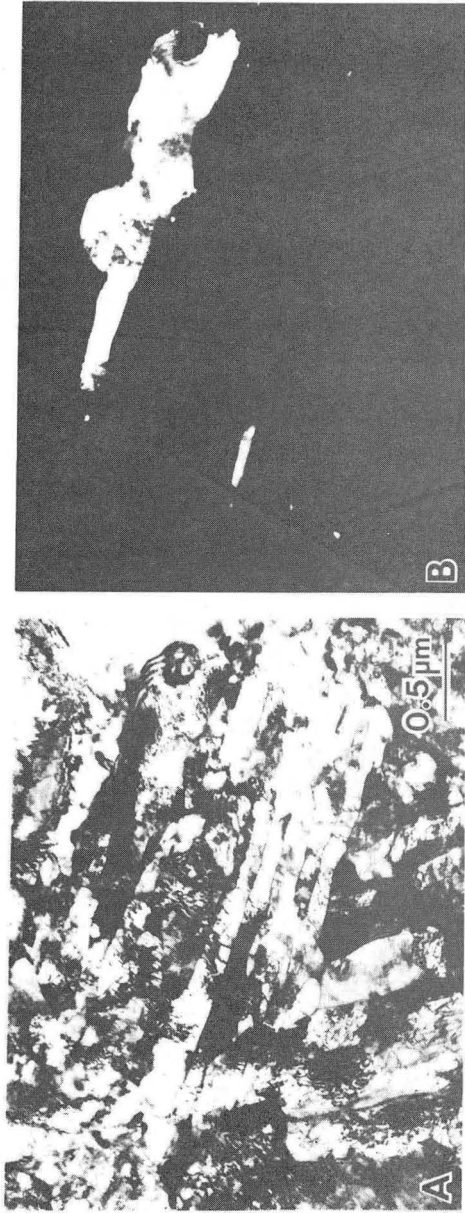


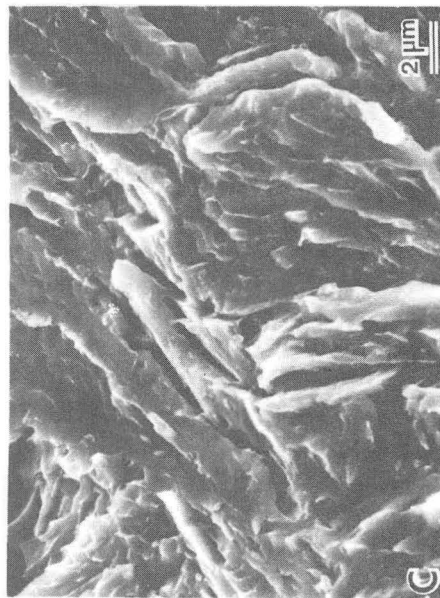
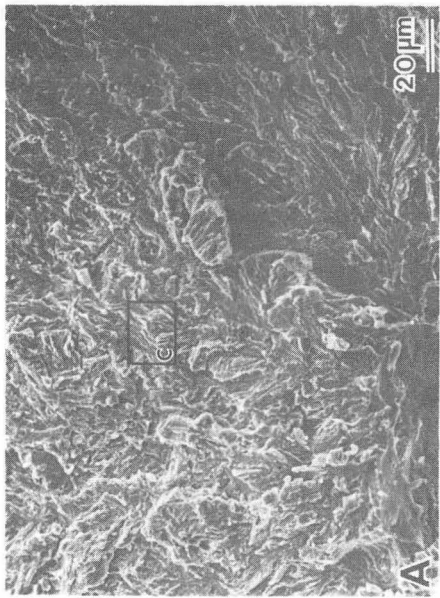
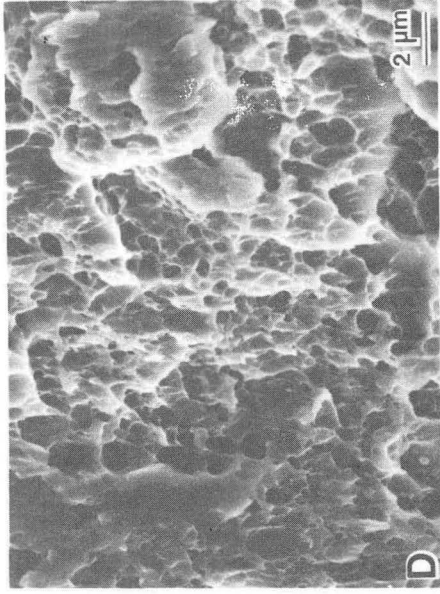
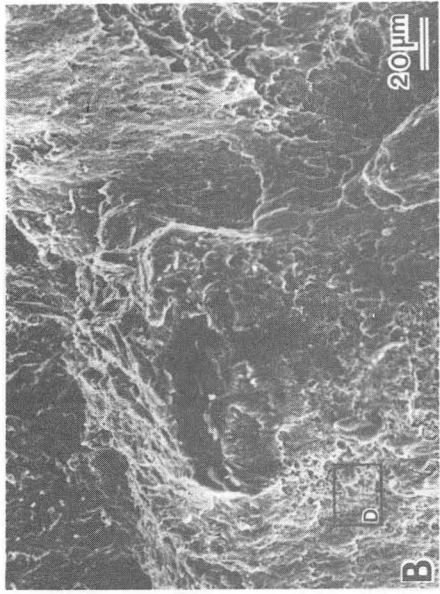
Fig. 20

XBB 829-8222B



XBB 840-8652

Fig. 21



XBB 833-1979

Fig. 22



Fig. 23

XBB 837-6559

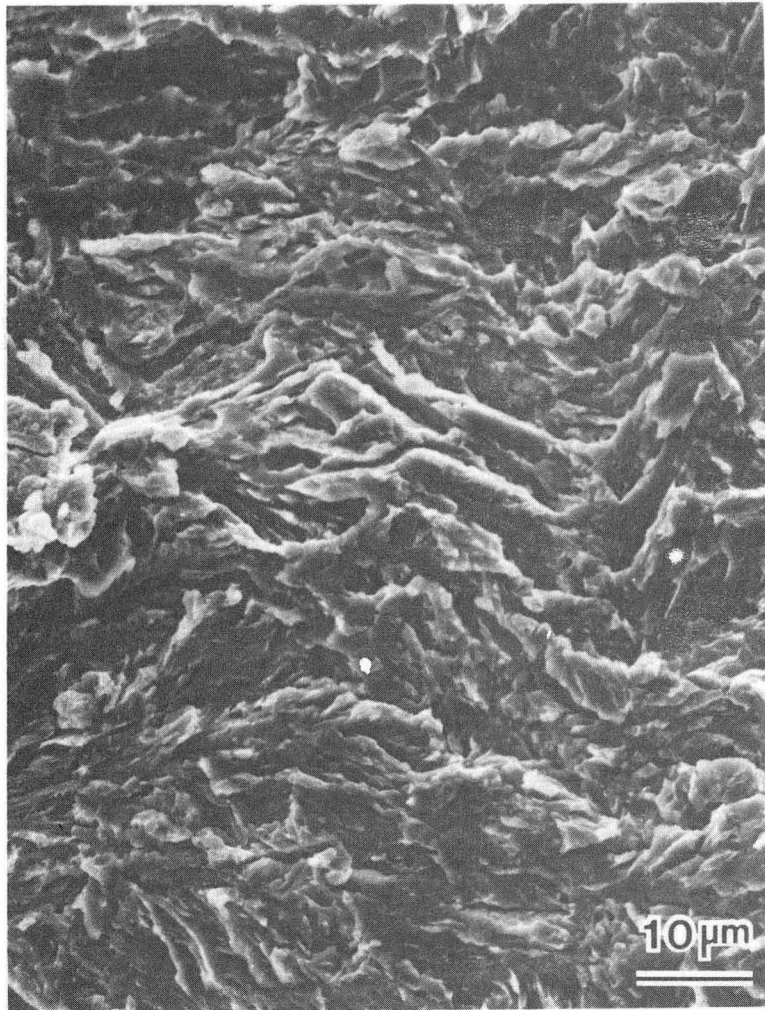


Fig. 24

XBB 835-4521



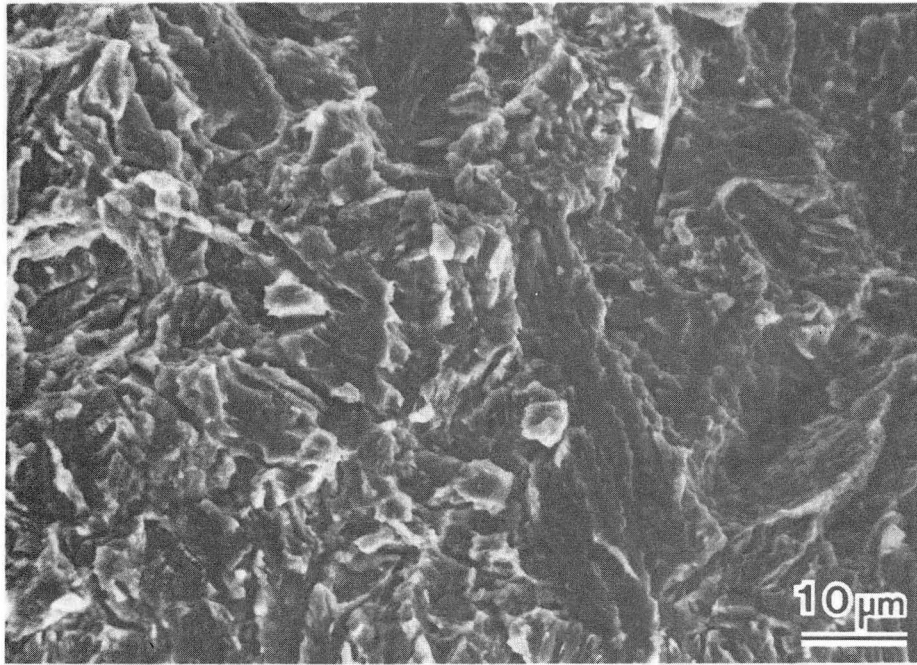


Fig. 25

XBB 844-2684



Fig. 26

XBB 830-10016

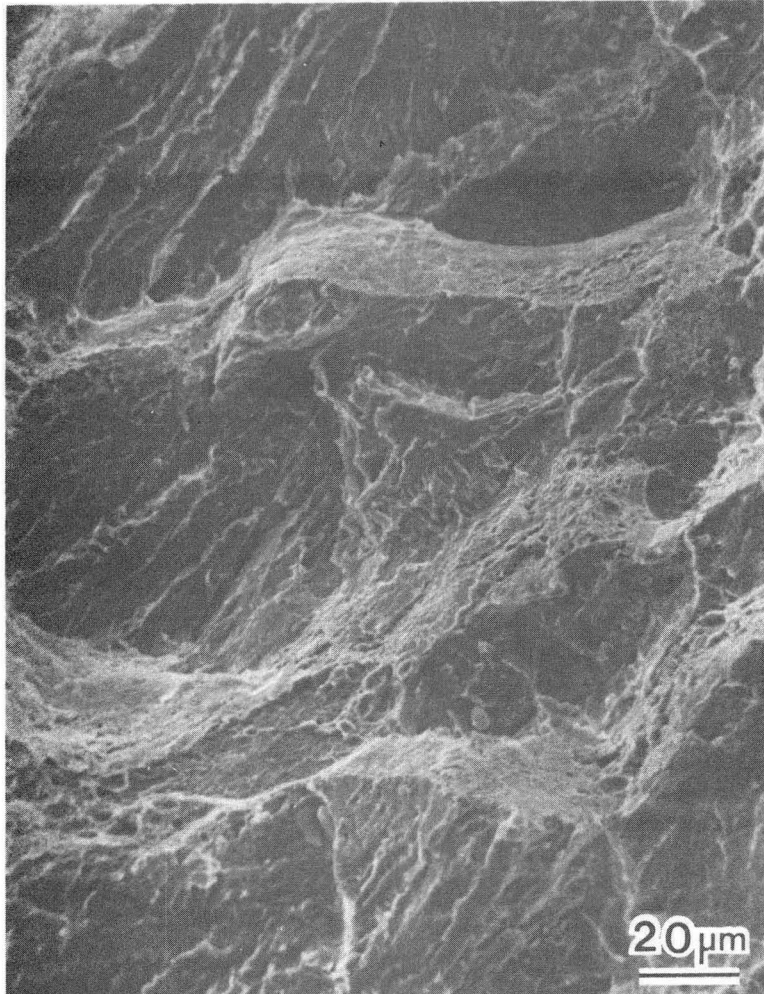


Fig.27

XBB 830-9856

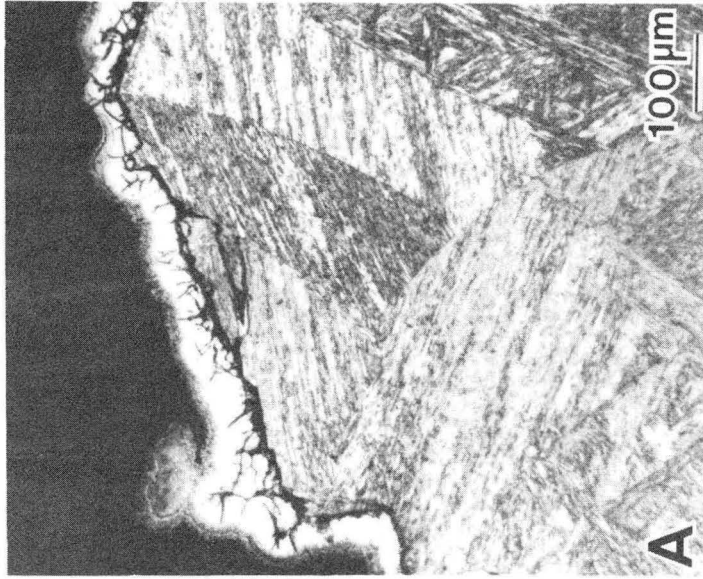


Fig. 28

XBB 839-8232



Fig. 29

XBB 830-9857

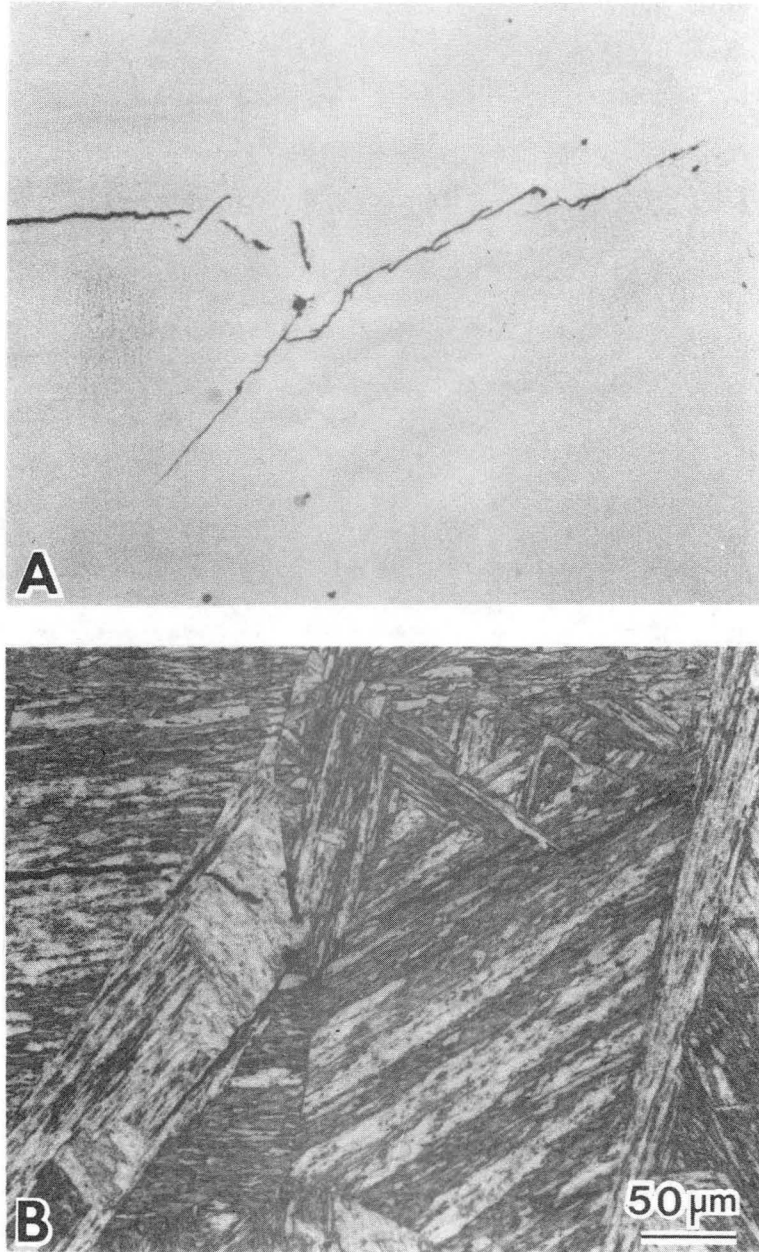


Fig. 30

XBB 830-9858

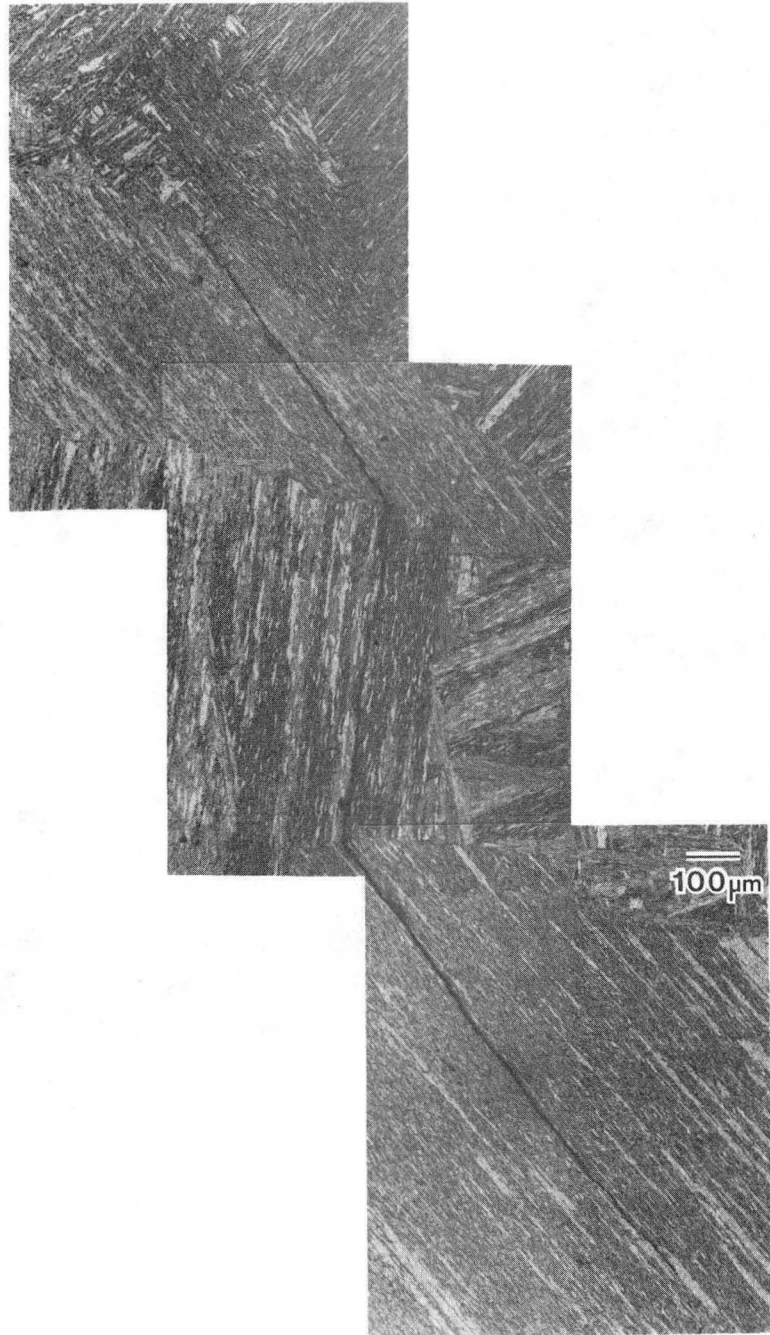


Fig. 31

XBB 830-9859

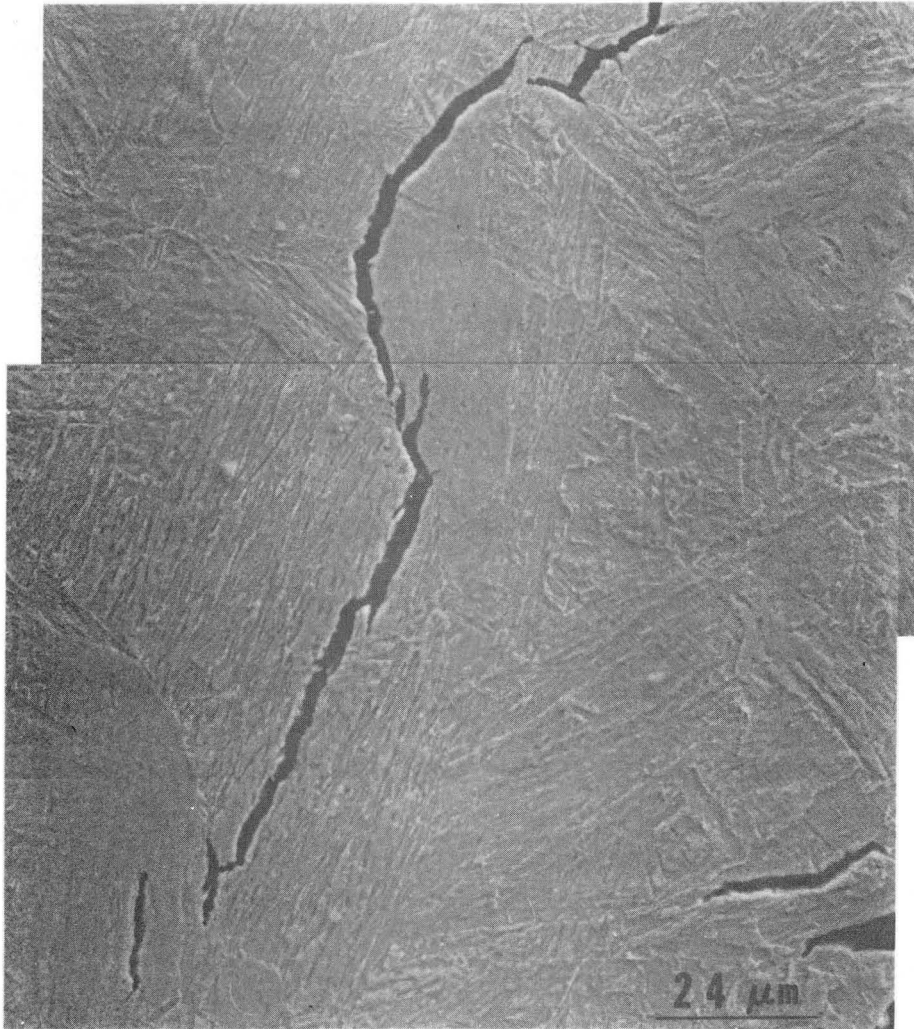


Fig. 32

XBB 829 8368



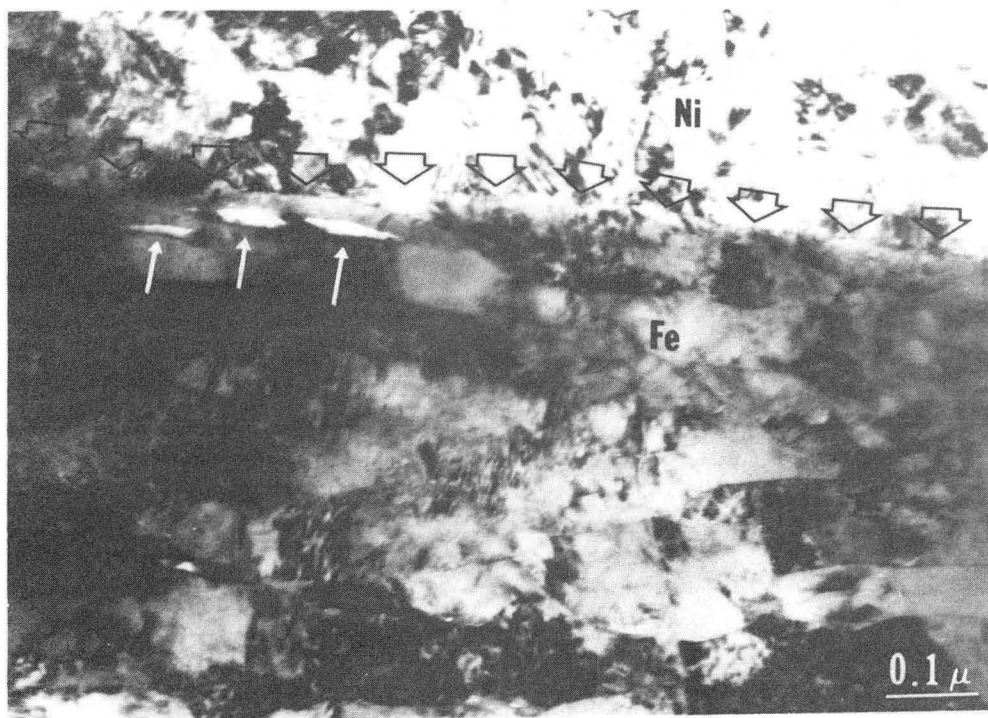


Fig. 33

XBB 820-9309



Fig. 34

XBB 829-8224A

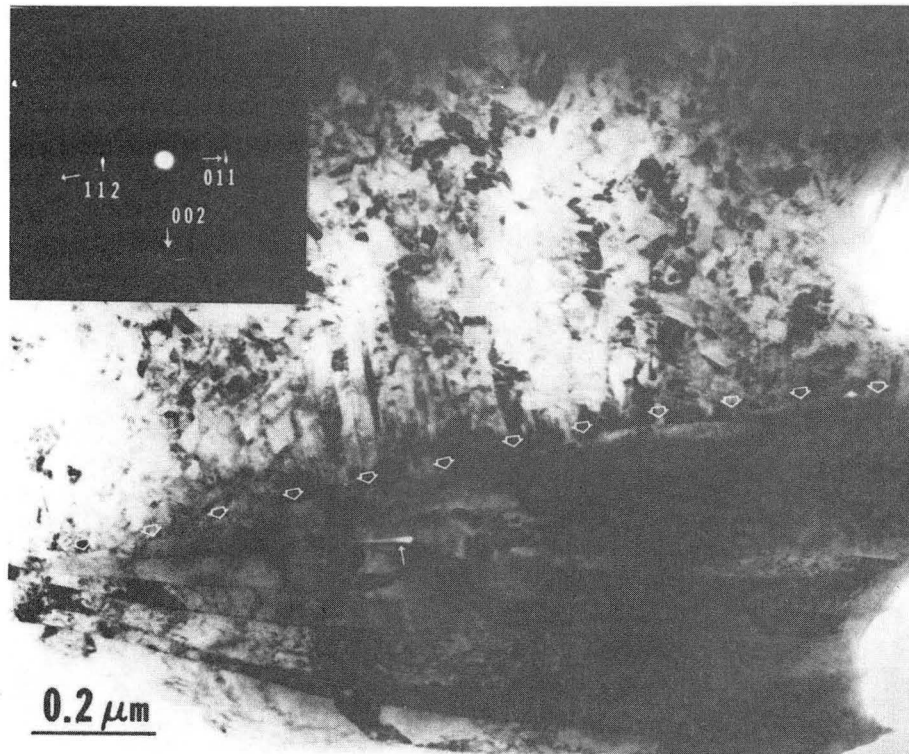


Fig. 35

XBB 829-8221

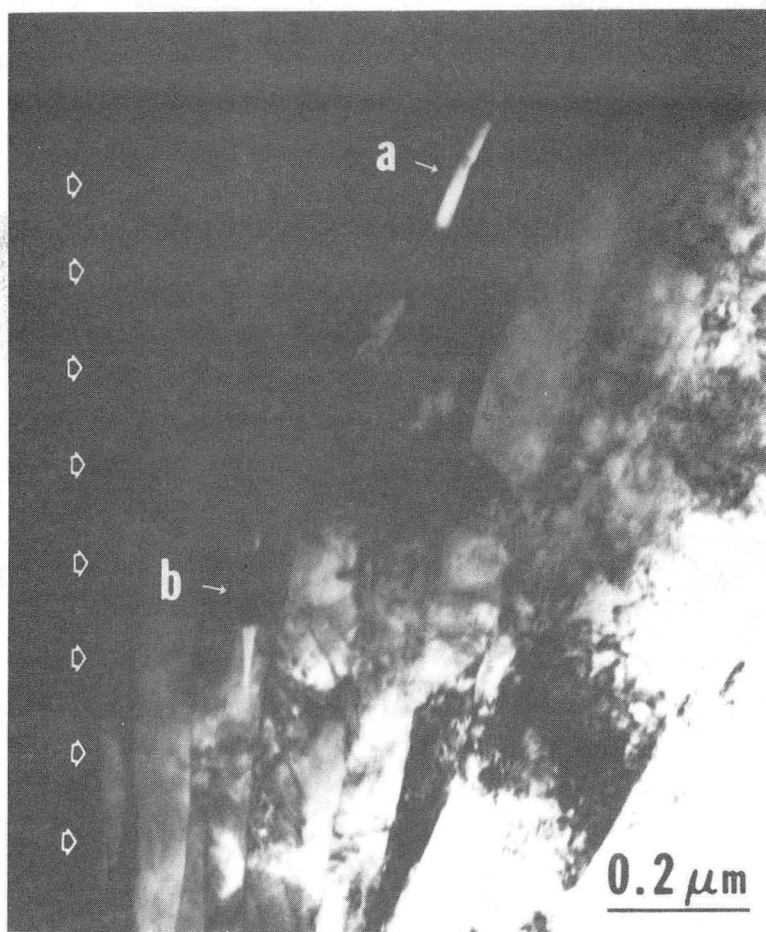


Fig. 36

XBB 829-8223

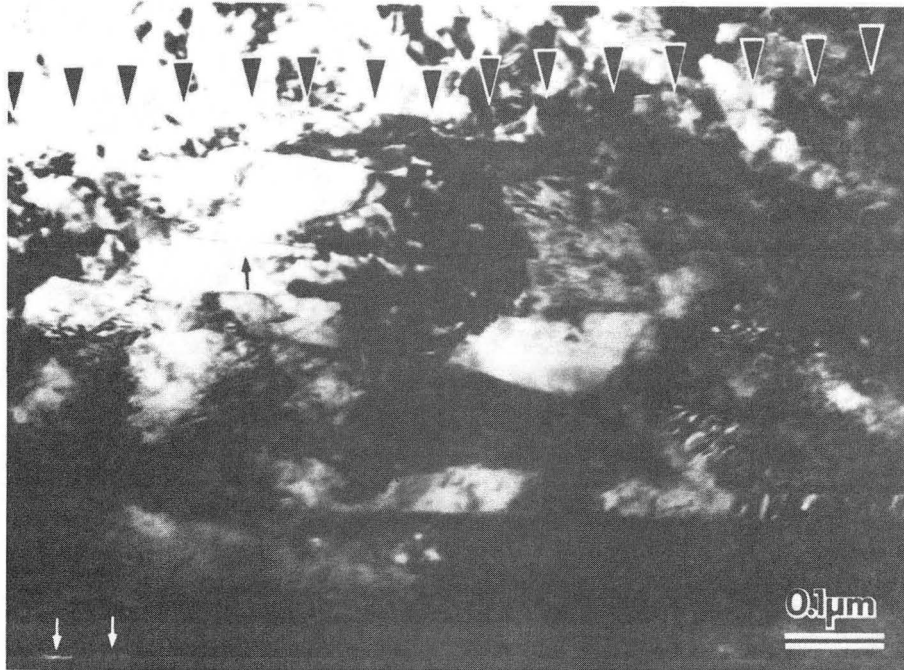


Fig. 37

XBB 855-3762

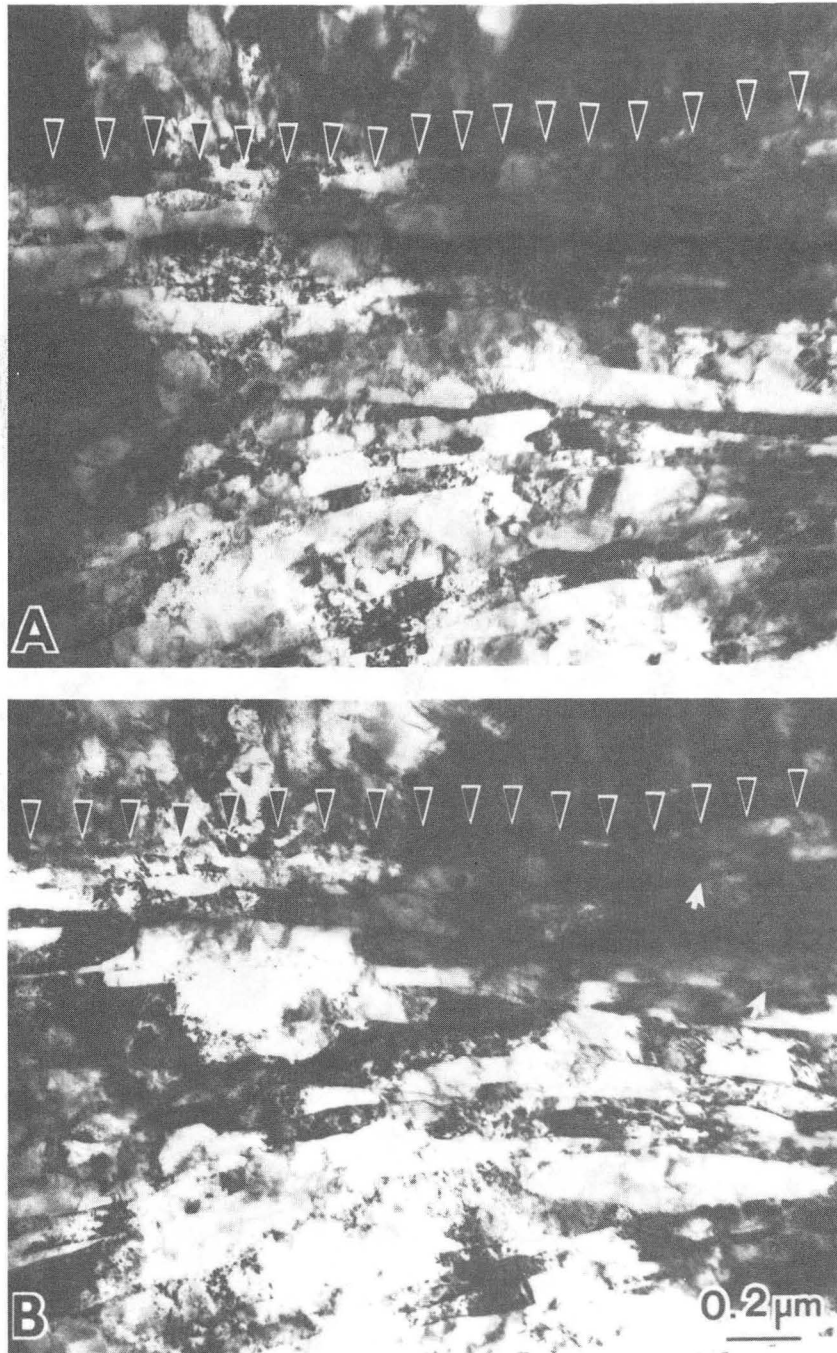


Fig. 38

XBB 842-1235

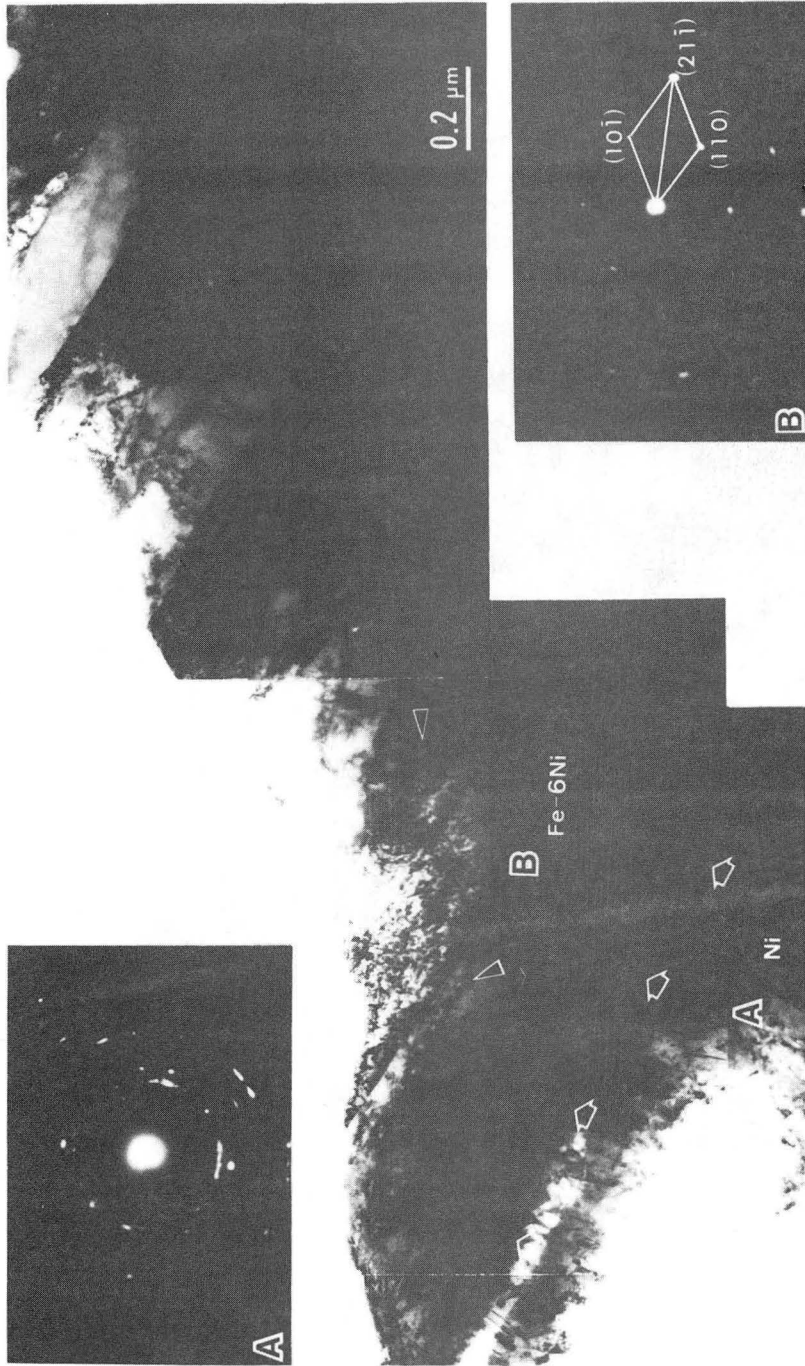


Fig. 39

XBB 833-1973

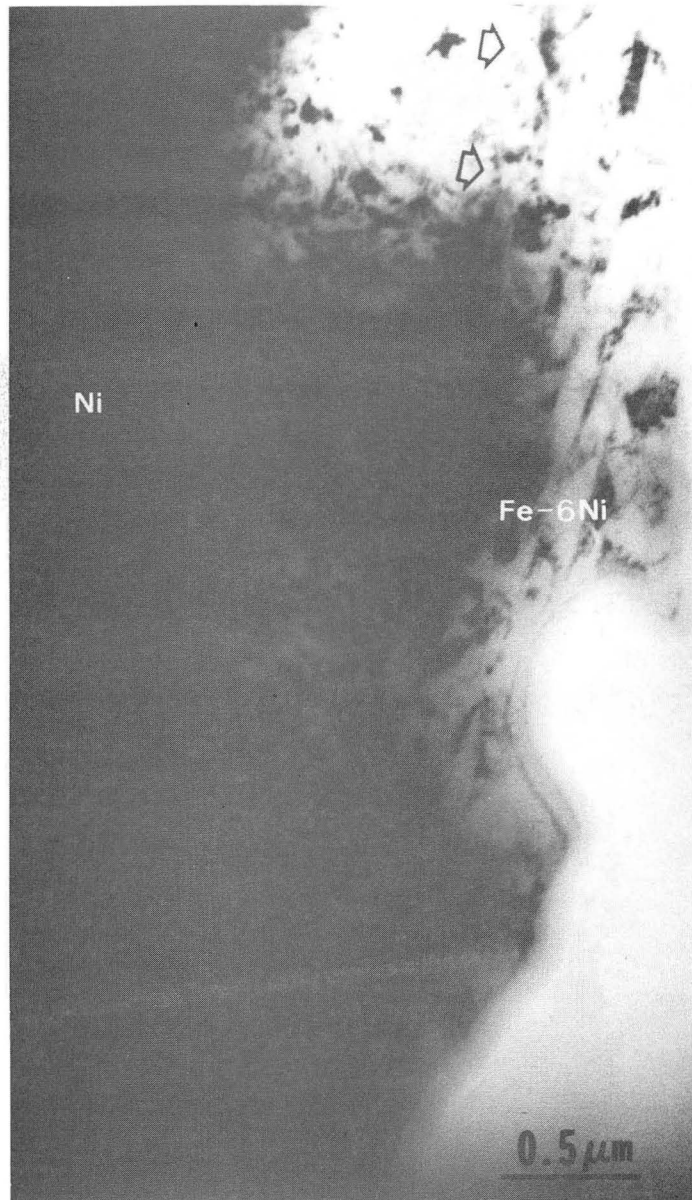


Fig. 40

XBB 833-1975



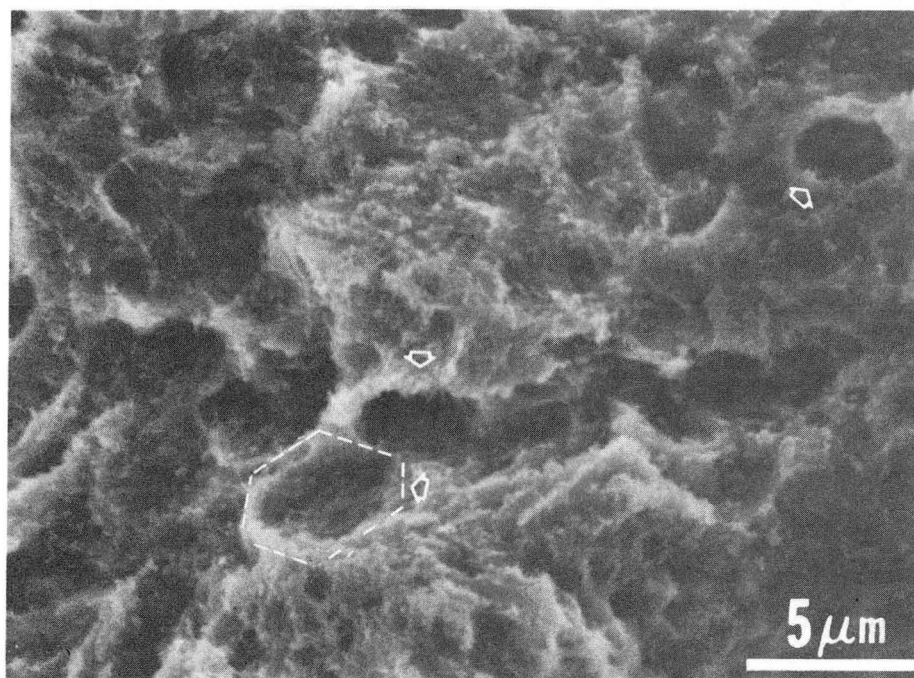


Fig. 41

XBB 820-9086

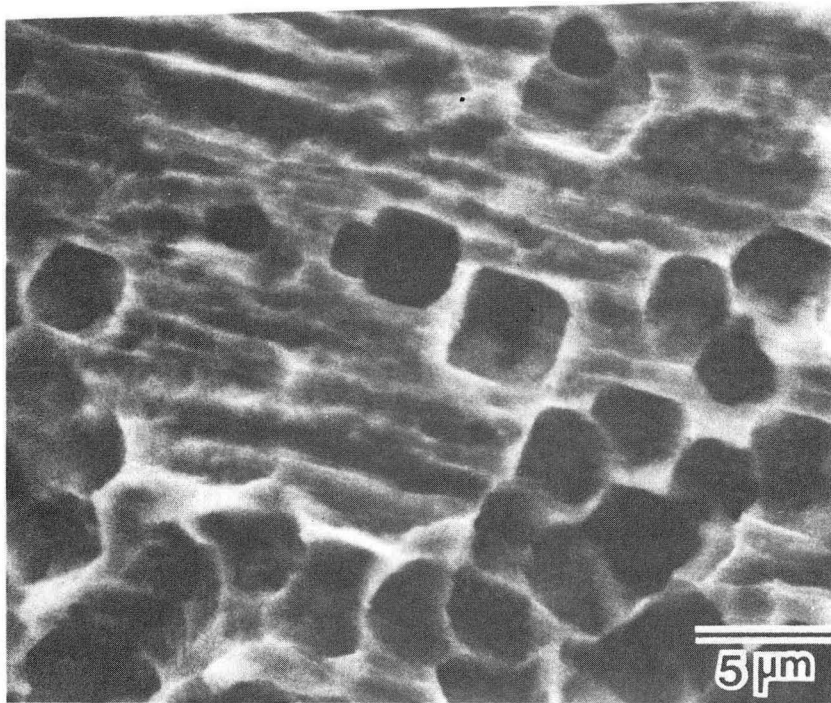


Fig. 42

XBB 851-32

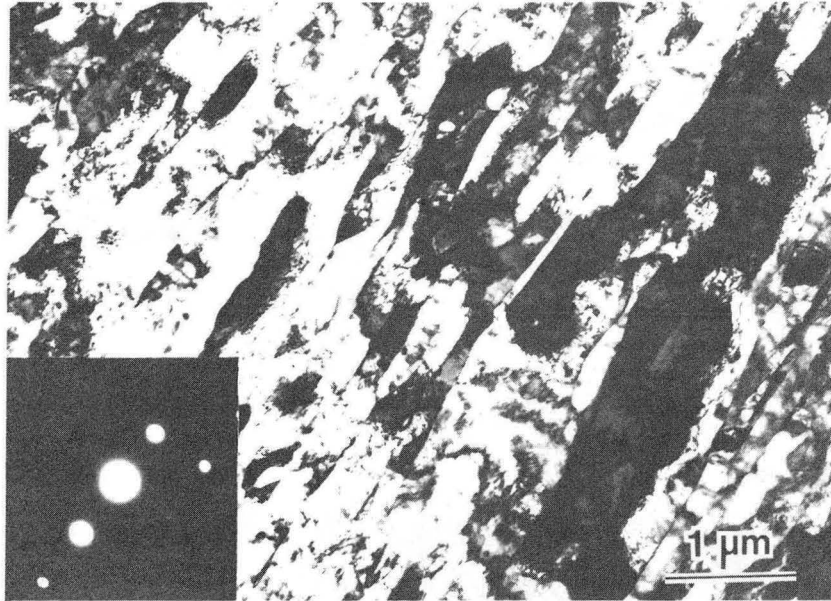


Fig. 43

XBB 840-7609

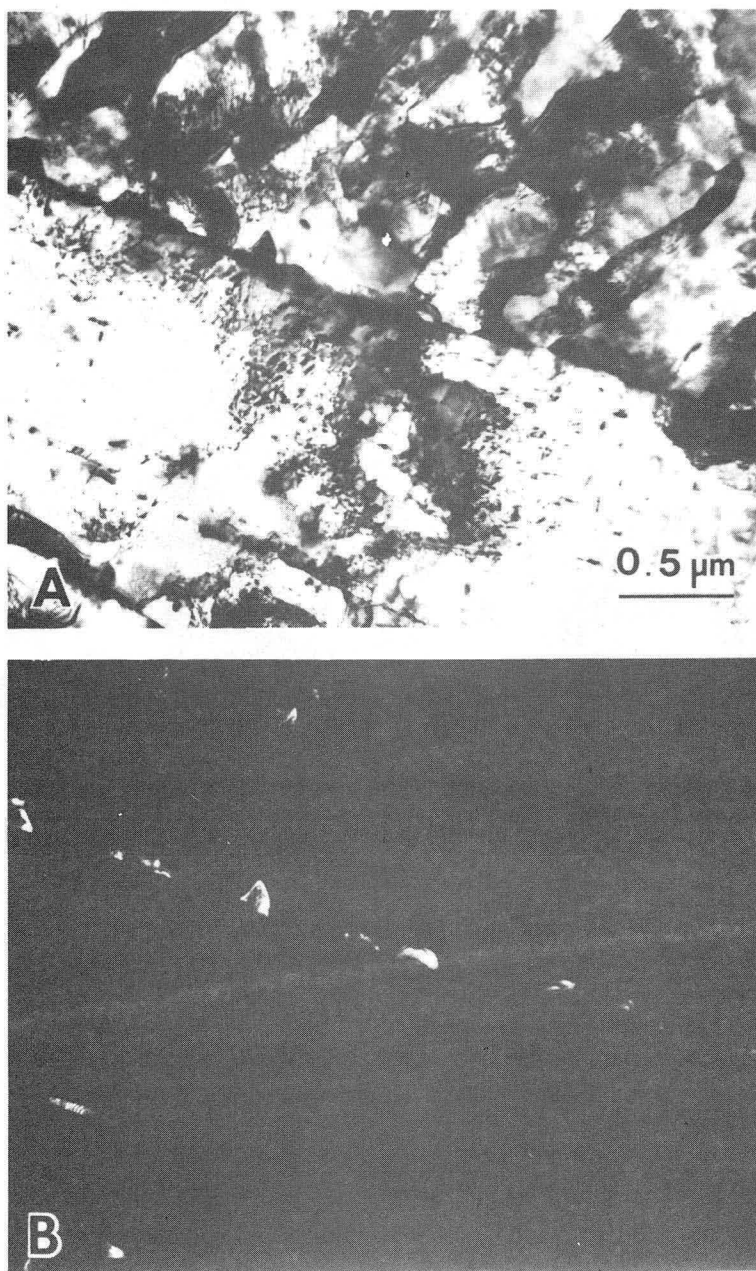
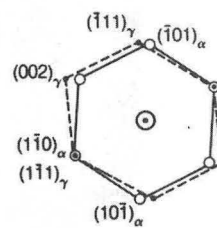
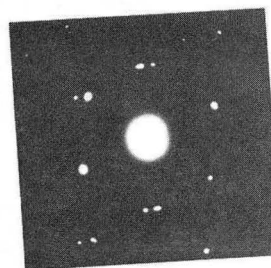
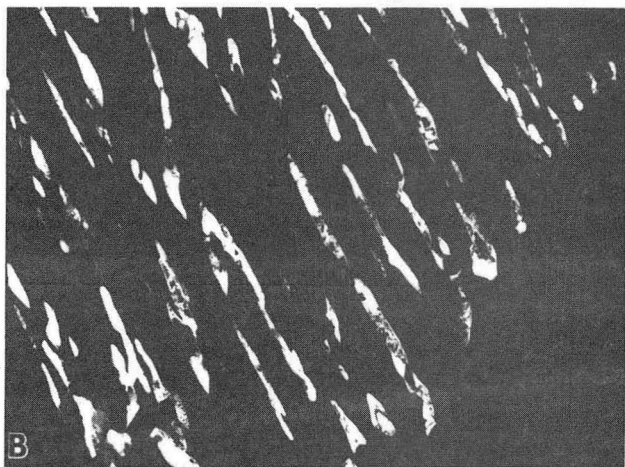
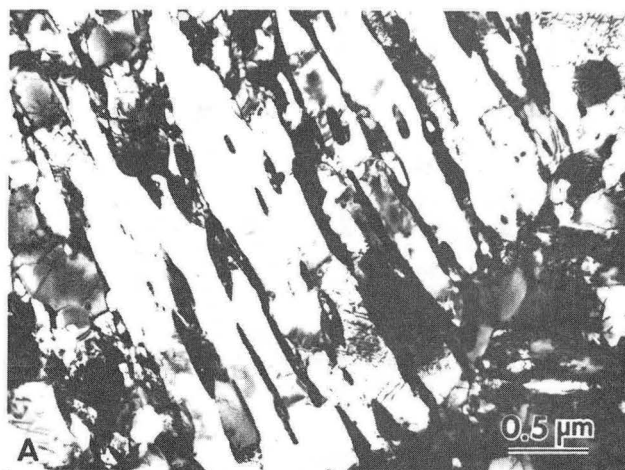


Fig. 44

XBB 849-6754



---- [110] Austenite

— [111] Martensite

Fig. 45

XBB 849-7766

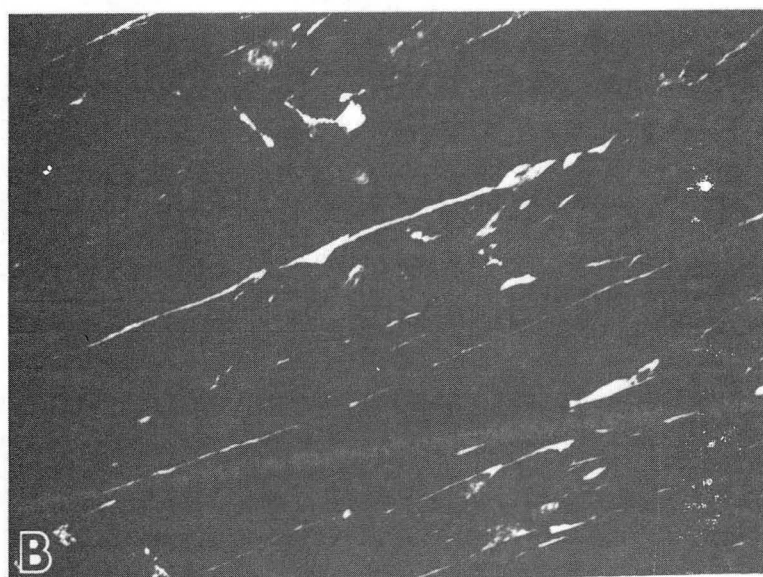
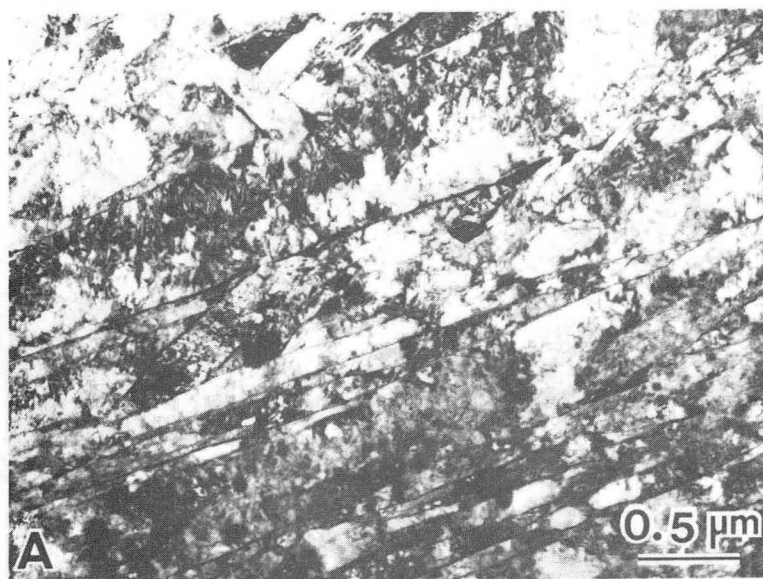
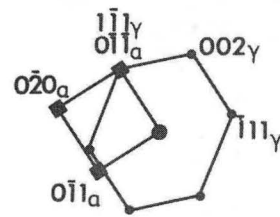
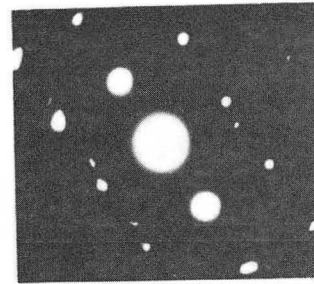
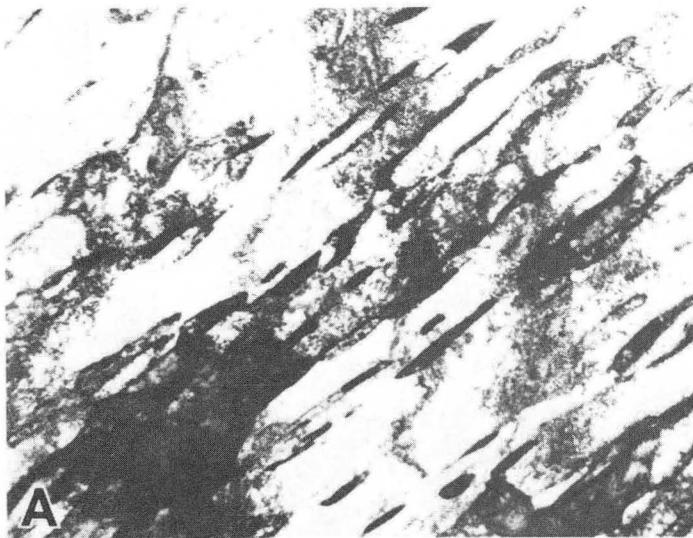


Fig. 46

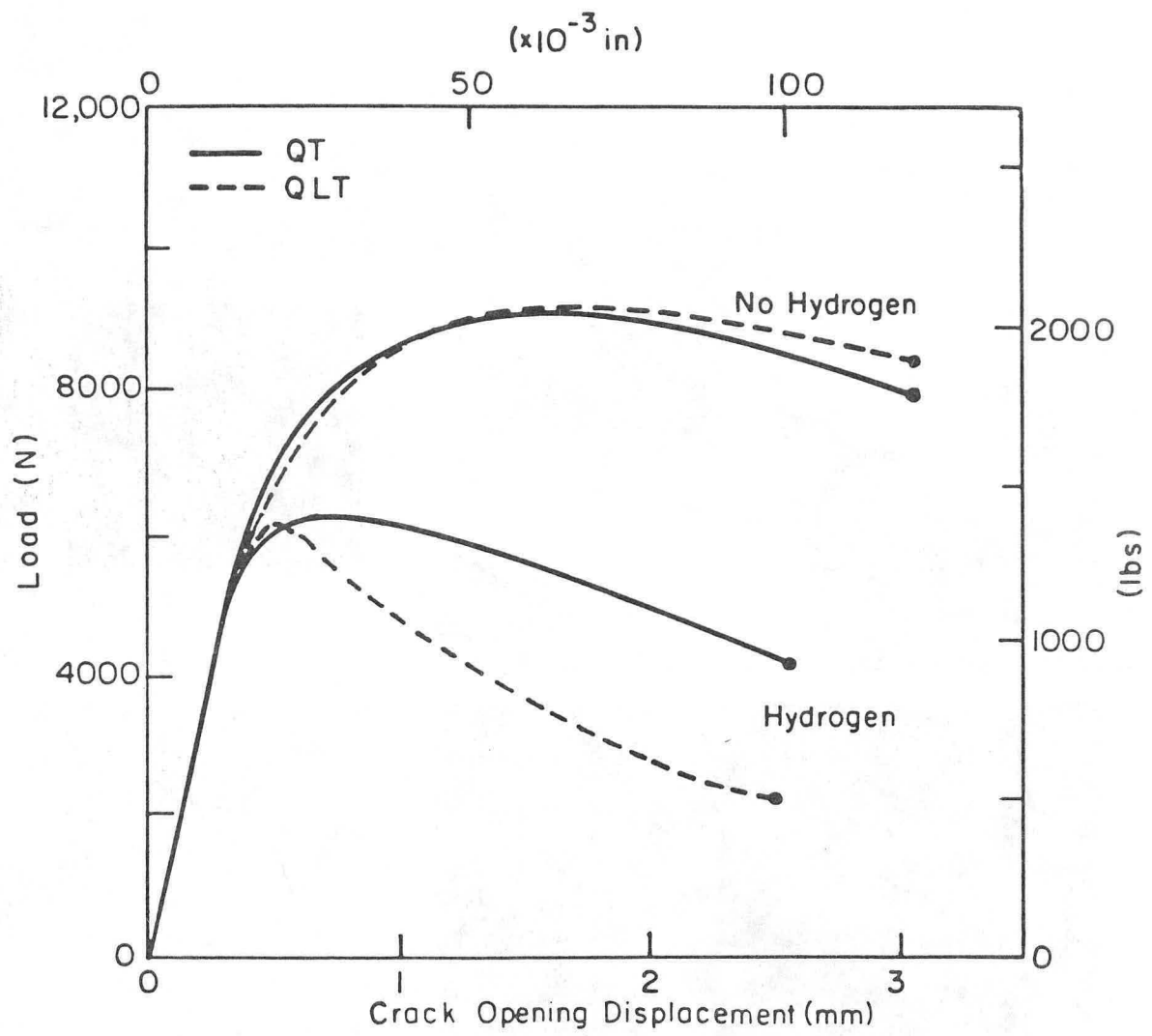
XBB 842-1015



- $[\bar{1}00]$  martensite
- $[\bar{1}\bar{1}0]$  austenite

Fig. 47

XBB 842-1016



XBL 833 - 5367

Fig. 48



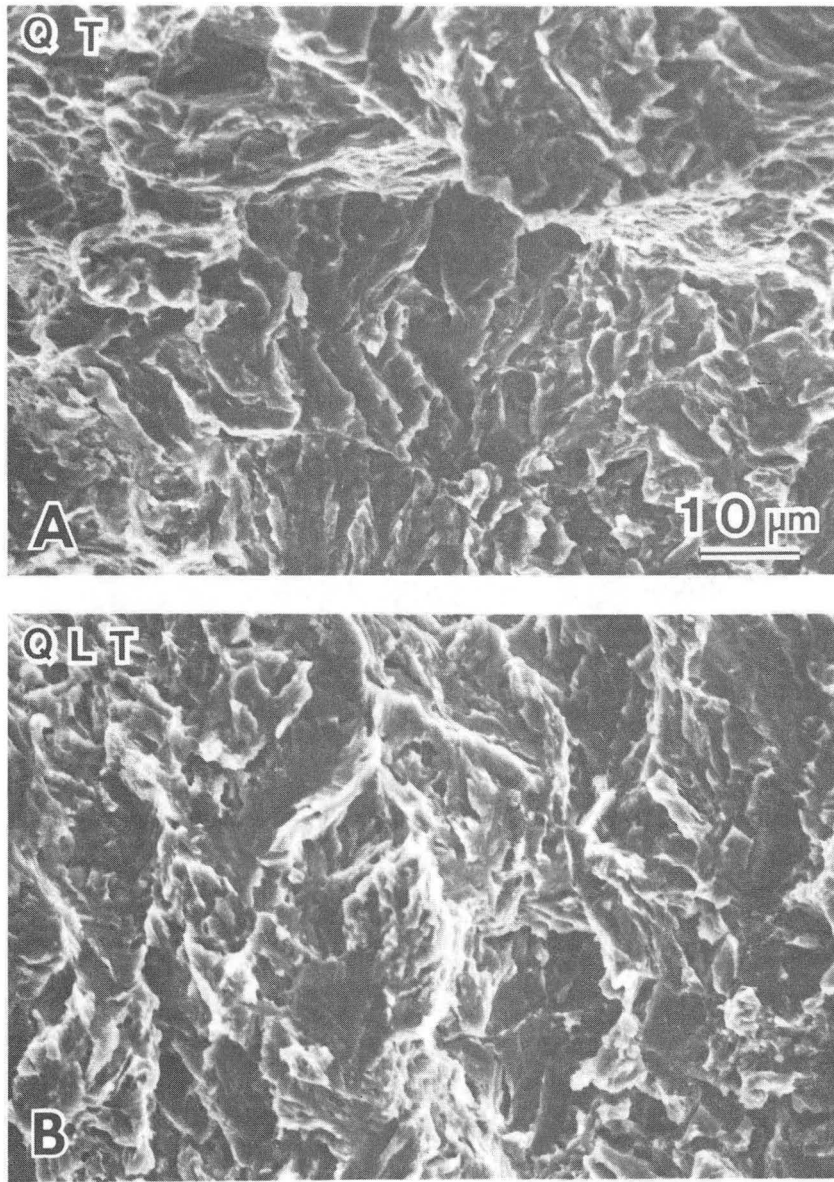


Fig. 49

XBB 845-3543

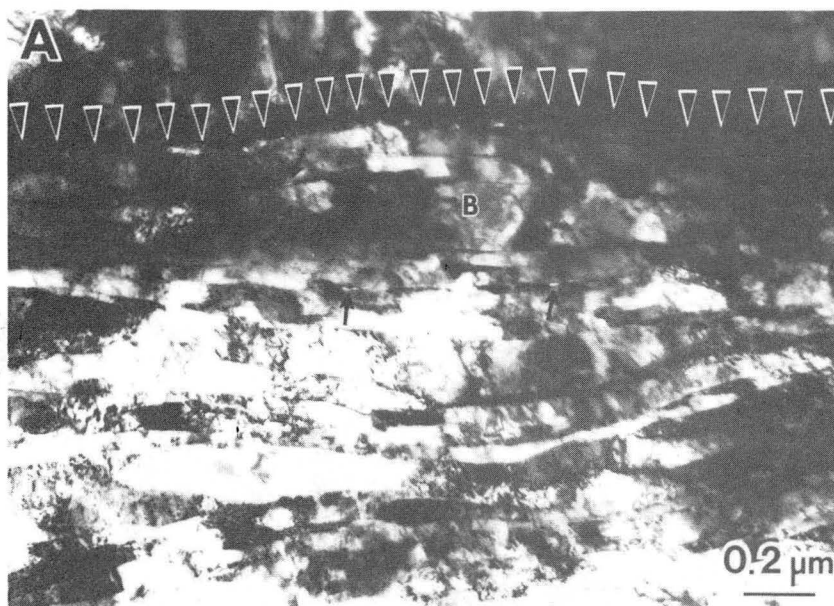


Fig. 50

XBB 842-1234

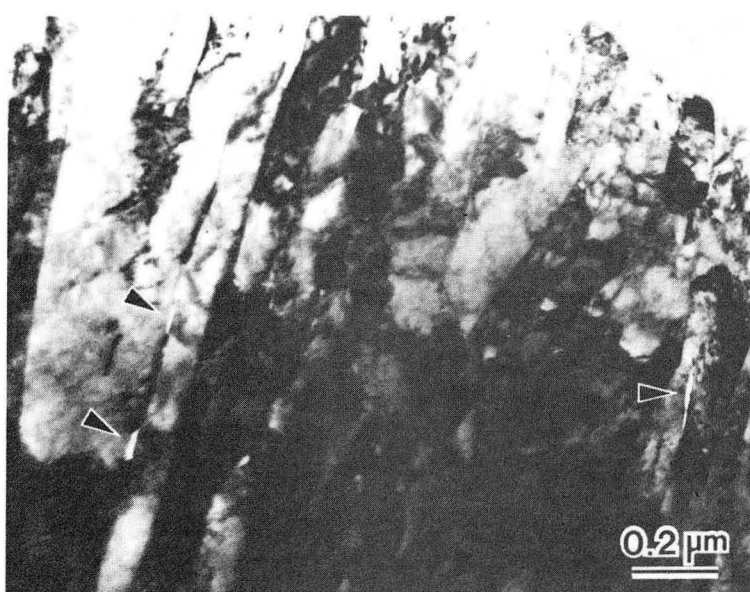


Fig. 51

XBB 842-1013

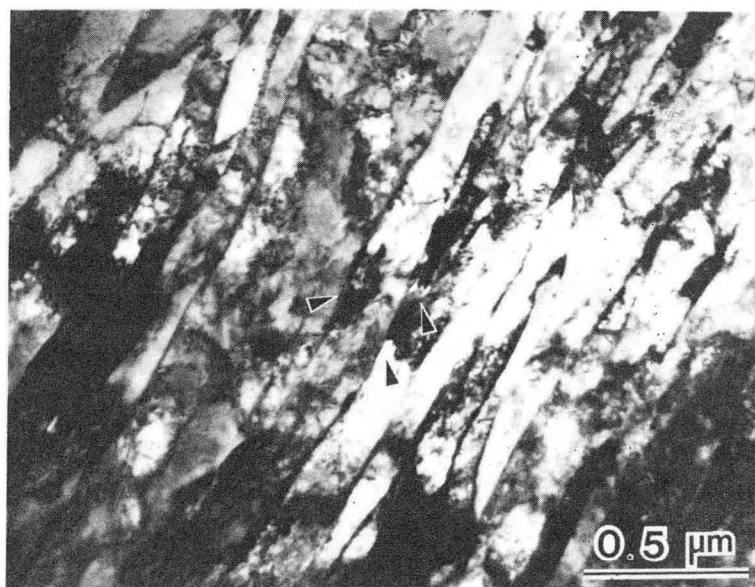


Fig. 52

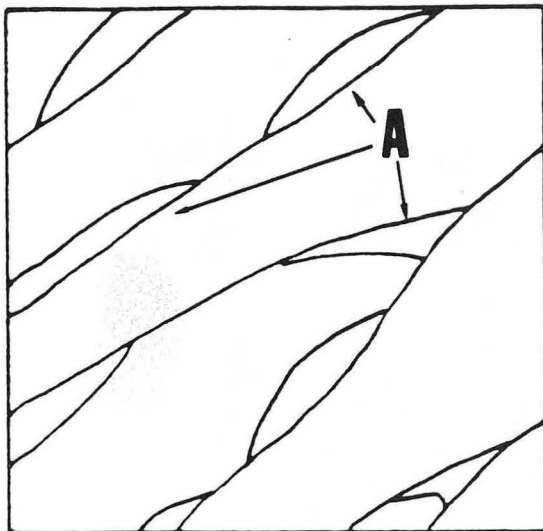
XBB 842-1014



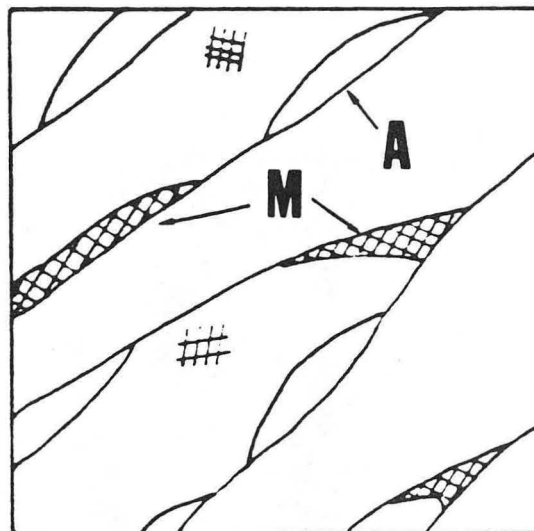
Fig. 53

XBB 842-1012

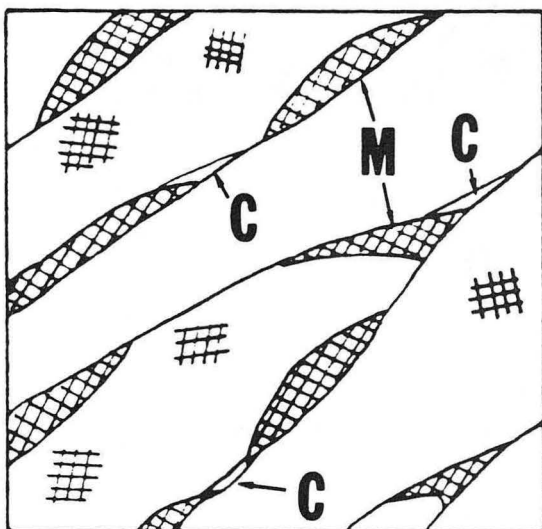
## 1. Initial Structure



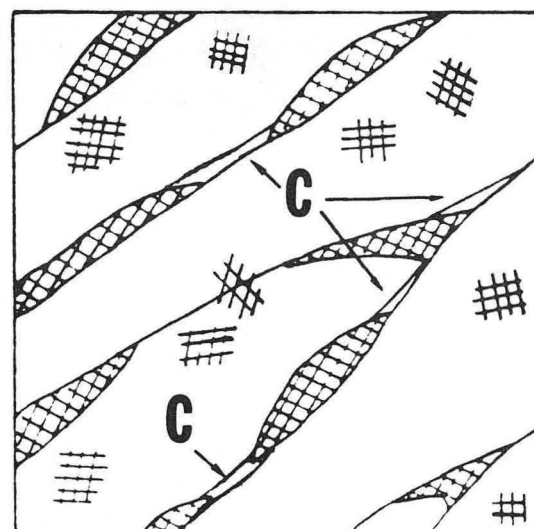
## 2. Transformation



## 3. Microcrack initiation



## 4. Microcrack coalescence



XBL 848-3335

Fig. 54

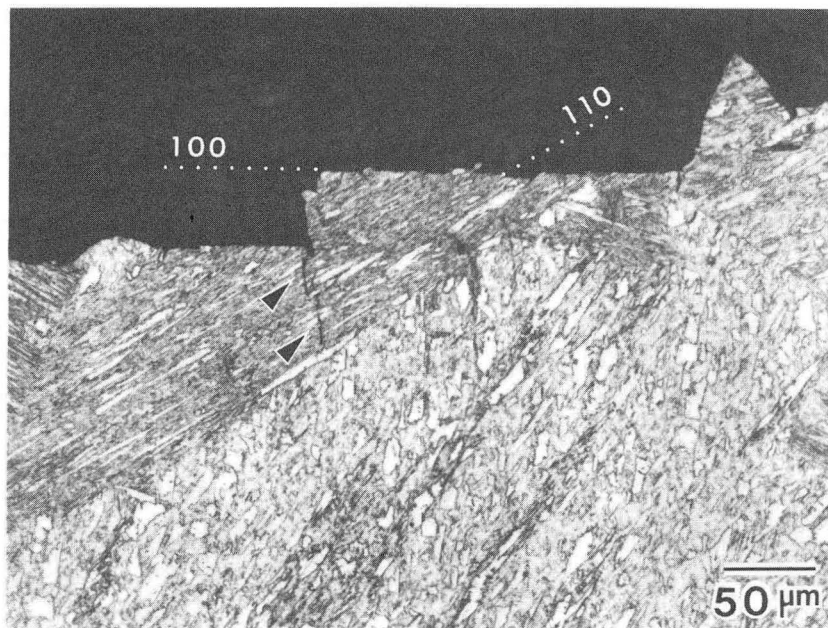
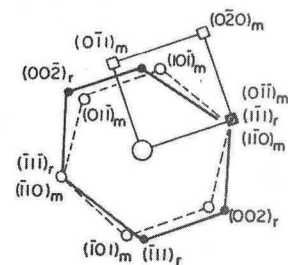
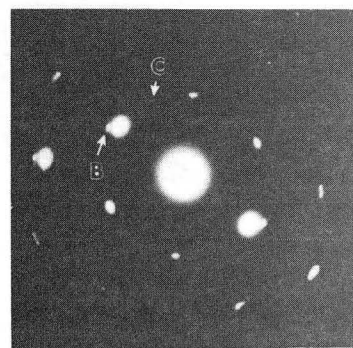
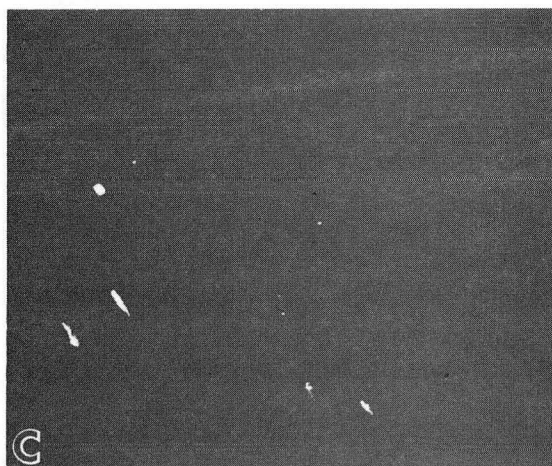


Fig. 55

XBB 840-9676



- $[111]$  martensite
- $[\bar{1}00]$  martensite
- $[\bar{1}\bar{1}0]$  austenite

Fig. 56

XBB 830-9216



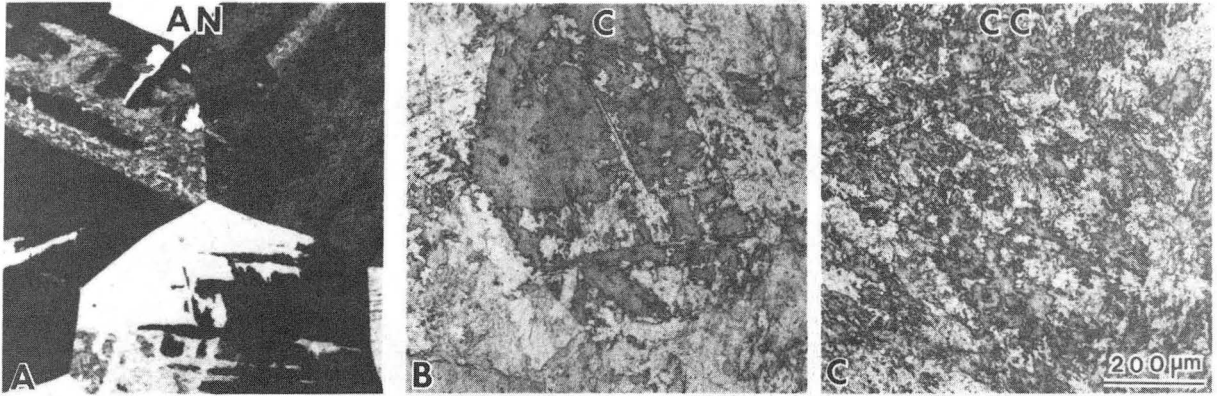


Fig. 57

XBB 855-4037

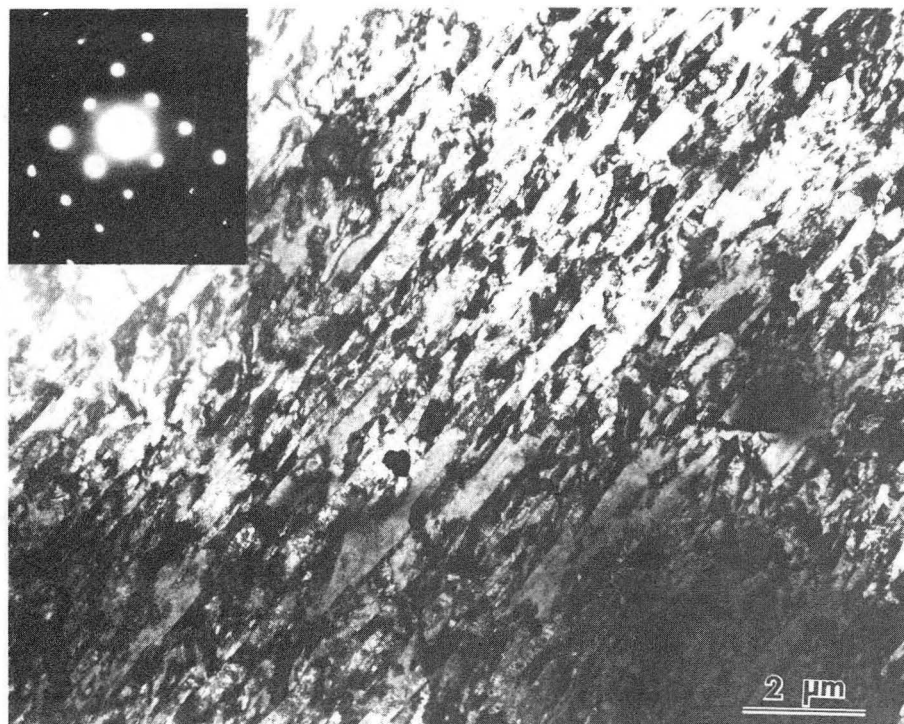
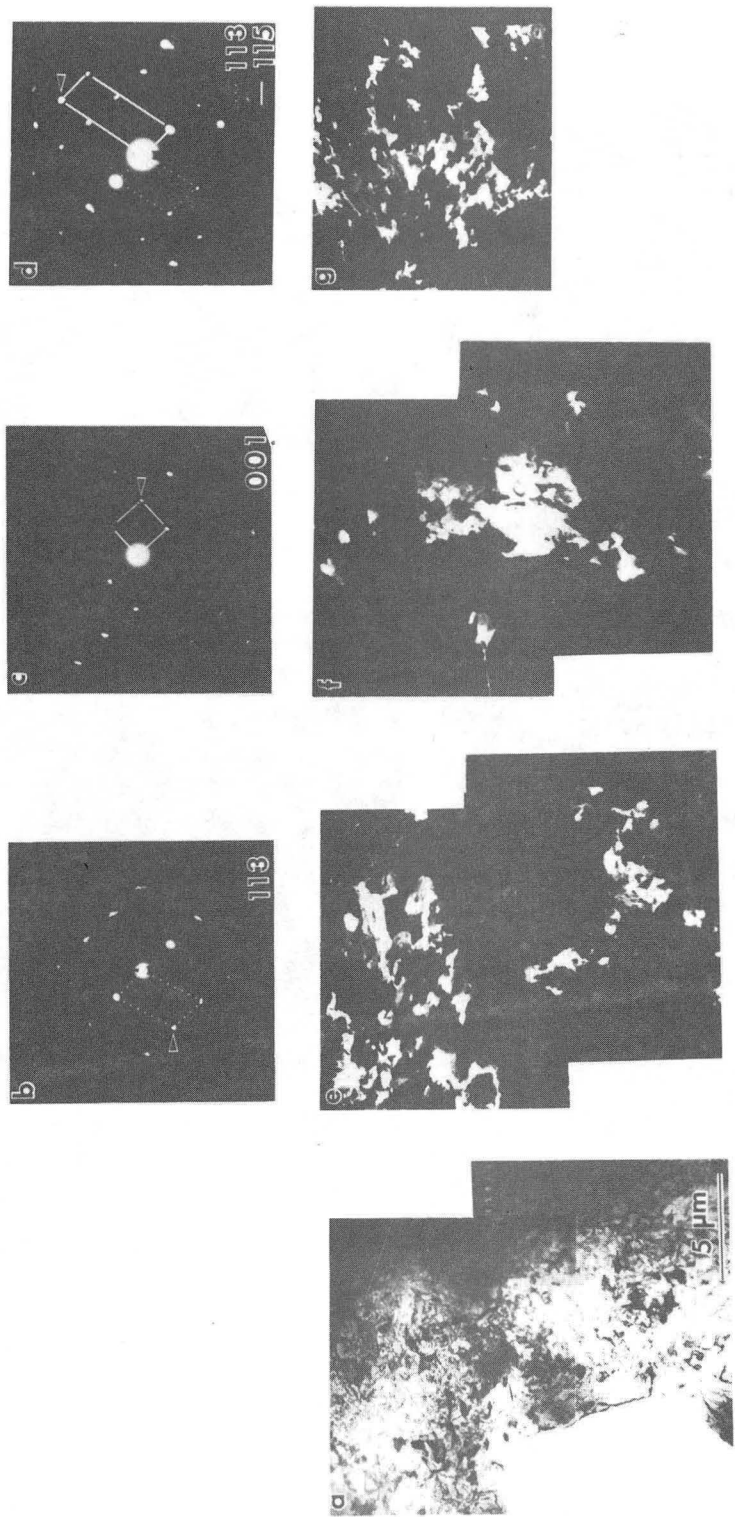


Fig. 58

XBB 830-10357



XBB 830-11013

Fig. 59

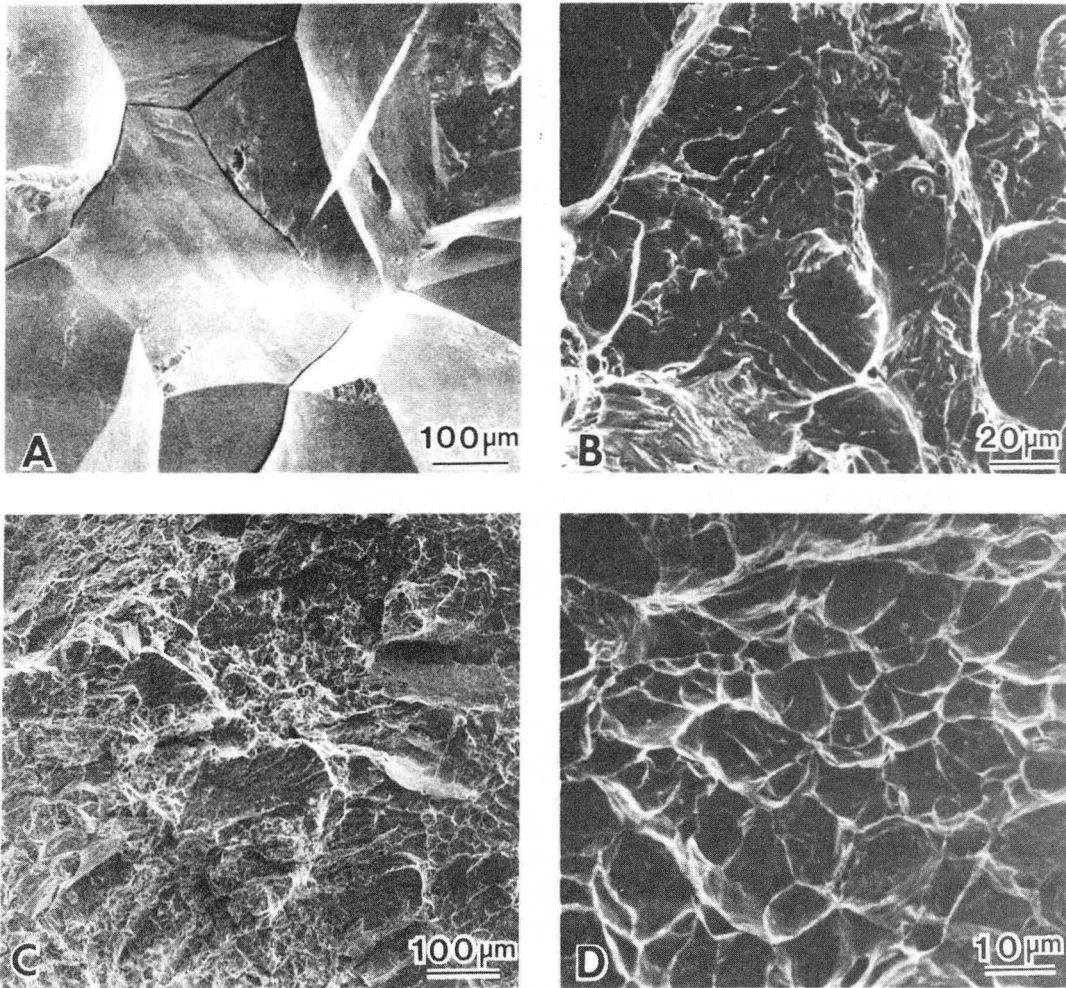


Fig. 60

XBB 855-4036

This report was done with support from the Department of Energy. Any conclusions or opinions expressed in this report represent solely those of the author(s) and not necessarily those of The Regents of the University of California, the Lawrence Berkeley Laboratory or the Department of Energy.

Reference to a company or product name does not imply approval or recommendation of the product by the University of California or the U.S. Department of Energy to the exclusion of others that may be suitable.

*LAWRENCE BERKELEY LABORATORY  
TECHNICAL INFORMATION DEPARTMENT  
UNIVERSITY OF CALIFORNIA  
BERKELEY, CALIFORNIA 94720*